OXFORD UNIVERSITY PRESS | Brain

Gene replacement ameliorates deficits in mouse and human models of cyclin-dependent kinase-like 5 disorder

Journal:	*Brain*
Manuscript ID	BRAIN-2019-00971.R1
Manuscript Type:	Original Article
Date Submitted by the Author:	15-Nov-2019
Complete List of Authors:	Gao, Yunan; Imperial College London, Medicine Irvine, Elaine ; Imperial College London Eleftheriadou, Ioanna; Imperial College London Jiménez Naranjo, Carlos ; Imperial College London Hearn-Yeates, Francesca ; Imperial College London Bosch, Leontien; Imperial College London Glegola, Justyna ; Imperial College London Murdoch, Leah ; Imperial College London Czerniak, Aleksandra ; Imperial College London Meloni, Ilaria ; University of Siena Renieri, Alessandra ; University of Siena Kinali, Maria ; Portland Hospital for Women and Children Mazarakis, Nicholas; Imperial College London, Medicine
Subject category:	Genetics
To search keyword list, use whole or part words followed by an *:	Gene therapy < GENETICS, Childhood epilepsy < EPILEPSY AND SLEEP, Motor control < MOVEMENT DISORDERS, Brain development < SYSTEMS/DEVELOPMENT/PHYSIOLOGY, Stem cells < NEURODEGENERATION: CELLULAR AND MOLECULAR, Cerebellar function < MOVEMENT DISORDERS, Autistic spectrum disorder < NEUROPSYCHIATRY

Gene replacement ameliorates deficits in mouse and human models of cyclin-dependent kinase-like 5 disorder

Yunan Gao[1], Elaine E. Irvine[2], Ioanna Eleftheriadou[1], Carlos Jiménez Naranjo[1], Francesca Hearn-Yeates[1], Leontien Bosch[1], Justyna A. Glegola[2], Leah Murdoch[3], Aleksandra Czerniak[3], Ilaria Meloni[4], Alessandra Renieri[4], Maria Kinali[5] & Nicholas D. Mazarakis[1*]

[1]Gene Therapy, Centre of Neuroinflammation and Neurodegeneration, Division of Brain Sciences, Faculty of Medicine, Imperial College London, Hammersmith Hospital Campus, London W12 0NN, UK

[2]Metabolic Signalling Group, MRC London Institute of Medical Sciences, Imperial College London, London W12 0NN, UK

[3]CBS Imperial College London, Hammersmith Hospital Campus, London W12 0NN, UK

[4]Medical Genetics, Department of Medical Biotechnologies, University of Siena, Siena, Italy

[5]The Portland Hospital, 205-209 Great Portland Street, London, W1W 5AH, UK

*corresponding author. Tel: +44(0)2075947024: E-mail: n.mazarakis@imperial.ac.uk

Running title: Gene therapy in models of CDKL5 disorder

Abstract

Cyclin-dependent kinase-like 5 disorder is a severe neurodevelopmental disorder caused by mutations in the X-linked cyclin-dependent kinase-like 5 ~~(*CDKL5*)~~ gene. It predominantly affects females that typically present with severe early epileptic encephalopathy, global developmental delay, motor dysfunction, autistic features and sleep disturbances. To develop a gene replacement therapy, we initially characterised the human cyclin-dependent kinase-like 5 transcript isoforms expressed in the brain, neuroblastoma cell lines, primary astrocytes and embryonic stem cell-derived cortical interneurons. We found that the isoform 1 and to a lesser extent the isoform 2 were expressed in human brain, and both neuronal and glial cell types. These isoforms were subsequently cloned into recombinant adeno-associated viral ~~(AAV)~~ vector genome and high-titre viral vectors were produced. Intrajugular delivery of green fluorescence protein via adeno-associated viral vectors serotype PHP.B in adult wild-type male mice transduced neurons and astrocytes throughout the brain more efficiently than serotype 9. Cyclin-dependent kinase-like 5 knockout male mice treated with the isoform 1 via intrajugular injection at age 28-30 days exhibited significant behavioural improvements compared to green fluorescence protein-treated controls (1×10^{12} vg per animal, n = 10 per group) with PHP.B vectors. Brain expression of the isoform 1 transgene was more abundant in hindbrain than forebrain and midbrain. Transgene brain expression was sporadic at the cellular level and most prominent in hippocampal neurons and cerebellar Purkinje cells. Correction of postsynaptic density protein 95 cerebellar misexpression, a major fine cerebellar structural abnormality in ~~*Cdkl5*~~ knockout mice, was found in regions of high transgene expression within cerebellum. Adeno-associated viral vectors serotype DJ efficiently transduced cyclin-dependent kinase-like 5-mutant human induced pluripotent stem cell-derived neural progenitors, which were subsequently differentiated into mature neurons. When treating ~~*CDKL5*~~-mutant neurons, isoform 1 expression led to an increased density of synaptic puncta, whilst isoform 2 ameliorated the calcium signalling defect compared to green fluorescence protein control, implying distinct functions of these isoforms in neurons. This study provides the first evidence that gene therapy mediated by adeno-associated viral vectors can be utilised for treating the cyclin-dependent kinase-like 5 disorder.

Keywords: AAV gene therapy/autism/CDKL5/hiPSC/motor deficits

Abbreviations

2-ME	2-Mercaptoethanol
aa	Amino acid
AAV	Adeno-associated virus
ADHD	Attention deficit hyperactivity disorder
aEB	Adherent embryoid bodies
ASD	Autism spectrum disorder
BBB	Blood-brain barrier
BGH	Bovine growth hormone
CA1	Cornu Ammonis 1
CB	Calbindin D-28k
CBA	Chicken β-actin
CBh	CBA hybrid
CDS	Coding sequence
CGH	Comparative genomic hybridization
CS	Conditioned stimulus
DMEM	Dulbecco's modified Eagle's medium
DRG	Dorsal root ganglia
EMEM	Minimum essential medium Eagle
FACS	Fluorescence-activated cell sorting
FBS	Fetal bovine serum
GSP	Gene-specific primer
HBSS	Hanks' balanced salt solution
HEK	Human embryo kidney
hESC	Human embryonic stem cell
ICC	Immunocytochemistry
IHC	Immunohistochemistry
iPSC	Induced pluripotent stem cell
ITR	Inverted terminal repeat
KO	Knockout
KRH	Krebs-Ringer HEPES
NC	Negative control
NEAA	Non-essential amino acids

NHP	Non-human primate
NMDA	N-methyl-D-aspartate
NPC	Neural progenitor cell
NTC	Non-template control
pA	BGH polyA
PBS	Phosphate buffered saline
PEI	Polyethylenimine
PEG	Poly(ethylene glycol)
PM	Purmorphamine
PVDF	Immobilon-P polyvinylidene fluoride
RACE	Rapid amplification of cDNA ends
SDS-PAGE	Sodium dodecyl sulfate-polyacrylamide gel electrophoresis
sEB	Suspension embryoid body
ss	Single-stranded
SV40	Simian vacuolating virus 40
TFR	Transferrin receptor
UPM	Universal Primer A Mix
UTR	Untranslated region
WB	Western blot
WT	Wild-type

Introduction

CDKL5 disorder, or CDKL5 deficiency disorder, is a severe, neurodevelopmental disease predominantly affecting females, associated with a full spectrum of comorbidities. It is an ultra-rare X-linked dominant disorder caused by *de novo* mutations in the cyclin-dependent kinase-like 5 (*CDKL5*) gene (Bahi-Buisson *et al.*, 2008). Early-onset epilepsy occurs by 3 months of age in over 90% patients (Fehr *et al.*, 2013), though age at onset may vary from 1 to 78 weeks (median 6 weeks) (Fehr *et al.*, 2016). With time severe and global developmental delay develops, whilst gross motor deficits and other abnormalities such as gastrointestinal, sleep and behavioural comorbidities emerge (Bahi-Buisson and Bienvenu, 2012; Fehr *et al.*, 2013; Fehr *et al.*, 2016). Currently, there is no therapy apart from antiepileptic drugs providing poor seizure management (Bahi-Buisson *et al.*, 2008; Fehr *et al.*, 2016). In females, CDKL5 disorder is caused by haploinsufficiency, whilst the corresponding *CDKL5* null genotype in males effects a generally more severe phenotype. Indeed, somatic mosaicism is frequently seen in male cases and is presumed to reduce the probability of embryonic lethality (Masliah-Plachon *et al.*, 2010; Mirzaa *et al.*, 2013; Mei *et al.*, 2014).

The human *CDKL5* gene is located on the Xp22.13 region of the X chromosome (Montini *et al.*, 1998; Kalscheuer *et al.*, 2003). It is composed of 27 exons: the first 6 exons (exons 1, 1a to 1e) are untranslated, whilst the remaining 21 exons (exons 2 – 22) encode a serine/threonine kinase (Hector *et al.*, 2016). Five major transcript isoforms have been identified, *hCDKL5_1-5*, with *hCDKL5_1* being the most abundant isoform in the CNS (Hector *et al.*, 2016). *hCDKL5_1-4* are ubiquitously expressed, whilst *hCDKL5_5* is expressed only in the adult testes and foetal brain (Hector *et al.*, 2016). The majority of the *CDKL5* coding region is orthologous and well-conserved between human, rat and mouse (Hector *et al.*, 2016, 2017a). Over a hundred pathogenic mutations have been reported thus far in CDKL5 disorder, consisting of point mutations throughout the *CDKL5* coding sequence, and X-chromosomal rearrangements involving part or all of the *CDKL5* gene (Kalscheuer *et al.*, 2003; Van Esch *et al.*, 2007; Tzschach *et al.*, 2008; Thorson *et al.*, 2010; Fehr *et al.*, 2015; Hector *et al.*, 2017b).

CDKL5 protein is a serine/threonine kinase ubiquitously expressed in all tissues, with the highest levels in the brain, thymus and testis (Lin *et al.*, 2005; Rusconi *et al.*, 2008). It consists of an N-terminal catalytic domain and a long C-terminal extension involved in the regulation of the catalytic activity of CDKL5 and its subcellular localization (Lin *et al.*, 2005; Bertani *et al.*, 2006; Rusconi *et al.*, 2008). In the mouse brain, mCdkl5 was reported to be mainly

expressed in neurons but virtually absent in glia (Rusconi *et al.*, 2008). However, rCdkl5 expression was reported in cultured rat glial cells, though at lower level than in cultured rat cortical neurons, and as distinct glial isoform (CDKL5b or rCdkl5_1) from neuronal isoform (CDKL5a or rCdkl5_2) (Chen *et al.*, 2010; Hector *et al.*, 2017a). Furthermore, the cellular expression of hCDKL5 was detected in interfascicular glia in the corpus callosum of post-mortem human brain tissue (Rusconi *et al.*, 2008).

CDKL5 appears to have numerous functions in neuronal cells via auto-phosphorylation (Bertani *et al.*, 2006) and phosphorylating various proteins. Firstly, it regulates gene expression, both via phosphorylation of transcription factors MeCP2 and Dnmt1, and HDAC4 that regulates transcription factor MEF2A (Mari *et al.*, 2005; Kameshita *et al.*, 2008; Carouge *et al.*, 2010; Trazzi *et al.*, 2016); and via interaction with the nuclear speckles involved in the pre-mRNA processing (Ricciardi *et al.*, 2009). Secondly, CDKL5 appears to directly impact neuronal morphogenesis via interaction with Rac1 for dendrite growth, palmitoylated PSD95 for spine development, and shootin 1 for neural polarization (Chen *et al.*, 2010; Zhu *et al.*, 2013; Nawaz *et al.*, 2016). Thirdly, CDKL5 regulates synaptic stability and neuronal transmission via phosphorylation of NGL-1 to strengthen the NGL-1/PSD95 association, and Amph 1 to influence synaptic vesicle endocytosis (Ricciardi *et al.*, 2012; Sekiguchi *et al.*, 2013). Furthermore, CDKL5 has been found to regulate microtubule assembly, cilia-based signalling and polarity-based cellular networks via phosphorylation of microtubule-associated proteins MAP1S, EB2 and ARHGEF2, and CEP131 and DLG5 that regulates centrosome function, these being the first physiological substrates of CDKL5 identified in murine and human cells in two recent phosphoproteomic studies (Baltussen *et al.*, 2018; Munoz *et al.*, 2018).

Over the last decade, various CDKL5 disease models have been developed, including *Cdkl5* knockout (KO) mouse and *CDKL5*-mutant human induced pluripotent stem cell (iPSC)-derived neuron models. Three constitutive *Cdkl5* KO mouse models have been generated via deletion of either exon 2 (Okuda *et al.*, 2017), exon 4 (Amendola *et al.*, 2014) or exon 6 (Wang *et al.*, 2012). *Cdkl5* loss of function causes disruption of neural circuit communication and multiple signalling pathways, thereby mimicking certain clinical features of human CDKL5 disorder (Wang *et al.*, 2012; Amendola *et al.*, 2014; Sivilia *et al.*, 2016; Okuda *et al.*, 2017, 2018). The *Cdkl5* KO mice exhibit motor deficits, autistic-like behaviours, and impaired learning and memory. Notably, all the *Cdkl5* KO mouse models available to-date have failed to recapitulate the cardinal symptom of the disorder, the recurrent, unprovoked seizures.

Despite creating several conditional mutants and restricting mutations to different neuronal subsets, there were no unprovoked seizures, indicating either a fundamental difference in generation and propagation of seizures between humans and rodents (Amendola *et al.*, 2014; Tang *et al.*, 2017) and/or an incomplete gene compensation effect. Despite lack of spontaneous seizures, *Cdkl5* KO mice showed significantly enhanced seizure susceptibility in response to N-methyl-D-aspartate (NMDA) relative to wild-type (WT) mice (Okuda *et al.*, 2017).

Human iPSC lines carrying different *CDKL5* mutations have been derived from patients with CDKL5 disorder (Amenduni *et al.*, 2011; Livide *et al.*, 2015). Female clones express either the mutant X-linked *CDKL5* allele or the WT allele as an isogenic control due to X-chromosome inactivation (Amenduni *et al.*, 2011). *CDKL5*-mutant iPSCs can be differentiated into neurons to model CDKL5 disorder *in vitro* compared to the isogenic control. *CDKL5*-mutant iPSC-derived neurons revealed severe deficits in spine density and morphology compared to WT neurons, indicated by the significant reduction in $VGLUT1^+$ and $PSD95^+$ synaptic density, aberrant long and thin spines and lack of SYP^+ pre-synaptic terminals (Ricciardi *et al.*, 2012).

To-date there is no disease-modifying therapy for CDKL5 disorder. Gene replacement therapy is well suited as a strategy for the correction/reversal of CDKL5 disease progression. Adeno-associated virus (AAV) serotype 9 (AAV9) offers a means of widespread transgene delivery to the CNS due to its ability to cross the blood-brain barrier (BBB) (Foust *et al.*, 2009). Following systemic intravascular delivery, AAV9 vectors can extensively transduce both neurons and glia in mouse CNS as well as various peripheral tissues (Dufour *et al.*, 2014; Foust *et al.*, 2009). However, only 2% of global CNS transduction was achieved in non-human primates (NHPs) following an intrathecal route of delivery (Gray *et al.*, 2013). Furthermore, the AAV9-mediated systemic delivery that has gone clinical for spinal muscular atrophy (Mendell *et al*., 2017) transduces predominantly glia in NHP brain and neurons in spinal cord (Bevan *et al*., 2011). AAV-PHP.B vectors, one of the AAV9 variants selected for global CNS transduction, such as AAV-PHP.B vectors injected via retro-orbital vein can transfer genes throughout mouse CNS with at least 40-fold greater efficiency than AAV9 via retro-orbital vein injection (Deverman *et al.*, 2016). In NHPs, systemically delivered AAV-PHP.B led to significantly enhanced transgene expression in the CNS of adult cynomolgus monkeys relative to AAV9 following intravenous administration (Sah *et al.*, 2018), whereas transduced marmoset brain at a similar level to AAV9 (Matsuzaki *et al.*, 2018). In addition, recombinant AAV-DJ capsid, selected through a directed evolution approach, can mediate *in vitro* transduction up to 1 x 10^5-fold higher than AAV9 (Grimm *et al.*, 2008).

In this study, we aimed to develop an effective disease-modifying gene replacement therapy, utilizing AAV-*CDKL5* vectors in *in vivo* and *in vitro* models of CDKL5 disorder. Thus, we cloned and produced AAV9, AAV-DJ and AAV-PHP.B vectors expressing the major *CDKL5* brain isoforms, at high titre and purity. We first investigated the effects of gene transfer of the most abundant brain isoform *in vivo* via intrajugular delivery of AAV-PHP.B-*hCDKL5_1* vectors in a *Cdkl5* KO mouse model; then compared the two brain isoforms *in vitro* via transduction of AAV-DJ-*hCDKL5_1* or -*hCDKL5_2* vectors in a *CDKL5*-mutant iPSC-derived neuron model. Our findings provide the first evidence that AAV-mediated gene replacement therapy could mediate functional recovery in CDKL5 disorder.

Materials and methods

Cell lines, culture and differentiation

Human embryo kidney (HEK) 293 cells were obtained from ECACC (85120602). HEK 293T cells were the derivatives of HEK 293 cells expressing a mutant version of simian vacuolating virus 40 (SV40) large T antigen, obtained from ATCC (HEK 293T/17, CRL-11268™). HeLa cells were obtained from ECACC (93021013). Primary human astrocytes were obtained from Lonza (CC-2565). SH-SY5Y cells are human neuroblastoma cells, thrice-cloned sub-line of bone marrow biopsy-derived line SK-N-SH (Biedler *et al.*, 1978) acquired from ECACC (94030304), which can be used as a dopaminergic neuronal model. SNL cells are mouse SIM strain embryonic fibroblasts, kindly provided by Prof. Vasso Episkopou (Imperial College London, UK). HES-3 *NKX2.1*$^{GFP/w}$ human embryonic stem cells (hESCs) were human embryonic stem cells with a GFP knockin construct inserted into the second exon of *NKX2.1* gene (Goulburn *et al.*, 2011), kindly provided by Prof. Andrew Elefanty (Murdoch Children's Research Institute, Australia). NKX2.1 expression can mark the ventral forebrain-specific identity in the developing CNS (Nicholas *et al.*, 2013). RET849 iPSCs (#13 line carrying a pGlu55fs*74 frameshift mutation in exon 5; and #11 line as isogenic control) were obtained from the Cell lines and DNA bank of Rett Syndrome, X-linked mental retardation and other genetic diseases. See Supplementary methods for cell culture methods.

SH-SY5Y cells were differentiated using 10 μM all trans-retinoic acid (Sigma) for 7 days. HES-3 *NKX2.1*$^{GFP/w}$ hESCs were differentiated into *NKX2.1*-GFP^{+} cortical interneurons using the B27 + 5F method as previously described (Nicholas *et al.*, 2013). RET849 #11 isogenic control and #13 *CDKL5*-mutant iPSCs were differentiated into neural progenitor cells (NPCs) and then NPCs were terminally differentiated into neurons on astrocyte layer as previously described (Kim *et al.*, 2011). See Supplementary methods for detailed differentiation methods.

Rapid Amplification of cDNA Ends (RACE) and RT-PCR

RACE of *CDKL5* was performed using Human Brain Cerebral Cortex Poly A+ RNA (Takara Bio). Generally, the 1st-strand RACE-ready cDNA was synthesized using the SMARTer® RACE cDNA Amplification Kit (Takara Bio); followed by 3'- or 5'- RACE PCR reactions using the Advantage® 2 Polymerase Mix (Takara Bio) according to manufacturer's instructions.

RT-PCR was performed using total RNA purified with RNeasy® Micro Kit (Qiagen) from up to 5 x 10^5 cells or RNeasy® Mini Kit (Qiagen) from up to 1 x 10^7 cells according to manufacturer's instructions. Generally, the 1st-strand cDNA synthesis from RNA was performed using SuperScript® III First-Strand Synthesis SuperMix (Invitrogen) according to manufacturer's instructions. Next, the 1st-strand cDNA was amplified by PCR using Platinum® Taq DNA Polymerase (Invitrogen).

Two gene specific primers (GSPs) were designed to pick up the ends of *CDKL5* cDNA, GSP1 for 5'-RACE and GSP2 for 3'-RACE and RT-PCR. And for 3'-RACE and RT-PCR, two 3'-RACE coding sequence (CDS) primers were designed to amplify the alternative 3'-terminal sequences of *hCDKL5* mRNA, 3'-CDS *hCDKL5_1* primer of exon 19 and 3'-CDS *hCDKL5_5* primer of exon 22 (Fig 1 A; Supplementary Table 1). RACE and RT-PCR products were cloned into the pCR™4-TOPO® vectors (Invitrogen) using TOPO® TA Cloning® Kit for Sequencing (Invitrogen) according to manufacturer's instructions. Positive clones were selected, sequenced and analyzed using DNADynamo (BlueTractorSoftware).

Cloning, production and titre determination of AAV vectors

The *CDKL5* transgene sequences (GenBank: HQ171445.1) were 5' tagged and codon-optimized, synthesized by GeneArt (Thermo), and cloned into single-stranded (ss)AAV vector genome to generate pTR-CBh-HA-*hCDKL5_1*-BGH polyA and pTR-CBh-Myc-*hCDKL5_2*-BGH polyA. pTR-CBh-eGFP-BGH polyA-*LacZ* stuffer vector plasmid was constructed as positive control. See Supplementary methods for detailed cloning methods.

AAV vectors were prepared via 3-plasmid co-transfection of HEK 293T cells using polyethylenimine (PEI) (Polysciences) as previously described (Gray *et al.*, 2011a; Deverman *et al.*, 2016). See Supplementary methods for detailed production methods.

rAAV titres were determined by measuring the number of vector genome extracted using DNeasy Blood & Tissue Kit (Qiagen) via qPCR performed in the Mx3000P QPCR System with MxPro QPCR software (Agilent), with linearized genome plasmid as a standard. The purity of each rAAV vector preparation was examined using SYPRO® Ruby Protein Gel Stain (Invitrogen) according to manufacturer's instructions.

***In vitro* AAV transduction**

For AAV transduction of iPSC-derived NPCs, 8-well glass chamber slides (Thermo) or 24-well plastic plates (Corning) were pre-coated with poly-L-ornithine/laminin. NPCs were seeded at the density of 5 x 10^4 cells in 400 µl medium per well in 8-well slides or 1 x 10^5 cells in 500 µl medium per well in 24-well plates. 24 hours post-seeding, 250 µl medium was removed and 50 µl medium containing AAV-DJ vectors at certain multiplicity of infection (MOI) was added dropwise per well. 6 hours post-transduction, 200 µl medium was topped up per well. 24 hours post-transduction, the transduction medium was replaced with 400 µl or 500 µl fresh culture medium per well in 8-well slides or 24-well plates, respectively. Transduced NPCs were incubated for 4 days and then dissociated for fluorescence-activated cell sorting (FACS) or fixed in slides for ICC staining; or incubated for 3 days and then re-plated on astrocyte layer for terminal differentiation (See Supplementary methods for details).

Animals

All animal procedures were approved by the local ethical committee and performed in accordance with the United Kingdom Animals Scientific Procedures Act (1986) and associated guidelines. The mouse strain C57BL/6 was used for the study of comparing *in vivo* biodistribution of AAV9 and AAV-PHP.B vectors via intrajugular injection. 20 C57BL/6 inbred male mice at 5-week age were supplied by Envigo. The mouse strain B6.129(FVB)-*Cdkl5*$^{tm1.1Joez}$/J, also known as *Cdkl5* KO mice, was used as the *in vivo* model of CDKL5 disorder. This *Cdkl5* KO mouse model was originally generated by deletion of *mCdkl5* exon 6 (Wang *et al.*, 2012). Two hemizygous males (*Cdkl5*$^{-/y}$) and two heterozygous females (*Cdkl5*$^{+/-}$) were imported from The Jackson Laboratory (stock number 021967) and bred according to provider's instructions to establish a colony. The *Cdkl5*$^{-/y}$ and *Cdkl5*$^{+/y}$ mice for testing were produced by crossing *Cdkl5*$^{+/-}$ females with *Cdkl5*$^{-/y}$ males, and *Cdkl5*$^{-/-}$ females with *Cdkl5*$^{+/y}$ males.

***In vivo* AAV delivery**

To compare the biodistribution of AAV9 and AAV-PHP.B vectors via intrajugular injection, a total of 19 male C57BL/6 mice were used at the age of 43 to 51 days. To investigate the therapeutic effects of CDKL5 expression in *Cdkl5* KO mouse model, a total of 20 *Cdkl5*$^{-/y}$ mice were used at the age of 28 to 30 days (Supplementary Table 2). Animals were randomized into each vector group.

Prior to surgery, mice were weighed and deeply anaesthetized by inhalation of a mixture of 1.0 L/min O_2 and 3.0% isoflurane (Merial). Anesthetized mice were placed in a ventral recumbent position and the anesthetic mixture was lowered to 0.5 L/min oxygen and 1.0 – 2.0% isoflurane. A small incision was made lateral to the ventral midline, from the pectoral muscle to the lower neck. The right jugular vein was exposed with blunt dissection. AAV vectors or saline (Supplementary Table 2) were delivered into the systemic circulation through a direct injection using a 29-Gauge 0.5 ml Insulin Syringe (BD) into the right jugular vein at the rate of 100 µl/min. For those mice pre-treated with mannitol, 25% mannitol was injected at 8 µl/g body weight 6 minutes prior to AAV or saline injection.

Behavioural analysis

Behavioural testing was conducted on the *Cdkl5* KO mice group and AAV-injected *Cdkl5* KO mice group (Supplementary Table 3) as follows: open field, hind-limb clasping, rotarod, elevated O-maze, marble burying, social interaction, three-chambered social approach, nesting, Y-maze spontaneous alternation, and contextual and cued fear conditioning. See Supplementary methods for detailed behavioural methods. All the behavioural tests and analysis were performed blindly.

Immunohistochemistry (IHC), microscopy and image analysis

Mice were deeply anaesthetized and transcardially perfused with ice-cold heparin-saline followed by 4% PFA. Then the brain, spinal cord and dorsal root ganglia (DRG) were removed, as well as both eyes and one kidney from each mouse. Tissues were post-fixed in 4% PFA on ice for 2-4 hours. Fixed tissues were transferred to 30% sucrose – NaN_3 until they all sank and then frozen in O.C.T. compound (VWR) for cryo-sectioning. The brains were cryo-sectioned into 35 µm sagittal sections or 30 µm coronal sections of 12 series using a Leica CM1850 Cryostat. Spinal cords and DRGs were cryo-sectioned into 16 µm sagittal sections of 10 series onto SuperFrost Plus Microscope Slides (VWR). Eyes were cryo-sectioned into 18 µm sagittal sections of 8 series and kidneys into 16 µm coronal sections of 20 series onto slides.

IHC staining of free-floating brain sections was conducted in 12-well plates wrapped in aluminium, shaking at 120 rpm. Sections were washed 3 times in phosphate buffered saline (PBS), followed by blocking in 10% goat serum/0.25% Triton X-100/PBS at RT for 1 hour. Then sections were incubated with primary antibodies (Supplementary Table 4) diluted in 10% goat serum/0.25% Triton X-100/PBS for around 40 hours at 4°C. Subsequently, sections were

washed 4 times with PBS and re-blocked in 10% goat serum/0.25% Triton X-100/PBS at RT for 30 minutes. Then sections were incubated with secondary antibodies (Supplementary Table 5) diluted 1:500 in 10% goat serum/0.25% Triton X-100/PBS for 1 hour at RT. Afterwards, sections were washed 5 times with PBS and then mounted onto the SuperFrost Plus Microscope Slides. The slides were mounted with ProLong® Gold Antifade Mountant with DAPI (Invitrogen) and sealed with nail polish.

Tiling images were acquired using a Zeiss Axio Observer Inverted Widefield Microscope (Fig 2 A) or a Nikon Eclipse 80i Fluorescence Microscope (Supplementary Fig 4 A) with 10x objective. Fluorescence images were captured using a Nikon Eclipse TE2000-U Inverted Microscope (Fig 2 B-E; Supplementary Fig 3) or a Leica TCS SP5 Confocal Microscope (Fig 6 B and D; Supplementary Fig 4 C).

For image analysis, the number of animals per group was pre-established and no animal was excluded from the analysis. For the analysis of PSD95 pinceau volume, confocal images were acquired with the oil-immersion x63 lens, x1 scanner zoom, 1024 x 1024 pixels resolution as z series of images taken at 0.5 µm intervals. All images were acquired using the same microscope parameters for analysis purpose. Quantification of the PSD95 pinceau volume in each animal was performed blindly. The PSD95 estimated volume in the pinceau was measured cell-by-cell using Imaris (BitPlane). The PSD95 signal was detected by 3D voxel-based reconstruction of confocal z stacks, followed by surface recognition and finally referred as 'estimated volume' by Imaris as previously described (Sivilia *et al.*, 2016).

Western blot (WB)

Cell lysate was prepared using RIPA Buffer (Thermo) supplemented with 1x Halt™ Protease and Phosphatase Inhibitor Cocktail (Thermo) and 1x EDTA Solution (Thermo) according to manufacturer's instructions. Tissue lysate was prepared via homogenisation straight from frozen using Micropestle (Eppendorf) in 50 mM Tris-HCl pH 7.5, 150 mM NaCl, 1% Triton X-100 and 1 mM EDTA supplemented with 1x Halt™ Protease and Phosphatase Inhibitor Cocktail. Tissue lysate was left to solubilise for 30 minutes on ice and centrifuged at 13,000 x g for 10 minutes at 4 °C. Protein supernatant was stored at -80 °C.

Protein concentration was measured using the Pierce® BCA Protein Assay Kit (Thermo) according to manufacturer's instructions. Equal amount of protein samples was resolved on a 5-12% tris-glycine sodium dodecyl sulfate-polyacrylamide gel electrophoresis (SDS-PAGE)

gel. Afterwards, separated proteins on the gel were transferred onto the Immobilon-P polyvinylidene fluoride (PVDF) membrane (Millipore). The resulting blots were blocked in 5% milk in 0.1% PBS-Tween (v/v) overnight at 4°C. The following day, blots were probed with primary antibodies (Supplementary Table 4) diluted in 5% milk in 0.1% PBS-Tween at RT for 2 hours. The primary antibodies used were listed in Supplementary Table 4. Then blots were washed and incubated with secondary antibodies (Supplementary Table 5) diluted in 5% milk in 0.1% PBS-Tween at RT for 1 hour. Alternatively, rapid processing of blots was conducted using SNAP i.d.® 2.0 Protein Detection System (Millipore) according to manufacturer's instructions. HRPs on immunoblots were detected using the SuperSignal® West Pico Chemiluminescent Substrate (Thermo) according to manufacturer's instructions. The chemiluminescent images of membranes were captured using GeneGnome XRQ imaging system and GeneSys image acquisition software (Syngene). Densitometry analysis on images was performed using FIJI (NIH). Intensity for each band was normalized to the intensity of the corresponding GAPDH band and the relative protein content was expressed as arbitrary units.

Calcium imaging

Calcium imaging was performed on iPSC-derived neurons on day 32 of terminal differentiation using Fluo-4 AM (Invitrogen) as calcium indicator according to manufacturer's instructions. Briefly, cells were washed once with pre-warmed Hanks' balanced salt solution (HBSS) (Gibco) and then incubated with 3 µM fluo-4 AM in the dark at 37°C for 30 minutes. Then the fluo-4-loaded cells were washed once with HBSS, followed by adding 200 µl of 5 mM Krebs-Ringer HEPES (KRH) solution (5 mM KCl, 130 mM NaCl, 1.2 mM KH_2PO_4, 1.2 mM $MgSO_4$, 2 mM $CaCl_2$, 25 mM HEPES and 1.1 mg/ml glucose, pH 7.5) per well. Subsequently, cytosolic calcium changes indicated by fluo-4 in response to 50 mM KCl were observed under the Zeiss Axio Observer Inverted Widefield Microscope with 10x objective at 37°C and recorded at 1 Hz using Zen microscope software (ZEISS). After 30 seconds of recording at basal condition, 200 µl of 95 mM KRH solution (95mM KCl, 40 mM NaCl, 1.2 mM KH_2PO_4, 1.2 mM $MgSO_4$, 2 mM $CaCl_2$, 25 mM HEPES and 1.1 mg/ml glucose, pH 7.5) was added per well to make a final concentration of 50 mM KCl, followed by further recording for at least 2.5 minutes. FIJI-based plugin Time Series Analyzer was used to analyse the cytosolic calcium changes.

Immunocytochemistry (ICC)

Cells were fixed directly in 8-well chamber slides using 2% PFA prior to staining. Fixed cells were washed 3 times with PBS and permeabilised with 2% BSA/0.1% Triton X-100/PBS at

RT for 10 minutes. After washing twice with PBS and once with 2% BSA/ PBS, cells were blocked with 2% BSA/PBS at RT for 15 minutes. Then cells were incubated with primary antibodies (Supplementary Table 4) diluted in 2% BSA/PBS in the dark at 4°C overnight. The following day, cells were washed three times with 2% BSA/PBS and incubated with secondary antibodies (Supplementary Table 5) diluted 1:400 in 2% BSA/PBS in the dark for 1 hour at RT. After washing three times with PBS, the slides were mounted ProLong® Gold Antifade Mountant with DAPI and sealed with nail polish.

Images were acquired using a Zeiss Axioskop 40FL Microscope (Supplementary Fig 7 C-D; Supplementary Fig 8 A-B) or a Zeiss LSM-780 Inverted Confocal Microscope (Fig 7 A-B, E-G). For synaptic analysis, confocal images were acquired with oil-immersion x63 lens, x1 scanner zoom, 2048 x 2048 pixels resolution as z series of images taken at 0.5 µm intervals. All images were acquired using the same microscope parameters for each experiment. Images were analysed blindly using FIJI software. Synaptic density was measured by automated counting of the number of puncta on secondary dendrites and expressed as the number of puncta per 10 µm dendritic length.

Statistical analysis

Statistical testing was performed in Prism 7 (GraphPad) with 95% confidence interval of difference. Two-tailed unpaired t-test, ordinary one-way ANOVA and one-way ANOVA with Tukey's multiple comparisons test, ordinary two-way ANOVA and two-way ANOVA with Tukey's multiple comparisons test, Bonferroni's multiple comparisons test or Sidak's multiple comparisons test were performed as specified in figure legends. A probability level of $P<0.05$ was considered to be statistically significant; *$P<0.05$, **$P<0.01$, ***$P<0.001$, ****$P<0.0001$.

Data availability

Data are available upon request from the corresponding author.

Results

Design and development of AAV-*CDKL5* vectors

To determine which *hCDKL5* isoform would be most suitable for gene replacement therapy, we initially characterised the *CDKL5* transcript isoforms expressed in human cerebral cortex via RACE PCR, which had not been identified when this study began. We found that both *hCDKL5_1* (634 bp product) and *hCDKL5_2* (757 bp product) isoforms were expressed in human brain cerebral cortex and that *hCDKL5_1* is more abundant than *hCDKL5_2* (Fig 1 A-C). We also identified *hCDKL5* isoforms in neuronal cell lines (neuroblastoma cell lines including undifferentiated and differentiated SH-SY5Y cells, and hESC-derived cortical interneurons) and glia (primary human astrocytes) via RT-PCR. We found that *hCDKL5_1* and to a lesser extent *hCDKL5_2* isoforms were expressed in both neuronal and glial cell types (Fig 1 A-C). In addition, both *hCDKL5_1* and *hCDKL5_5* (915 bp product) isoforms were expressed in human testis whilst *hCDKL5_5* was expressed exclusively in the adult testis (Fig 1 A-C). These results were consistent with recently published data, though neither *hCDKL5_3* nor *hCDKL5_4* isoforms were detected in our analysis probably due to their low abundance of less than 5% of total brain isoforms (Hector *et al.*, 2016). It was thus deduced that *hCDKL5* isoforms 1 and/or 2 were the most suitable isoforms to be delivered by AAV vectors as a potential gene therapy for CDKL5 disorder. CDKL5 protein expression was detected in multiple human cell lines at different levels via WB (Fig 1 D). Since human neuronal and glial cells revealed similar cellular expression patterns of *hCDKL5* isoforms (Fig 1 B and D), a hybrid form of the chicken β-actin (CBA) promoter, the CBh promoter, could be used to drive transgene expression, which provides robust, long-term and ubiquitous expression in all CNS cell types *in vivo* (Gray *et al.*, 2011b).

We then cloned the codon-optimised coding region of *hCDKL5_1* and *hCDKL5_2* downstream of the CBh promoter into the ssAAV2 vector genome as follows: pTR-CBh-HA-*hCDKL5_1*-BGH polyA and pTR-CBh-Myc-*hCDKL5_2*-BGH polyA. In addition, pTR-CBh-eGFP-BGH polyA-*LacZ* stuffer vector plasmid was constructed as positive control (Fig 1 E). Next, expression of both transgenes and tags of the constructed AAV vector plasmids in transfected HEK 293T cells were verified via WB, including HA-hCDKL5_1, Myc-hCDKL5_2 and GFP (Fig 1 F). Furthermore, we produced high-titre rAAV vectors pseudotyped with AAV9, the variant capsid AAV-PHP.B for *in vivo* and the hybrid capsid AAV-DJ for *in vitro* applications.

In vivo gene transfer by AAV9 and AAV-PHP.B vectors following intrajugular delivery

To achieve optimal gene transfer in mouse CNS, *in vivo* CNS transduction efficiencies of ssAAV9 and ssAAV-PHP.B vectors were compared following intrajugular delivery into adult WT male mice. Pre-treatment with 25% mannitol before AAV injection has been reported to temporarily open the BBB and increase transduction in the brain following a systemic injection of AAV9 and other AAV serotypes (Fu *et al.*, 2003; McCarty *et al.*, 2009; Fu *et al.*, 2011).

AAV9-eGFP or AAV-PHP.B-eGFP vectors were administrated at a dose of 1 x 10^{12} vg per animal to WT male mice age 43-51 days via intrajugular injection, with saline as negative control (Supplementary Table 2). In total 11 mice were pre-treated with 25% mannitol at 8 µl/g body weight 6 minutes before injection (Supplementary Table 2). *In vivo* AAV transduction indicated by GFP expression was assessed 4 weeks post-injection via IHC. We found that AAV-PHP.B transduced the adult brain with high efficiency via intrajugular delivery (Fig 2 A). With mannitol pre-treatment, AAV-PHP.B transduced 33.215 ± 25.785% of the whole brain, higher than that of AAV9 (0.560 ± 0.284%) (Fig 2 F). When injected without mannitol pre-treatment, AAV-PHP.B transduced 54.293 ± 19.968 % of the whole brain, significantly higher than that of AAV9 (1.733 ± 0.409%) (Fig 2 F). Thus, pre-treatment with 25% mannitol before AAV injection did not enhance AAV transduction in the brain following intrajugular injection of AAV9 or AAV-PHP.B vectors. Furthermore, both AAV9 and AAV-PHP.B vectors transduced $NeuN^+$ neurons in cortex, hippocampus, striatum and thalamus, as well as other cell types (Fig 2 B; Supplementary Fig 3). In cerebellum, $NeuN^+$ granular layers exhibited little GFP expression whilst Purkinje cells revealed high GFP expression (Fig 2 B; Supplementary Fig 3). In each brain region examined, AAV-PHP.B provided much greater gene transfer than AAV9 (Supplementary Fig 3).

Brain cell types transduced by AAV-PHP.B via intrajugular injection were examined via co-localization of GFP with cell markers: neuronal marker NeuN, astrocytic marker GFAP and dopaminergic neuronal marker TH. In addition to $NeuN^+$ neurons (Fig 2 B; Supplementary Fig 3), AAV-PHP.B also transduced $GFAP^+$ astrocytes in cortex, hippocampus and striatum, as well as TH^+ dopaminergic neurons in substantia nigra and Purkinje cells in cerebellum (Fig 2 B). Next, fractions of $NeuN^+$ neurons transduced by AAV-PHP.B were quantified in different brain regions, which revealed that AAV-PHP.B transduced 11.9 ± 1.868% $NeuN^+$ neurons in cortex, 7.967 ± 0.491% in striatum, 36.73 ± 6.347% in hippocampus and 15.4 ± 5.549% in thalamus (Fig 2 G). GFP expression was detected in both neurons and glial cells, as expected from using the CBh promoter (Fig 2 B; Gray *et al.*, 2011b). Tropism of AAV9 and AAV-PHP.B to various regions, such as hippocampal Cornu Ammonis 1 (CA1) subregion (Fig 2

A-B and G; Supplementary Fig 3), was similar to previous findings (Deverman *et al.*, 2016), indicating increased density and sharing of entry receptor of AAV-PHP.B relative to AAV9.

In addition, AAV-PHP.B transduction was investigated in mouse spinal cord and DRGs. GFP expression was observed in spinal cords and DRGs of AAV-PHP.B-injected mice (Fig 2 C). Due to the auto-fluorescence of DRGs from saline-injected mice, the green fluorescence intensity ratio of AAV-PHP.B to saline was quantified in small (<25 µm), intermediate (25-40 µm) and large (>40 µm) diameter DRG neurons (Renganathan *et al.*, 2000; Deshmukh, 2018) to verify the AAV-PHP.B transduction of DRGs. DRGs of AAV-PHP.B-injected mice showed 20-50% increase in green fluorescence signal compared to saline-injected ones (Fig 2 H), demonstrating AAV-PHP.B transduction of DRGs.

Moreover, AAV-PHP.B transduction was examined in a few mouse peripheral tissues including retina and kidney. In mouse retina, GFP expression was observed in different cell types throughout multiple layers (Fig 2 D). In mouse kidney, GFP expression was observed in both renal cortex and medulla (Fig 2 E).

To conclude, we found that AAV-PHP.B could cross the BBB with no need for mannitol pre-treatment, and transduced neurons and astrocytes throughout the mouse brain with significantly higher efficiency than AAV9. Spinal cord, DRGs, kidney and retina were also transduced by AAV-PHP.B vectors via this route. These data confirmed the previous findings that ssAAV-PHP.B vectors injected via the retro-orbital vein could transfer genes throughout the mouse CNS much more efficiently than ssAAV9 and transduce the majority of astrocytes and neurons across multiple CNS regions (Deverman *et al.*, 2016). The intrajugular route (Dufour *et al.*, 2014) chosen here was demonstrated to target CNS widely and safely, being considered more translational than the retro-orbital route that requires ophthalmic expertise.

Behavioural improvements in *Cdkl5* KO mice following AAV-PHP.B-*hCDKL5_1* gene delivery

The behavioural profile of adult *Cdkl5* KO male mice (*Cdkl5*$^{-/y}$) was initially characterised in comparison with their WT male littermates (*Cdkl5*$^{+/y}$) (Supplementary Table 3). We found that *Cdkl5* KO mice exhibited hyperactivity in open field test (Fig 3 A), impaired motor coordination in rotarod test (Fig 3 B), abnormal clasping in hind-limb clasping test (Fig 3 C), decreased repetitive behaviour in marble burying test (Fig 3 D), impaired nesting behaviour in nesting test (Fig 3 E), abnormal social interaction in social interaction test (Fig 3 F), normal

sociability whilst impaired social novelty in three-chambered social approach test (Fig 3 G), normal anxiety in elevated O-maze test (Fig 3 H), impaired spontaneous alteration in Y-maze test (Fig 3 I), and impaired contextual and cued fear memory in fear conditioning tests (Fig 3 J-K), when compared to WT littermates. These deficits in motor functions, social behaviours, and learning and memory observed in *Cdkl5* KO mice relative to WT (Fig 3) were consistent with previously published data (Wang *et al.*, 2012; Jhang *et al.*, 2017).

To investigate the therapeutic effects of CDKL5 expression in the *Cdkl5* KO mouse model, we injected 10 *Cdkl5*$^{-/y}$ mice with AAV-PHP.B-HA-*hCDKL5_1* and another 10 *Cdkl5*$^{-/y}$ mice with AAV-PHP.B-eGFP, at 1 x 10^{12} vg per animal via intrajugular delivery at a juvenile stage of 28-30 days (Supplementary Table 2). One month after injection, a battery of behavioural tests, which were the same tests performed in behaviourally characterising the *Cdkl5* KO mice (Fig 3), were conducted on the AAV-injected *Cdkl5* KO mice (Supplementary Table 3) to look for any improvement resulting from CDKL5 expression, including open field, rotarod, hind-limb clasping, marble burying, nesting, social interaction, three-chambered social approach, elevated O-maze, Y-maze spontaneous alternation, and contextual and cued fear conditioning. For comparison, 7 saline-treated same-age *Cdkl5*$^{+/y}$ mice were included as positive control. Among them, significant improvements were observed only in a subset of behavioural tests performed (Fig 4). No significant improvements were observed in other behavioural tests performed.

In the hind-limb clasping test, the clasping score of hCDKL5_1-treated *Cdkl5*$^{-/y}$ mice was significantly decreased compared to the GFP-treated ones, though not as low as the clasping score of *Cdkl5*$^{+/y}$ mice. This indicated amelioration in hind-limb clasping in hCDKL5_1-treated *Cdkl5*$^{-/y}$ mice (Fig 4 A). In the marble burying test, hCDKL5_1-treated *Cdkl5*$^{-/y}$ mice buried significantly more marbles in total than GFP-treated mice, though not as many as *Cdkl5*$^{+/y}$ mice. Such results demonstrated that deficits in repetitive behaviours – which are thought to reflect an autistic phenotype – were partially restored after hCDKL5_1 treatment (Fig 4 B). Moreover, in the rotarod test, hCDKL5_1-treated *Cdkl5*$^{-/y}$ mice exhibited a rising trend in latency to fall across 9 trials in 3 days. At day 3, hCDKL5_1-treated *Cdkl5*$^{-/y}$ mice showed a significantly higher latency to fall than the GFP-treated ones and almost as high a latency as *Cdkl5*$^{+/y}$ mice (Fig 4 C left). Furthermore, the average latency to fall for all 3 days was significantly higher in hCDKL5_1-treated *Cdkl5*$^{-/y}$ mice than in GFP-treated ones, though not as high as *Cdkl5*$^{+/y}$ mice (Fig 4 C right). Together, these data demonstrated partial restoration of motor coordination in hCDKL5_1-treated *Cdkl5*$^{-/y}$ mice (Fig 4 C).

Nevertheless, in the contextual fear conditioning test, hCDKL5_1-treated *Cdkl5*$^{-/y}$ mice showed no significant improvement in the percentage of time freezing compared to the GFP-treated ones, with only a slight trend towards *Cdkl5*$^{+/y}$ mice (Fig 4 D). Interestingly, in the open field test, hCDKL5_1-treated *Cdkl5*$^{-/y}$ mice, which showed a trend of increased hyperactivity compared to GFP-treated ones, were significantly more hyperactive than *Cdkl5*$^{+/y}$ mice. Thus, hCDKL5_1 expression caused a trend of increased hyperactivity in *Cdkl5*$^{-/y}$ mice beyond expectation (Fig 4 E).

Correction of PSD95 misexpression in cerebellum of *Cdkl5* KO mice following AAV-PHP.B-*hCDKL5_1* gene therapy

Brains from *Cdkl5*$^{-/y}$ mice injected with AAV-PHP.B-eGFP or AAV-PHP.B-HA-*hCDKL5_1* vectors were harvested 3 months post-injection when all the behavioural tests were completed, as well as their saline-injected *Cdkl5*$^{+/y}$ and *Cdkl5*$^{-/y}$ littermates. AAV-PHP.B distribution in *Cdkl5*$^{-/y}$ mouse brain indicated by GFP expression was assessed via IHC relative to saline-injected *Cdkl5*$^{-/y}$ mouse brain (Supplementary Fig 4 A-B). AAV-PHP.B-eGFP transduced 52.21 ± 6.869% of the whole brain (Supplementary Fig 4 B). AAV-PHP.B-mediated hCDKL5_1 expression level in *Cdkl5* KO mice was closer to the WT Cdkl5 level in the hindbrain (Fig 5) than in the forebrain and midbrain (Supplementary Fig 5 A-B). hCDKL5_1-treated *Cdkl5*$^{-/y}$ mice showed a trend of increased expression of CaMKII-α in forebrain and midbrain (Supplementary Fig 5 A and D) and decreased expression of PSD95 in hindbrain (Supplementary Fig 6 A-B) compared to GFP-treated ones. CaMKII-α expression was not detected in hindbrain by WB (Supplementary Fig 6 A). HA-*hCDKL5_1* transgene brain expression as indicated by HA immunofluorescence was sparse at the cellular level and detected primarily at specific regions such as the hippocampal CA1 region, cerebellar Purkinje cells and cortical neurons (Supplementary Fig 4 C).

To elucidate the neurobiological substrate of the significant motor improvements in hCDKL5_1-treated *Cdkl5*$^{-/y}$ mice, cerebellar regions with relatively high HA-hCDKL5_1 expression in Purkinje cells were first selected (Fig 6 A-C). The cerebellum was divided into 5 regions based on lobules for quantification purposes (White and Sillitoe, 2013): region a, lobules I – III; region b, lobules IV – V; region c, lobules VIa, VIb and VII; region d, lobules VIII – IX; and region e, lobule X (Fig 6 A). Relative HA fluorescence intensity was quantified on 50-84 Purkinje cells from 5 mice for each region (Fig 6 B-C). Quantitative analysis revealed that Purkinje cells in regions a (68.97 ± 1.173) and b (68.83 ± 1.051) had significantly higher

HA expression than those in regions c (60.69 ± 0.7342), d (61.11 ± 0.9196) and e (65.80 ± 0.5386) (Fig 6 C). Thus, regions a and b, which formed the anterior domain of the cerebellar vermis (Fig 6 A), had relatively high hCDKL5_1 expression among cerebellar regions. Taken together, the anterior domain of cerebellum was demonstrated to have the highest hCDKL5_1 expression in Purkinje cells delivered by AAV-PHP.B vectors via the intrajugular route.

Motor deficits associated with *CDKL5* mutation have been preliminarily attributed to the impaired development of GABAergic cerebellar network, including altered inhibitory pathways, and fine cerebellar structural abnormalities such as increased estimated volume of $PSD95^+$ pinceau (Sivilia *et al.*, 2016). Thus, we examined potential alterations in fine anatomical structures in the anterior domain of cerebellar vermis in hCDKL5_1-treated $Cdkl5^{-/y}$ mice relative to GFP-treated ones. $PSD95^+$ pinceau was formed by the ramified axons of basket cells embracing the initial segment of cerebellar Purkinje cells (Iwakura *et al.*, 2012). It has been reported that the estimated volume of $PSD95^+$ pinceau was significantly increased in $Cdkl5^{-/-}$ mice compared to $Cdkl5^{+/+}$ mice (Sivilia *et al.*, 2016). Hence, the $PSD95^+$ pinceau volume in the anterior domain of cerebellar vermis was compared between hCDKL5_1-treated and GFP-treated $Cdkl5^{-/y}$ mice, to investigate any restoration following CDKL5 expression. Mouse cerebellum was co-labelled with cerebellar Purkinje cell marker Calbindin D-28k (CB) and pinceau marker PSD95. The cerebellar Purkinje cells exhibited strong CB staining, with $PSD95^+$ pinceau surrounding their axon hillock (Fig 6 D). Quantitative analysis revealed that $PSD95^+$ pinceau volume in the anterior domain of cerebellar vermis was significantly decreased in hCDKL5_1-treated $Cdkl5^{-/y}$ mice (282.8 ± 12.18) compared to GFP-treated ones (355.2 ± 22.73), demonstrating correction of the abnormal increase of pinceau volume in *Cdkl5* KO mice following CDKL5 expression (Fig 6 E).

Amelioration of synaptic and functional deficits in *CDKL5*-mutant iPSC-derived neurons via AAV-DJ-*hCDKL5_1*/*hCDKL5_2* gene therapy

RET849 iPSCs were derived from fibroblasts of a 15-year old female patient with CDKL5 disorder and early-onset seizures, which comprised of two cell lines genotypically identical except for CDKL5 expression. The #13 line was the *CDKL5*-mutant iPSC, which carried a pGlu55fs*74 frameshift mutation in exon 5 in the kinase domain of *CDKL5* gene; the #11 line was the isogenic control from the same patient.

We first characterized the RET849 iPSC lines to confirm its pGlu55fs*74 mutation, null CDKL5 expression, embryonic stem cell-like pluripotency, and normal karyotype. The #13

mutant line was demonstrated to have a deletion of GAAA in the *CDKL5* exon 5 relative to the #11 isogenic line (Supplementary Fig 7 A), which caused the pGlu55fs*74 frameshift mutation from amino acid (aa) 55 and a premature truncation at aa 74, resulting in the complete loss of CDKL5 expression in the #13 iPSCs (Supplementary Fig 7 B). Both #11 and #13 iPSCs were validated to possess embryonic stem cell-like pluripotency via immunostaining of hESC markers SSEA4, TRA-1-60 and OCT4 (Supplementary Fig 7 C-D), and a normal 46 XX karyotype without chromosomal rearrangements via array-comparative genomic hybridization (CGH) analysis (Supplementary Fig 7 E-F). Then we differentiated both #11 and #13 iPSCs into NPCs and characterized the iPSC-derived NPCs with neural stem cell markers nestin and SOX1, and telencephalon marker FOXG1, which demonstrated these NPCs exhibiting characteristics of telencephalic neural stem cells (Supplementary Fig 8 A-B). The transduction efficiency of AAV-DJ vectors was tested on NPCs by transducing both #11 and #13 NPCs with AAV-DJ-eGFP vectors at MOIs from 3 x 10^3 to 1 x 10^5 vg per cell for 4 days. At each MOI tested, the %GFP^+ cells of #11 and #13 NPCs were similar and both above 95%. At the lowest MOI 3 x 10^3 vg per cell tested, 95.16% of #11 NPCs and 95.28% of #13 NPCs were GFP^+ (Supplementary Fig 8 C).

To investigate the therapeutic effects of hCDKL5_1 and hCDKL5_2 expression mediated by AAV-DJ vectors in *CDKL5*-mutant iPSC-derived neurons, RET849 #13 NPCs were transduced with AAV-DJ-HA-*hCDKL5_1* or AAV-DJ-Myc-*hCDKL5_2* vectors for 3 days, with AAV-DJ-eGFP as negative control, at an MOI of 3 x 10^3 vg per cell (Supplementary Fig 8 E). Next, the #13 NPCs transduced with AAV-DJ vectors, as well as the non-transduced #11 and #13 NPCs, were re-plated on astrocyte layers for 1 day and then terminally differentiated into neurons for 32 days (Supplementary Fig 8 D-E).

After terminal differentiation, we first investigated the deficits in synaptic contacts and functionality of #13 *CDKL5*-mutant neurons compared to #11 isogenic control neurons. Non-transduced #11 and #13 neurons were double stained with neuronal marker TUJ1 and glutamatergic neuronal marker VGLUT1 to characterize excitatory neurons. The #11 and #13 $TUJ1^+$ neurons (Fig 7 A-B) exhibited robust staining of VGLUT1 along the dendrites, demonstrating that excitatory neurons were generated via iPSC differentiation. Quantitative analysis showed a slight trend of decreased $VGLUT1^+$ puncta density on secondary dendrites in #13 neurons (17.59 ± 1.191 puncta per 10 μm) compared to #11 neurons (19.1 ± 1.281 puncta per 10 μm), although this was not statistically significant (Fig 7 C).

In addition, Ca^{2+} imaging was performed using fluo-4 AM on non-transduced #11 and #13 neurons. Both neurons and astrocytes were loaded with fluo-4 (Supplementary Fig 9 A and C). However, when given 50 mM KCl after 30 seconds of baseline recording, only neurons would show an increase in fluo-4 fluorescence, indicating the Ca^{2+} transient influxes. Changes of fluo-4 fluorescence were normalised to the basal fluorescence during the first 20 seconds throughout the 3-minute recording as ratios of the fluorescence change and basal fluorescence ($\Delta F/F_0$). Among the KCl-responding cells, both the #11 and #13 neurons depolarised immediately after the application of 50 mM KCl and reached the peak of around 40% $\Delta F/F_0$. After the peak, $\Delta F/F_0$ of #11 neurons decreased steadily throughout the remaining 2.5 minutes to below 10%. On the other hand, $\Delta F/F_0$ of #13 neurons decreased rapidly within the first minute but then stayed almost unchanged at approximately 13% for the remaining 1.5 minutes (Fig 7 D; Supplementary Fig 9 B and D). This indicated that the *CDKL5*-mutant neurons had functional defects in neuronal activity, specifically in maintaining high concentration of cytosolic Ca^{2+} and recovering to basal state.

Next, the #13 *CDKL5*-mutant neurons transduced by AAV-DJ vectors were double-stained with one of the transgene markers (GFP, HA or Myc) and VGLUT1, to confirm *hCDKL5* transgene expression in glutamatergic neurons (Fig 7 E-G). Among the AAV-DJ-transduced #13 neurons, *hCDKL5_1* expression significantly increased synaptic density of $VGLUT1^+$ puncta along the secondary dendrites (16.58 ± 1.074 puncta per 10 µm) whilst *hCDKL5_2* enhanced the $VGLUT1^+$ puncta density but not in a statistically significant manner (14.41 ± 1.706 puncta per 10 µm), when compared with neurons expressing GFP (12.79 ± 1.191 puncta per 10 µm) (Fig 7 H). Interestingly, the #13 neurons transduced with AAV-DJ-*hCDKL5* vectors showed distinct KCl-induced Ca^{2+} signalling patterns (Fig 7 I). #13 neurons expressing hCDKL5_2 exhibited a $\Delta F/F_0$ curve similar to that of the #11 neurons, with a steadily decreasing curve after the peak compared to the sharp decrease seen with the GFP control (Fig 7 I; Supplementary Fig 9). This indicated that hCDKL5_2 could ameliorate the excitation defects caused by the *CDKL5* mutation. The #13 neurons expressing hCDKL5_1 showed merely a small increase of $\Delta F/F_0$ for less than 10%, but a similar polarization rate to those expressing hCDKL5_2 (Fig 7 I; Supplementary Fig 9).

Discussion

In this study, we show that gene therapy utilizing AAV-CDKL5 vectors ameliorates deficits in both mouse and iPSC models of CDKL5 disorder. Due to the extensive CDKL5 expression in the CNS in both neurons and glia, AAV-PHP.B vector was selected over AAV9 so as to achieve this widespread expression pattern and thus increase chances of efficacy. AAV-PHP.B-mediated hCDKL5_1 treatment of *Cdkl5* KO male juvenile mice, led to significant improvements in motor functions and autistic-like behaviours compared to GFP-treated controls, due to the hCDKL5_1 expression relatively high in the hindbrain and most prominent in hippocampal CA1 and cerebellar Purkinje neuronal cell layers. In cerebellar regions of high hCDKL5_1 expression, PSD95 cerebellar misexpression was corrected, which is a major fine cerebellar structural abnormality associated with motor symptoms in *Cdkl5* KO mice (*Sivilia et al.*, 2016). This indicates that protein re-expression even in the severe form of this disease at early stages could be therapeutic for some deficits. In addition, AAV-DJ-mediated hCDKL5_1 expression in *CDKL5*-mutant iPSC-derived neurons led to an increased density of synaptic puncta, whilst hCDKL5_2 ameliorated the calcium signalling defect compared to GFP control, implying distinct functions of these isoforms in neurons. Thereby we provide the first evidence that AAV-mediated gene therapy can be utilised for treating CDKL5 disorder.

For *in vivo* study, we used the B6.129(FVB)-*Cdkl5*$^{tm1.1Joez}$/J as the *Cdkl5* KO mouse model, which was originally generated by deletion of *mCdkl5* exon 6 (Wang *et al.*, 2012). *Cdkl5*$^{-/y}$ mice were used as the *in vivo* model of CDKL5 disorder in this study, although CDKL5 patients are mostly female heterozygotes, and some male hemizygotes with generally a more severe phenotype than in females caused by haploinsufficiency. Theoretically, *Cdkl5*$^{+/-}$ mice should be used to model CDKL5 female patients whilst *Cdkl5*$^{-/y}$ mice for male patients in translational studies. Nevertheless, *Cdkl5*$^{+/-}$ mice exhibited behavioural, cellular and molecular abnormalities at intermediate levels between *Cdkl5*$^{-/-}$ and *Cdkl5*$^{+/+}$ littermates. Moreover, multiple deficits in *Cdkl5*$^{+/-}$ mice showed slight but not as significant differences as in *Cdkl5*$^{-/-}$ mice compared to *Cdkl5*$^{+/+}$ mice, which might be due to a mosaic of KO and WT cells caused by X-chromosome inactivation (Amendola *et al.*, 2014; Fuchs *et al.*, 2014, 2018b). Such minor deficits in *Cdkl5*$^{+/-}$ mice are likely to hinder the assessment of potential improvements led by therapeutics. On the other hand, *Cdkl5*$^{-/y}$ mice exhibited distinct and significant impairments relative to *Cdkl5*$^{+/y}$ littermates (Wang *et al.*, 2012; Amendola *et al.*, 2014; Fuchs *et al.*, 2014; Pizzo *et al.*, 2016; Okuda *et al*, 2017, 2018), thus have been used in multiple translational studies of CDKL5 disorder to-date (Fuchs *et al.*, 2015, 2018a; Della Sala *et al.*, 2016; Trazzi

et al., 2018). Therefore, for the proof of concept purpose in the first gene therapy study of CDKL5 disorder, we considered the *Cdkl5*$^{-/y}$ mice to be more suitable as the *in vivo* disease model than *Cdkl5*$^{+/-}$ mice. We found that adult *Cdkl5* KO male mice exhibited hyperactivity, abnormal clasping, impaired motor coordination, decreased repetitive behaviour, abnormal social interaction and social novelty, impaired nesting, and deficits in learning and memory when compared to WT, which confirmed the published behavioural data (Wang *et al.*, 2012; Jhang *et al.*, 2017).

The behavioural deficits identified in *Cdkl5* KO mouse model were consistent with many of the phenotypes observed in CDKL5 patients. The impaired motor coordination and balance in mice in rotarod test may mimic the impaired ambulation and gait dyspraxia in patients (Fehr *et al.*, 2015). Moreover, the hind-limb clasping may model the hand-wringing stereotypy in patients (Li *et al.*, 2008; Lalonde and Strazielle, 2011), though human phenotype lacks the postural component displayed in mice. In addition, the abnormal social interaction and social novelty, reduced repetitive/perseverative behaviours evaluated by marble burying test, and impaired nesting behaviour in mice, which are phenotypes in mouse models of autism spectrum disorder (ASD), resemble the ASD-like phenotypes in patients ((Jhang *et al.*, 2017; Xiong *et al.*, 2019). Furthermore, the deficits in learning and memory in fear conditioning tests can be linked to the severe intellectual disability in patients (Bahi-Buisson and Bienvenu, 2012).

Following single gene delivery of AAV-PHP.B-*hCDKL5_1*, young *Cdkl5* KO mice exhibited significant improvements in motor deficits in hind-limb clasping and rotarod tests, and reduced autistic-like behavioural deficits in marble burying tests, in comparison with GFP-treated ones. The hind-limb clasping of *Cdkl5* KO mice mimicking hand-wringing stereotypy in patients appears to involve various brain regions including cerebellum, basal ganglia and neocortex (Lalonde and Strazielle, 2011). In addition, the impaired motor coordination and balance in mice measured by rotarod test to model impaired ambulation and gait dyspraxia in patients also involves cerebellum, motor cortex and many other brain regions (Scholz *et al.*, 2015). Therefore, such motor improvements could be attributed to the relatively high hCDKL5_1 expression in the hindbrain, especially the prominent expression in the cerebellar Purkinje cells. Furthermore, the repetitive/perseverative behaviours in mice evaluated by marble burying test have been reported to partially rely on hippocampal function (Deacon and Rawlins, 2005). Thus, the most prominent hCDKL5_1 expression in hippocampal CA1 region might lead to the partial restoration of autistic-like behaviours in *Cdkl5* KO mice. The increased hyperactivity detected upon hCDKL5_1 treatment is difficult to explain; yet it is unlikely to be

due to a gene duplication effect (Szafranski *et al.*, 2015), as both hCDKL5_1-treated mice and GFP controls exhibited hyperactivity.

The mechanism of motor deficits in alternate *Cdkl5* KO mice has been previously reported to involve an increased volume of PSD95$^+$ pinceau, which constitutes the initial segment of cerebellar Purkinje cells (Iwakura *et al.*, 2012; Sivilia *et al.*, 2016). Although PSD95 is mainly associated with the post-synaptic density (PSD) of excitatory synapses throughout the brain (El-Husseini *et al.*, 2000), it is also localised at the pre-synaptic terminals of GABAergic synapses in the adult cerebellum, exclusively in the pinceau (Castejón *et al.*, 2004). We found that abnormal increase of PSD95$^+$ pinceau volume in *Cdkl5* KO mice could be restored in parts of the cerebellum where hCDKL5_1 transduction was robust. As regular pinceau organisation is required for normal motor behaviours, including gait coordination (Bobik *et al.*, 2004; Suárez *et al.*, 2008), it could be that the correction of PSD95 misexpression and pinceau alteration were responsible for the significant motor improvements in hCDKL5_1-treated mice.

Despite significant improvements, behavioural deficits in *Cdkl5* KO mice were partially restored via hCDKL5_1 expression, which might be attributed to the following reasons. First, the distribution pattern of hCDKL5_1 transgene expression in mouse brain was determined by the AAV-PHP.B vector tropism (Deverman *et al.*, 2016): denser in hippocampus and cerebellum whilst sparser in cortex and striatum; which deviated from the Cdkl5 WT expression pattern in rodents: high levels in forebrain (i.e. cortex, hippocampus, striatum and olfactory bulb) whilst low levels in midbrain and hindbrain (Chen *et al.*, 2010; Okuda *et al.*, 2017). Loss of CDKL5 disrupted dopamine synthesis in the cortico-striatal areas, which might underlie the comorbid features of autism and attention deficit hyperactivity disorder (ADHD) in *Cdkl5* KO mice (Jhang *et al.*, 2017). Next, the absence of *hCDKL5_2* co-expression might also be responsible, which contains the brain-specific exon 17 not present in *hCDKL5_1* (Fichou *et al.*, 2011; Hector *et al.*, 2016). Due to volume limitation, simultaneous co-delivery of two vectors, even at the high titres obtained, was not feasible in this study. Additionally, such gene replacement approach might not be able to restore the activity-dependent expression, dephosphorylation and degradation of Cdkl5 at synaptic level (La Montanara *et al.*, 2015) or the neurodevelopmental deficits caused by prenatal absence of Cdkl5 (Hector *et al.*, 2016). Furthermore, there is growing evidence that autistic traits are driven by a widespread synaptopathy in the CNS, necessitating a more robust CNS transduction to mediate behavioural changes (Benger *et al.*, 2018), which might also explain the lack of impact on many such behavioural deficits in this model. Indeed, no rescue of autistic phenotypes and dendritic

dysfunction has been reported following AAV gene therapy in rodent models of other neurodevelopmental disorders, such as Rett syndrome (Garg *et al.*, 2013; Gholizadeh *et al.*, 2014; Gadalla *et al.*, 2017). Some rescue of dendritic spine instability in juvenile *Cdkl5*$^{-/y}$ mice was reported following multiple subcutaneous injections of IGF1 (Della Sala *et al.*, 2016); yet IGF1 has not demonstrated therapeutic efficacy to-date (Costales and Kolevzon 2016). Rescue of neurological phenotypes in *Cdkl5*$^{-/y}$ mice has been reported via CDKL5 protein substitution therapy delivered intracerebroventricularly or intravenously (Trazzi *et al.*, 2018). However, in this study continuous administration was performed and only short-term outcomes were measured.

Cdkl5 KO mouse models available to-date have failed to recapitulate the spontaneous seizures in human disorder, as is often the case with epilepsy modelling in mice. Nevertheless, *Cdkl5*$^{-/y}$ mice showed significantly enhanced seizure susceptibility in response to NMDA relative to *Cdkl5*$^{+/y}$ mice. Severe generalized tonic-clonic seizures could be induced in *Cdkl5*$^{-/y}$ mice via intraperitoneal injection of NMDA (Okuda *et al.*, 2017). Therefore, the alterations in the threshold for triggering epilepsy could be examined (Creson *et al.*, 2019) following gene therapy in *Cdkl5* KO mice, in order to speculate on possible therapeutic effects on seizures in human disorder in future trials.

For *in vitro* study, we used the RET849 iPSCs comprising of #13 *CDKL5*-mutant iPSC line and #11 isogenic control, the only iPSC line available that was completely null in CDKL5 expression due to the mutation in exon 5 affecting the kinase domain. These iPSCs were differentiated into neurons as previously described (Kim *et al.*, 2011). We found that growth on a human astrocyte layer was essential for the derivation of a healthy glutamatergic neuronal population post-differentiation. It has been reported that *CDKL5*-mutant iPSC-derived neurons showed significant reduction in synaptic contacts indicated by VGLUT1^{+} and PSD95^{+} puncta density compared to the isogenic control (Ricciardi *et al.*, 2012). In our study, we found that *CDKL5*-mutant neurons showed a slight trend towards decreased VGLUT1^{+} puncta density on secondary dendrites compared to isogenic control neurons, suggesting a potential decrease in excitatory neurotransmission caused by *CDKL5* deletion. Moreover, the Ca^{2+} influx and efflux processes of *CDKL5*-mutant neurons were abnormal compared to isogenic neurons.

We tested AAV-DJ-*hCDKL5_1/hCDKL5_2* vectors as gene replacement therapy in the *CDKL5*-mutant iPSC-derived neurons, which were treated pre-full neuronal differentiation at the neuronal precursor stage, thus representing an embryonic gene therapy intervention in this

human disorder, though of no translational possibility. Interestingly, these 2 isoforms exhibited distinct effects in phenotypic and functional aspects. In phenotypic studies, *hCDKL5_1* restored the synaptic defect of *CDKL5*-mutant neurons by increasing $VGLUT1^{+}$ puncta density on secondary dendrites relative to GFP, in a trend similar to the isogenic neurons. Nevertheless, no significant improvement of synaptic defects was observed in *hCDKL5_2*-treated *CDKL5*-mutant neurons compared to GFP. In functional studies, the abnormal Ca^{2+} influx and efflux processes of *CDKL5*-mutant neurons could be ameliorated by expression of *hCDKL5_2* rather than *hCDKL5_1* isoform. These data provide the first functional evidence that *hCDKL5_2* is crucial to CDKL5 functions, contrary to previous data (Hector *et al.*, 2017). Both *hCDKL5_1* and *hCDKL5_2* isoforms appear to mediate distinct roles in neurons and thus should probably be co-expressed in the CNS for effective functional replacement. AAV-PHP.B vectors used in our *in vivo* studies were recently shown to transduce NHP CNS regions such as cortex, cerebellum and spinal cord via intrathecal delivery (Liguore *et al*., 2019). This, coupled with clinical applications of AAV vectors via intrathecal route (Bailey *et al*., 2018), open up the potential for such an intervention in CDKL5 disorder. Further studies are now needed to test the efficacy of such an approach and to decide on its translational applicability.

Acknowledgements

We thank Istvan Nagy for advising on calcium imaging, and Paolo La Montanara for advising on calcium imaging and analysis, and analysis of DRG neurons. We also thank Stephen Rothery at the Facility for Imaging by Light Microscopy (FILM) of Imperial College London for use of fluorescent tiling and confocal microscopes and synapse analysis. We are indebted to Mimoun Azzouz for help with AAV iodixanol gradients. We are also grateful to our previous colleagues Nelly Jolinon and Josephine Malmevik for advising on cloning, AAV production and *in vivo* work. We thank Matthew Benger for help in quantification and critical reading of manuscript, and Richard Reynolds for critical reading. We also thank Simone Di Giovanni and Thomas Knöpfel for fruitful discussions. We thank the Cell lines and DNA bank of Rett Syndrome, X-linked mental retardation and other genetic diseases, member of the Telethon Network of Genetic Biobanks (project no. GTB12001), funded by Telethon Italy, and of the EuroBioBank network and the 'Associazione Italiana Rett O.N.L.U.S.', for providing us with iPSC lines. We also thank the National Gene Vector Biorepository (NGVB) for providing AAV plasmids, Benjamin Deverman for AAV-PHP.B plasmid and Dirk Grimm for AAV-DJ plasmid.

Funding

This work was supported by funds from the Division of Brain Sciences, Imperial College London (NDM) and donations from an anonymous donor, Mr and Mrs Gao and Dr S Retsas.

Author contributions

IE, CJN, FH-Y, LB performed experiments; EEI and JAG performed behavioural studies; IM and AR provided cell lines; MK gave clinical advice and co-wrote paper; LM and AC performed mouse breeding; NDM and YG designed the study, obtained funding, performed experiments, supervised the research and co-wrote the paper.

Competing interests

The authors report no competing interests.

References

Amendola E, Zhan Y, Mattucci C, Castroflorio E, Calcagno E, Fuchs C, et al. Mapping pathological phenotypes in a mouse model of CDKL5 disorder. PLoS One 2014; 9(5): e91613.

Amenduni M, De Filippis R, Cheung AY, Disciglio V, Epistolato MC, Ariani F, et al. iPS cells to model CDKL5-related disorders. Eur J Hum Genet 2011; 19(12): 1246-55.

Anagnostaras SG, Gale GD, Fanselow MS. Hippocampus and contextual fear conditioning: recent controversies and advances. Hippocampus 2001; 11(1): 8-17.

Archer HL, Evans J, Edwards S, Colley J, Newbury-Ecob R, O'Callaghan F, et al. CDKL5 mutations cause infantile spasms, early onset seizures, and severe mental retardation in female patients. J Med Genet 2006; 43(9): 729-34.

Ayuso E, Mingozzi F, Montane J, Leon X, Anguela XM, Haurigot V, et al. High AAV vector purity results in serotype- and tissue-independent enhancement of transduction efficiency. Gene Ther 2010; 17(4): 503-10.

Bahi-Buisson N, Bienvenu T. CDKL5-Related Disorders: From Clinical Description to Molecular Genetics. Mol Syndromol 2012; 2(3-5): 137-52.

Bahi-Buisson N, Kaminska A, Boddaert N, Rio M, Afenjar A, Gérard M, et al. The three stages of epilepsy in patients with CDKL5 mutations. Epilepsia 2008; 49(6): 1027-37.

Bailey RM, Armao D, Nagabhushan Kalburgi S, Gray SJ. Development of Intrathecal AAV9 Gene Therapy for Giant Axonal Neuropathy. Mol Ther Methods Clin Dev 2018; 9: 160-71.

Baltussen LL, Negraes PD, Silvestre M, Claxton S, Moeskops M, Christodoulou E, et al. Chemical genetic identification of CDKL5 substrates reveals its role in neuronal microtubule dynamics. EMBO J 2018; 37(24).

Benger M, Kinali M, Mazarakis ND. Autism spectrum disorder: prospects for treatment using gene therapy. Mol Autism 2018; 9: 39.

Bertani I, Rusconi L, Bolognese F, Forlani G, Conca B, De Monte L, et al. Functional consequences of mutations in CDKL5, an X-linked gene involved in infantile spasms and mental retardation. J Biol Chem 2006; 281(42): 32048-56.

Bevan AK, Duque S, Foust KD, Morales PR, Braun L, Schmelzer L, et al. Systemic gene delivery in large species for targeting spinal cord, brain, and peripheral tissues for pediatric disorders. Mol Ther 2011; 19(11): 1971-80.

Biedler JL, Roffler-Tarlov S, Schachner M, Freedman LS. Multiple neurotransmitter synthesis by human neuroblastoma cell lines and clones. Cancer Res 1978; 38(11 Pt 1): 3751-7.

Bobik M, Ellisman MH, Rudy B, Martone ME. Potassium channel subunit Kv3.2 and the water channel aquaporin-4 are selectively localized to cerebellar pinceau. Brain Res 2004; 1026(2): 168-78.

Carouge D, Host L, Aunis D, Zwiller J, Anglard P. CDKL5 is a brain MeCP2 target gene regulated by DNA methylation. Neurobiol Dis 2010; 38(3): 414-24.

Castejón OJ, Fuller L, Dailey ME. Localization of synapsin-I and PSD-95 in developing postnatal rat cerebellar cortex. Brain Res Dev Brain Res 2004; 151(1-2): 25-32.

Chen Q, Zhu YC, Yu J, Miao S, Zheng J, Xu L, et al. CDKL5, a protein associated with rett syndrome, regulates neuronal morphogenesis via Rac1 signaling. J Neurosci 2010; 30(38): 12777-86.

Costales J, Kolevzon A. The therapeutic potential of insulin-like growth factor-1 in central nervous system disorders. Neurosci Biobehav Rev 2016; 63: 207-22.

Creson TK, Rojas C, Hwaun E, Vaissiere T, Kilinc M, Jimenez-Gomez A, et al. Re-expression of SynGAP protein in adulthood improves translatable measures of brain function and behavior. Elife 2019; 8.

Deacon RM. Assessing nest building in mice. Nat Protoc 2006; 1(3): 1117-9.

Deacon RM, Rawlins JN. Hippocampal lesions, species-typical behaviours and anxiety in mice. Behav Brain Res 2005; 156(2): 241-9.

Della Sala G, Putignano E, Chelini G, Melani R, Calcagno E, Michele Ratto G, et al. Dendritic Spine Instability in a Mouse Model of CDKL5 Disorder Is Rescued by Insulin-like Growth Factor 1. Biol Psychiatry 2016; 80(4): 302-11.

Deshmukh VR. Gap Junctions in the Dorsal Root Ganglia. In: Aranda-Abreu GE, Hernández-Aguilar ME, editors. Neurons - Dendrites and Axons. London: IntechOpen; 2018.

Deverman BE, Pravdo PL, Simpson BP, Kumar SR, Chan KY, Banerjee A, et al. Cre-dependent selection yields AAV variants for widespread gene transfer to the adult brain. Nat Biotechnol 2016; 34(2): 204-9.

Dufour BD, Smith CA, Clark RL, Walker TR, McBride JL. Intrajugular vein delivery of AAV9-RNAi prevents neuropathological changes and weight loss in Huntington's disease mice. Mol Ther 2014; 22(4): 797-810.

El-Husseini AE, Schnell E, Chetkovich DM, Nicoll RA, Bredt DS. PSD-95 involvement in maturation of excitatory synapses. Science 2000; 290(5495): 1364-8.

Fehr S, Leonard H, Ho G, Williams S, de Klerk N, Forbes D, et al. There is variability in the attainment of developmental milestones in the CDKL5 disorder. J Neurodev Disord 2015; 7(1): 2.

Fehr S, Wilson M, Downs J, Williams S, Murgia A, Sartori S, et al. The CDKL5 disorder is an independent clinical entity associated with early-onset encephalopathy. Eur J Hum Genet 2013; 21(3): 266-73.

Fehr S, Wong K, Chin R, Williams S, de Klerk N, Forbes D, et al. Seizure variables and their relationship to genotype and functional abilities in the CDKL5 disorder. Neurology 2016; 87(21): 2206-13.

Fichou Y, Nectoux J, Bahi-Buisson N, Chelly J, Bienvenu T. An isoform of the severe encephalopathy-related CDKL5 gene, including a novel exon with extremely high sequence conservation, is specifically expressed in brain. J Hum Genet 2011; 56(1): 52-7.

Foust KD, Nurre E, Montgomery CL, Hernandez A, Chan CM, Kaspar BK. Intravascular AAV9 preferentially targets neonatal neurons and adult astrocytes. Nat Biotechnol 2009; 27(1): 59-65.

Fu H, Dirosario J, Killedar S, Zaraspe K, McCarty DM. Correction of neurological disease of mucopolysaccharidosis IIIB in adult mice by rAAV9 trans-blood-brain barrier gene delivery. Mol Ther 2011; 19(6): 1025-33.

Fu H, Muenzer J, Samulski RJ, Breese G, Sifford J, Zeng X, et al. Self-complementary adeno-associated virus serotype 2 vector: global distribution and broad dispersion of AAV-mediated transgene expression in mouse brain. Mol Ther 2003; 8(6): 911-7.

Fuchs C, Fustini N, Trazzi S, Gennaccaro L, Rimondini R, Ciani E. Treatment with the GSK3-beta inhibitor Tideglusib improves hippocampal development and memory performance in juvenile, but not adult, Cdkl5 knockout mice. Eur J Neurosci 2018a; 47(9): 1054-66.

Fuchs C, Gennaccaro L, Trazzi S, Bastianini S, Bettini S, Lo Martire V, et al. Heterozygous CDKL5 Knockout Female Mice Are a Valuable Animal Model for CDKL5 Disorder. Neural Plast 2018b; 2018: 9726950.

Fuchs C, Rimondini R, Viggiano R, Trazzi S, De Franceschi M, Bartesaghi R, et al. Inhibition of GSK3β rescues hippocampal development and learning in a mouse model of CDKL5 disorder. Neurobiol Dis 2015; 82: 298-310.

Fuchs C, Trazzi S, Torricella R, Viggiano R, De Franceschi M, Amendola E, et al. Loss of CDKL5 impairs survival and dendritic growth of newborn neurons by altering AKT/GSK-3β signaling. Neurobiol Dis 2014; 70: 53-68.

Gadalla KKE, Vudhironarit T, Hector RD, Sinnett S, Bahey NG, Bailey MES, et al. Development of a Novel AAV Gene Therapy Cassette with Improved Safety Features and Efficacy in a Mouse Model of Rett Syndrome. Mol Ther Methods Clin Dev 2017; 5: 180-90.

Garg SK, Lioy DT, Cheval H, McGann JC, Bissonnette JM, Murtha MJ, et al. Systemic delivery of MeCP2 rescues behavioral and cellular deficits in female mouse models of Rett syndrome. J Neurosci 2013; 33(34): 13612-20.

Gholizadeh S, Arsenault J, Xuan IC, Pacey LK, Hampson DR. Reduced phenotypic severity following adeno-associated virus-mediated Fmr1 gene delivery in fragile X mice. Neuropsychopharmacology 2014; 39(13): 3100-11.

Goulburn AL, Alden D, Davis RP, Micallef SJ, Ng ES, Yu QC, et al. A targeted NKX2.1 human embryonic stem cell reporter line enables identification of human basal forebrain derivatives. Stem Cells 2011; 29(3): 462-73.

Gray SJ, Choi VW, Asokan A, Haberman RA, McCown TJ, Samulski RJ. Production of recombinant adeno-associated viral vectors and use in in vitro and in vivo administration. Curr Protoc Neurosci 2011a; Chapter 4: Unit 4.17.

Gray SJ, Foti SB, Schwartz JW, Bachaboina L, Taylor-Blake B, Coleman J, et al. Optimizing promoters for recombinant adeno-associated virus-mediated gene expression in the peripheral

and central nervous system using self-complementary vectors. Hum Gene Ther 2011b; 22(9): 1143-53.

Gray SJ, Nagabhushan Kalburgi S, McCown TJ, Jude Samulski R. Global CNS gene delivery and evasion of anti-AAV-neutralizing antibodies by intrathecal AAV administration in non-human primates. Gene Ther 2013; 20(4): 450-9.

Grimm D, Lee JS, Wang L, Desai T, Akache B, Storm TA, et al. In vitro and in vivo gene therapy vector evolution via multispecies interbreeding and retargeting of adeno-associated viruses. J Virol 2008; 82(12): 5887-911.

Guyenet SJ, Furrer SA, Damian VM, Baughan TD, La Spada AR, Garden GA. A simple composite phenotype scoring system for evaluating mouse models of cerebellar ataxia. J Vis Exp 2010(39).

György B, Meijer EJ, Ivanchenko MV, Tenneson K, Emond F, Hanlon KS, et al. Gene Transfer with AAV9-PHP.B Rescues Hearing in a Mouse Model of Usher Syndrome 3A and Transduces Hair Cells in a Non-human Primate. Mol Ther Methods Clin Dev 2019; 13: 1-13.

Hector RD, Dando O, Landsberger N, Kilstrup-Nielsen C, Kind PC, Bailey ME, et al. Characterisation of CDKL5 Transcript Isoforms in Human and Mouse. PLoS One 2016; 11(6): e0157758.

Hector RD, Dando O, Ritakari TE, Kind PC, Bailey ME, Cobb SR. Characterisation of Cdkl5 transcript isoforms in rat. Gene 2017a; 603: 21-6.

Hector RD, Kalscheuer VM, Hennig F, Leonard H, Downs J, Clarke A, et al. *CDKL5* variants: Improving our understanding of a rare neurologic disorder. Neurol Genet 2017b; 3(6): e200.

Iwakura A, Uchigashima M, Miyazaki T, Yamasaki M, Watanabe M. Lack of molecular-anatomical evidence for GABAergic influence on axon initial segment of cerebellar Purkinje cells by the pinceau formation. J Neurosci 2012; 32(27): 9438-48.

Jhang CL, Huang TN, Hsueh YP, Liao W. Mice lacking cyclin-dependent kinase-like 5 manifest autistic and ADHD-like behaviors. Hum Mol Genet 2017; 26(20): 3922-34.

Kalscheuer VM, Tao J, Donnelly A, Hollway G, Schwinger E, Kübart S, et al. Disruption of the serine/threonine kinase 9 gene causes severe X-linked infantile spasms and mental retardation. Am J Hum Genet 2003; 72(6): 1401-11.

Kameshita I, Sekiguchi M, Hamasaki D, Sugiyama Y, Hatano N, Suetake I, et al. Cyclin-dependent kinase-like 5 binds and phosphorylates DNA methyltransferase 1. Biochem Biophys Res Commun 2008; 377(4): 1162-7.

Kim JE, O'Sullivan ML, Sanchez CA, Hwang M, Israel MA, Brennand K, et al. Investigating synapse formation and function using human pluripotent stem cell-derived neurons. Proc Natl Acad Sci U S A 2011; 108(7): 3005-10.

La Montanara P, Rusconi L, Locarno A, Forti L, Barbiero I, Tramarin M, et al. Synaptic synthesis, dephosphorylation, and degradation: a novel paradigm for an activity-dependent neuronal control of CDKL5. J Biol Chem 2015; 290(7): 4512-27.

Lalonde R, Strazielle C. Brain regions and genes affecting limb-clasping responses. Brain Res Rev 2011; 67(1-2): 252-9.

Li H, Radford JC, Ragusa MJ, Shea KL, McKercher SR, Zaremba JD, et al. Transcription factor MEF2C influences neural stem/progenitor cell differentiation and maturation in vivo. Proc Natl Acad Sci U S A 2008; 105(27): 9397-402.

Liguore WA, Domire JS, Button D, Wang Y, Dufour BD, Srinivasan S, et al. AAV-PHP.B Administration Results in a Differential Pattern of CNS Biodistribution in Non-human Primates Compared with Mice. Mol Ther 2019; 27(11): 2018-37.

Lin C, Franco B, Rosner MR. CDKL5/Stk9 kinase inactivation is associated with neuronal developmental disorders. Hum Mol Genet 2005; 14(24): 3775-86.

Livide G, Patriarchi T, Amenduni M, Amabile S, Yasui D, Calcagno E, et al. GluD1 is a common altered player in neuronal differentiation from both MECP2-mutated and CDKL5-mutated iPS cells. Eur J Hum Genet 2014.

Mari F, Azimonti S, Bertani I, Bolognese F, Colombo E, Caselli R, et al. CDKL5 belongs to the same molecular pathway of MeCP2 and it is responsible for the early-onset seizure variant of Rett syndrome. Hum Mol Genet 2005; 14(14): 1935-46.

Masliah-Plachon J, Auvin S, Nectoux J, Fichou Y, Chelly J, Bienvenu T. Somatic mosaicism for a CDKL5 mutation as an epileptic encephalopathy in males. Am J Med Genet A 2010; 152A(8): 2110-1.

Matsuzaki Y, Konno A, Mochizuki R, Shinohara Y, Nitta K, Okada Y, et al. Intravenous administration of the adeno-associated virus-PHP.B capsid fails to upregulate transduction efficiency in the marmoset brain. Neurosci Lett 2018; 665: 182-8.

McCarty DM, DiRosario J, Gulaid K, Muenzer J, Fu H. Mannitol-facilitated CNS entry of rAAV2 vector significantly delayed the neurological disease progression in MPS IIIB mice. Gene Ther 2009; 16(11): 1340-52.

Mei D, Darra F, Barba C, Marini C, Fontana E, Chiti L, et al. Optimizing the molecular diagnosis of CDKL5 gene-related epileptic encephalopathy in boys. Epilepsia 2014; 55(11): 1748-53.

Mendell JR, Al-Zaidy S, Shell R, Arnold WD, Rodino-Klapac LR, Prior TW, et al. Single-Dose Gene-Replacement Therapy for Spinal Muscular Atrophy. N Engl J Med 2017; 377(18): 1713-22.

Mirzaa GM, Paciorkowski AR, Marsh ED, Berry-Kravis EM, Medne L, Alkhateeb A, et al. CDKL5 and ARX mutations in males with early-onset epilepsy. Pediatr Neurol 2013; 48(5): 367-77.

Montini E, Andolfi G, Caruso A, Buchner G, Walpole SM, Mariani M, et al. Identification and characterization of a novel serine-threonine kinase gene from the Xp22 region. Genomics 1998; 51(3): 427-33.

Muñoz IM, Morgan ME, Peltier J, Weiland F, Gregorczyk M, Brown FC, et al. Phosphoproteomic screening identifies physiological substrates of the CDKL5 kinase. EMBO J 2018; 37(24).

Nawaz MS, Giarda E, Bedogni F, La Montanara P, Ricciardi S, Ciceri D, et al. CDKL5 and Shootin1 Interact and Concur in Regulating Neuronal Polarization. PLoS One 2016; 11(2): e0148634.

Nicholas CR, Chen J, Tang Y, Southwell DG, Chalmers N, Vogt D, et al. Functional maturation of hPSC-derived forebrain interneurons requires an extended timeline and mimics human neural development. Cell Stem Cell 2013; 12(5): 573-86.

Okuda K, Kobayashi S, Fukaya M, Watanabe A, Murakami T, Hagiwara M, et al. CDKL5 controls postsynaptic localization of GluN2B-containing NMDA receptors in the hippocampus and regulates seizure susceptibility. Neurobiol Dis 2017; 106: 158-70.

Okuda K, Takao K, Watanabe A, Miyakawa T, Mizuguchi M, Tanaka T. Comprehensive behavioral analysis of the Cdkl5 knockout mice revealed significant enhancement in anxiety- and fear-related behaviors and impairment in both acquisition and long-term retention of spatial reference memory. PLoS One 2018; 13(4): e0196587.

Pintaudi M, Baglietto MG, Gaggero R, Parodi E, Pessagno A, Marchi M, et al. Clinical and electroencephalographic features in patients with CDKL5 mutations: two new Italian cases and review of the literature. Epilepsy Behav 2008; 12(2): 326-31.

Pizzo R, Gurgone A, Castroflorio E, Amendola E, Gross C, Sassoè-Pognetto M, et al. Lack of Cdkl5 Disrupts the Organization of Excitatory and Inhibitory Synapses and Parvalbumin Interneurons in the Primary Visual Cortex. Front Cell Neurosci 2016; 10: 261.

Renganathan M, Cummins TR, Hormuzdiar WN, Waxman SG. alpha-SNS produces the slow TTX-resistant sodium current in large cutaneous afferent DRG neurons. J Neurophysiol 2000; 84(2): 710-8.

Ricciardi S, Kilstrup-Nielsen C, Bienvenu T, Jacquette A, Landsberger N, Broccoli V. CDKL5 influences RNA splicing activity by its association to the nuclear speckle molecular machinery. Hum Mol Genet 2009; 18(23): 4590-602.

Ricciardi S, Ungaro F, Hambrock M, Rademacher N, Stefanelli G, Brambilla D, et al. CDKL5 ensures excitatory synapse stability by reinforcing NGL-1-PSD95 interaction in the postsynaptic compartment and is impaired in patient iPSC-derived neurons. Nat Cell Biol 2012; 14(9): 911-23.

Rusconi L, Salvatoni L, Giudici L, Bertani I, Kilstrup-Nielsen C, Broccoli V, et al. CDKL5 expression is modulated during neuronal development and its subcellular distribution is tightly regulated by the C-terminal tail. J Biol Chem 2008; 283(44): 30101-11.

Russo FB, Freitas BC, Pignatari GC, Fernandes IR, Sebat J, Muotri AR, et al. Modeling the Interplay Between Neurons and Astrocytes in Autism Using Human Induced Pluripotent Stem Cells. Biol Psychiatry 2018; 83(7): 569-78.

Sah D, Mazzarelli A, Christensen E, Thompson J, Lindgren H, Felix-Ortiz A, et al. Safety and increased transduction efficiency in the adult nonhuman primate central nervous system with intravenous delivery of two novel adeno-associated virus capsids [Abstract O661]. American Society of Gene and Cell Therapy Annual Meeting. Chicago, USA. Mol Ther 2018; 26 (Suppl 1): S305.

Scholz J, Niibori Y, W Frankland P, P Lerch J. Rotarod training in mice is associated with changes in brain structure observable with multimodal MRI. Neuroimage 2015; 107: 182-9.

Sekiguchi M, Katayama S, Hatano N, Shigeri Y, Sueyoshi N, Kameshita I. Identification of amphiphysin 1 as an endogenous substrate for CDKL5, a protein kinase associated with X-linked neurodevelopmental disorder. Arch Biochem Biophys 2013; 535(2): 257-67.

Sivilia S, Mangano C, Beggiato S, Giuliani A, Torricella R, Baldassarro VA, et al. CDKL5 knockout leads to altered inhibitory transmission in the cerebellum of adult mice. Genes Brain Behav 2016; 15(5): 491-502.

Suárez J, Bermúdez-Silva FJ, Mackie K, Ledent C, Zimmer A, Cravatt BF, et al. Immunohistochemical description of the endogenous cannabinoid system in the rat cerebellum and functionally related nuclei. J Comp Neurol 2008; 509(4): 400-21.

Szafranski P, Golla S, Jin W, Fang P, Hixson P, Matalon R, et al. Neurodevelopmental and neurobehavioral characteristics in males and females with CDKL5 duplications. Eur J Hum Genet 2015; 23(7): 915-21.

Tang S, Wang IJ, Yue C, Takano H, Terzic B, Pance K, et al. Loss of CDKL5 in Glutamatergic Neurons Disrupts Hippocampal Microcircuitry and Leads to Memory Impairment in Mice. J Neurosci 2017; 37(31): 7420-37.

Thorson L, Bryke C, Rice G, Artzer A, Schilz C, Israel J, et al. Clinical and molecular characterization of overlapping interstitial Xp21-p22 duplications in two unrelated individuals. Am J Med Genet A 2010; 152A(4): 904-15.

Trazzi S, De Franceschi M, Fuchs C, Bastianini S, Viggiano R, Lupori L, et al. CDKL5 protein substitution therapy rescues neurological phenotypes of a mouse model of CDKL5 disorder. Hum Mol Genet 2018; 27(9): 1572-92.

Trazzi S, Fuchs C, Viggiano R, De Franceschi M, Valli E, Jedynak P, et al. HDAC4: a key factor underlying brain developmental alterations in CDKL5 disorder. Hum Mol Genet 2016; 25(18): 3887-907.

Tzschach A, Chen W, Erdogan F, Hoeller A, Ropers HH, Castellan C, et al. Characterization of interstitial Xp duplications in two families by tiling path array CGH. Am J Med Genet A 2008; 146A(2): 197-203.

Van Esch H, Jansen A, Bauters M, Froyen G, Fryns JP. Encephalopathy and bilateral cataract in a boy with an interstitial deletion of Xp22 comprising the CDKL5 and NHS genes. Am J Med Genet A 2007; 143(4): 364-9.

Wang IT, Allen M, Goffin D, Zhu X, Fairless AH, Brodkin ES, et al. Loss of CDKL5 disrupts kinome profile and event-related potentials leading to autistic-like phenotypes in mice. Proc Natl Acad Sci U S A 2012; 109(52): 21516-21.

White JJ, Sillitoe RV. Development of the cerebellum: from gene expression patterns to circuit maps. Wiley Interdiscip Rev Dev Biol 2013; 2(1): 149-64.

Williamson SL, Giudici L, Kilstrup-Nielsen C, Gold W, Pelka GJ, Tam PP, et al. A novel transcript of cyclin-dependent kinase-like 5 (CDKL5) has an alternative C-terminus and is the predominant transcript in brain. Hum Genet 2012; 131(2): 187-200.

Xiong J, Chen S, Pang N, Deng X, Yang L, He F, et al. Neurological Diseases With Autism Spectrum Disorder: Role of ASD Risk Genes. Front Neurosci 2019; 13: 349.

Zhou A, Han S, Zhou ZJ. Molecular and genetic insights into an infantile epileptic encephalopathy - CDKL5 disorder. Front Biol (Beijing) 2017; 12(1): 1-6.

Zhu YC, Li D, Wang L, Lu B, Zheng J, Zhao SL, et al. Palmitoylation-dependent CDKL5-PSD-95 interaction regulates synaptic targeting of CDKL5 and dendritic spine development. Proc Natl Acad Sci U S A 2013; 110(22): 9118-23.

Zolotukhin S, Byrne BJ, Mason E, Zolotukhin I, Potter M, Chesnut K, et al. Recombinant adeno-associated virus purification using novel methods improves infectious titer and yield. Gene Ther 1999; 6(6): 973-85.

Figure legends

Figure 1. Identification and molecular cloning of *hCDKL5* brain isoforms.

A Schematic showing the structure of *hCDKL5* gene and positions of *CDKL5* primers (Supplementary Table 1). The dotted lines within exons represent alternative splice sites. The introns and 3'-untranslated regions (UTR) of exon 19 were not drawn to scale.

B Identification of *hCDKL5* isoforms in human brain cerebral cortex, testis, neuronal cell lines and glia via RACE and RT-PCR. Electrophoretic gels were cropped to show bands under investigation only and full-length gels can be seen in Supplementary Fig 1. RACE and RT-PCR were conducted using 3'-CDS *hCDKL5_1* primer to amplify *hCDKL5_1* and/or *hCDKL5_2* isoforms (top panels) or using 3'-CDS *hCDKL5_5* primer to amplify *hCDKL5_5* isoform (bottom panels). NC: negative control. NTC: non-template control.

Cerebral cortex: the *hCDKL5_1* (634 bp product) and *hCDKL5_2* (757 bp product) isoforms (top panels) were identified by RACE PCR using Human Cerebral Cortex Poly A+ RNA, whilst the *hCDKL5_5* (915 bp product) isoform was not detected (bottom panels) (full-length gels: Supplementary Fig 1 C). ~~Lanes 1 and 4: 634 bp product from *hCDKL5_1* and 757 bp from *hCDKL5_2* (top panel), no *hCDKL5_5* product (bottom panel). Lane 2:~~ NC 1: reverse primer (UPM: Universal Primer A Mix, Takara bio) only negative control. NC 2: forward primer (GSP2) only negative control.

Testis: the *hCDKL5_1* (634 bp product) (top panel) and *hCDKL5_5* (915 bp product) (bottom panel) isoforms were identified by RT-PCR using Human Testis Total RNA (Takara Bio) as positive control, based on the previous data on *hCDKL5_1* and *hCDKL5_5* isoforms in human testis (Williamson *et al.*, 2012; Hector *et al.*, 2016) (full-length gel: Supplementary Fig 1 D). ~~Lane 1: 634 bp product from *hCDKL5_1* (top panel) and 915 bp product from *hCDKL5_5* (bottom panel). Lane 2: non-template control of Lane 1 reactions.~~

Neuronal cell lines: the *hCDKL5_1* (634 bp product) and *hCDKL5_2* (757 bp product) isoforms were identified by RT-PCR using total RNA extracted from each neuronal cell line, whilst the *hCDKL5_5* (915 bp product) isoform was not detected.

Neuroblastoma cell lines (full-length gel: Supplementary Fig 1 E): ~~Lanes 1-2:~~ undifferentiated SH-SY5Y cells (left panels), ~~Lane 1:~~ 634 bp product from *hCDKL5_1* and 757 bp from *hCDKL5_2* (top panel) but no *hCDKL5_5* product (bottom panel); ~~Lane 2: non-template~~

~~control of Lane 1 reaction. Lanes 3-4:~~ differentiated SH-SY5Y cells (right panels), ~~Lane 3:~~ 634 bp product from *hCDKL5_1* and 757 bp from *hCDKL5_2* (top panel) but no *hCDKL5_5* product (bottom panel). ~~Lane 4: non-template control of Lane 3 reaction.~~

hESC-derived interneurons: ~~Lanes 5-6:~~ unsorted hESC-derived *NKX2.1*-GFP^{+} cortical interneurons (left panel) (full-length gel: Supplementary Fig 1 F), 634 bp product from *hCDKL5_1* and 757 bp from *hCDKL5_2*. hESC-derived culture without FACS-sorting was a mixture of *NKX2.1*-GFP^{+} interneurons and GFP^{-} cells. ~~Lane 5: Lane 6: non-template control of Lane 5 reaction. Lanes 7-8:~~ FACS-sorted hESC-derived *NKX2.1*-GFP^{+} cortical interneurons (right panel) (full-length gel: Supplementary Fig 1 G), 634 bp product from *hCDKL5_1*. *NKX2.1*-GFP^{+} interneurons were selected from hESC-derived culture via FACS-sorting. ~~Lane 7: Lane 8: non-template control of Lane 7 reaction.~~

Glia: the *hCDKL5_1* (634 bp product) and *hCDKL5_2* (757 bp product) isoforms (top panel) were identified by RT-PCR using total RNA extracted from primary human astrocytes, whilst the *hCDKL5_5* (915 bp product) isoform was not detected (bottom panel) (full-length gel: Supplementary Fig 1 H). ~~Lane 1: 634 bp product from *hCDKL5_1* and 757 bp from *hCDKL5_2* (top panel) but no *hCDKL5_5* product (bottom panel). Lane 2: non-template control of Lane 1 reaction.~~

C Schematics showing the exon composition of 3 coding isoforms identified, *hCDKL5_1*, *hCDKL5_2* and *hCDKL5_5*. *hCDKL5_2* has the same exon composition as *hCDKL5_1*, but contains one extra exon, exon 17 (green), a highly conserved brain-specific exon (Fichou *et al.*, 2011; Hector *et al.*, 2016). *hCDKL5_5* differs from the other isoforms at the 3' end, with an alternative splice site in exon 19 (blue) and exons 20 to 22 (purple) (Hector *et al.*, 2016). The introns and 3'-UTR of exon 19 were not drawn to scale.

D WB of CDKL5 expression in different human cell lines. Blots were cropped to show bands under investigation only and full-length blots can be seen in Supplementary Fig 2 A. ~~Lane 1: Differentiated SH-SY5Y cells. Lane 2: Undifferentiated SH-SY5Y cells. Lane 3: HEK 293T cells. Lane 4: HEK 293 cells. Lane 5:~~ HeLa cells: positive control according to the datasheet of mouse anti-CDKL5 monoclonal antibody used (Santa Cruz). ~~Lane 6: Primary human astrocytes. Lane 7: HES-3 *NKX2.1*$^{GFP/w}$ hESCs. Lane 8:~~ Cell lysis buffer (RIPA Lysis and Extraction Buffer, Thermo Scientific): no cell lysate, negative control. GAPDH: loading control. 8.7 µg total protein was loaded for each cell line.

E Schematics depicting transgene cassettes cloned into the ssAAV vector genome. Expression of HA-tagged *hCDKL5_1*, Myc-tagged *hCDKL5_2* and eGFP were driven by a CBh promoter. ITR: inverted terminal repeat. CBh: a hybrid form of CBA promoter. pA: bovine growth hormone (BGH) polyA.

F WB of transgene expression in HEK 293T cells transfected with AAV vector plasmids. Blots were cropped to show bands under investigation only and full-length blots can be seen in Supplementary Fig 2 B-C. 10 μg total protein was loaded for each sample. GFP: positive control. Untransfected 293T cells: negative control. GAPDH: loading control.

Figure 2. AAV-PHP.B efficiently transduces CNS and peripheral tissues following intrajugular injection into adult WT male mice.

A-E ssAAV9-CBh-eGFP or ssAAV-PHP.B-CBh-eGFP, at 1×10^{12} vg per animal, was intrajugularly injected into WT male mice at age 43-51 days, using saline as negative control. Images show GFP expression 4 weeks after injection.

A Representative sagittal brain sections with GFP (green) immunostaining of mice given saline (left), AAV9 (middle) or AAV-PHP.B (right).

B AAV-PHP.B transduced both neurons and astrocytes in various mouse brain regions. Representative images show that GFP^+ (green) cells colocalise with $NeuN^+$ (red) neurons and $GFAP^+$ (red) astrocytes in cortex, hippocampus and striatum (left and middle); $NeuN^+$ neurons in thalamus, Purkinje cells in cerebellum, and TH^+ (red) neurons in substantia nigra (right). Cell nuclei were counterstained with DAPI (blue). Scale bars: 50 μm.

C AAV-PHP.B transduced mouse spinal cords and DRGs. Representative images show spinal cord (left) and DRGs (right) with GFP (green) immunostaining of mice treated with AAV-PHP.B (top) or saline (bottom). Cell nuclei were counterstained with DAPI (blue). Scale bars: 100 μm.

D AAV-PHP.B transduced mouse retina. Representative images show retina with GFP (green) immunostaining of mice treated with AAV-PHP.B (top) or saline (bottom). Cell nuclei were counterstained with DAPI (blue). Scale bars: 50 μm.

E AAV-PHP.B transduced mouse kidney. Representative images show renal cortex (left) and medulla (right) with GFP (green) immunostaining of mice treated with AAV-PHP.B (top) or saline (bottom). Cell nuclei were counterstained with DAPI (blue). Scale bars: 50 μm.

F Quantitative analysis of AAV biodistribution in mouse brain. Data are presented as mean ± SEM. No mannitol group: saline, n = 2; AAV9, n = 3; AAV-PHP.B, n = 3. Mannitol group: saline, n = 4; AAV9, n = 5; AAV-PHP.B, n = 2. Two-way ANOVA with Sidak's multiple comparisons test.

G Quantification of the percentage of GFP^+ cells among $NeuN^+$ neurons in different brain regions of AAV-PHP.B-injected mice. Data are presented as mean ± SEM. n = 3 per group.

H Quantitative analysis of relative GFP fluorescence intensity of DRG neurons in AAV-PHP.B-injected mice relative to autofluorescence in saline-injected mice. Data are presented as mean ± SEM. Small diameter DRG neurons (<25 μm): AAV-PHP.B, n = 11 cells from 3 mice; saline, n = 38 cells from 2 mice. Intermediate diameter DRG neurons (25-40 μm): AAV-PHP.B, n = 16 cells from 3 mice; saline, n = 23 cells from 2 mice. Large diameter DRG neurons (>40 μm): AAV-PHP.B, n = 13 cells from 3 mice; saline, n = 26 cells from 2 mice. Multiple t-tests; ****P<0.0001.

Figure 3. Behavioural characterization of adult *Cdkl5* KO male mice.

A Open field test demonstrating hyperactivity in *Cdkl5* KO mice. *Cdkl5*$^{-/y}$ mice exhibited significantly increased activity relative to *Cdkl5*$^{+/y}$ mice (3-5 months). n = 10 per group.

B Rotarod test demonstrating impaired motor coordination in *Cdkl5* KO mice. *Cdkl5*$^{-/y}$ mice exhibited significantly decreased latency to fall from accelerating rotating rod to *Cdkl5*$^{+/y}$ mice (3-5 months). n = 10 per group.

C Hind-limb clasping test demonstrating abnormal clasping in *Cdkl5* KO mice. *Cdkl5*$^{-/y}$ mice exhibited significantly higher clasping score than *Cdkl5*$^{+/y}$ mice (3-5 months). n = 10 per group.

D Marble burying test demonstrating decreased repetitive behaviour in *Cdkl5* KO mice. *Cdkl5*$^{-/y}$ mice buried significantly fewer marbles than *Cdkl5*$^{+/y}$ mice (3-5 months). n = 10 per group.

E Nesting test demonstrating impaired nesting behaviour in *Cdkl5* KO mice. *Cdkl5*$^{-/y}$ mice exhibited significantly lower nesting score and more Nestlet left after the nesting test relative to *Cdkl5*$^{+/y}$ mice (5-7 months). n = 9 per group.

F Social interaction test demonstrating impaired social interaction in *Cdkl5* KO mice. *Cdkl5*$^{-/y}$ mice exhibited a significant reduction in percentage of time spent interacting in 5 minutes and a trend of reduction in 10 minutes relative to *Cdkl5*$^{+/y}$ mice (4-6 months). n = 5 per group.

G Three-chambered social approach test demonstrating normal sociability but impaired social novelty in *Cdkl5* KO mice. *Cdkl5*$^{-/y}$ mice (n = 7) exhibited normal social approach but impaired social novelty relative to *Cdkl5*$^{+/y}$ mice (n = 6) (4-6 months).

H Elevated O-maze test demonstrating normal anxiety in *Cdkl5* KO mice. *Cdkl5*$^{-/y}$ mice exhibited similar percentage of time spent in open area relative to *Cdkl5*$^{+/y}$ mice (3-5 months). n = 10 per group.

I Y-maze test demonstrating impaired spontaneous alteration in *Cdkl5* KO mice. *Cdkl5*$^{-/y}$ mice exhibited a trend of decreased percentage of spontaneous alterations whilst increased percentage of alternative arm entries relative to *Cdkl5*$^{+/y}$ mice (3-5 months). n = 10 per group.

J Contextual fear conditioning test demonstrating impaired contextual fear memory in *Cdkl5* KO mice. *Cdkl5*$^{-/y}$ mice exhibited significantly lower percentage of freezing whilst higher activity relative to *Cdkl5*$^{+/y}$ mice (4-6 months) when placed back into the same testing box without shock or tone. n = 10 per group.

K Cued fear conditioning test demonstrating impaired cued fear memory in *Cdkl5* KO mice. When placed into a novel testing box (Pre-CS), *Cdkl5*$^{-/y}$ mice exhibited similar percentage of freezing and activity to *Cdkl5*$^{+/y}$ mice. After given the same cued tone (90 dB, 10 kHz) (CS), *Cdkl5*$^{-/y}$ mice showed significantly lower percentage of freezing and activity relative to *Cdkl5*$^{+/y}$ mice (4-6 months). n = 10 per group. CS: conditioned stimulus.

Data are presented as mean ± SEM. **P*<0.05, ***P*<0.01, ****P*<0.001, *****P*<0.0001; unpaired t-test (A-F, H-J), and two-way ANOVA with Bonferroni's multiple comparisons test (E, K) or Tukey's multiple comparisons test (G) or Sidak's multiple comparisons test (K).

Figure 4. Behavioural improvements in *Cdkl5* KO male mice treated with AAV-PHP.B-*hCDKL5_1*.

AAV-PHP.B-HA-*hCDKL5_1* or AAV-PHP.B-eGFP, at 1 × 10^{12} vg per animal, was intrajugularly injected into *Cdkl5*$^{-/y}$ mice at age 28-30 days. Behavioural tests were conducted during 1-3 months after AAV injection and saline-injected WT littermates were used as positive control.

A Hind-limb clasping test showed improved hind-limb clasping in hCDKL5_1-treated *Cdkl5* KO mice relative to GFP-treated ones. Clasping score of hCDKL5_1-treated *Cdkl5*$^{-/y}$ mice was significantly decreased compared to the GFP-treated ones.

B Marble burying test showed partially restored repetitive behaviour in hCDKL5_1-treated *Cdkl5* KO mice relative to GFP-treated ones. hCDKL5_1-treated *Cdkl5*$^{-/y}$ mice buried significantly more marbles in total than the GFP-treated ones.

C Rotarod test showed restored motor coordination in hCDKL5_1-treated *Cdkl5* KO mice relative to GFP-treated ones. hCDKL5_1-treated *Cdkl5*$^{-/y}$ mice revealed significantly higher latency to fall than the GFP-treated ones.

D Contextual fear conditioning test showed a modest improvement in contextual fear memory in hCDKL5_1-treated *Cdkl5* KO mice relative to GFP-treated ones. hCDKL5_1-treated *Cdkl5*$^{-/y}$ mice showed no significant improvement in percentage of time freezing compared to the GFP-treated ones.

E Open field test showed a tendency for increased hyperactivity in hCDKL5_1-treated *Cdkl5* KO mice relative to GFP-treated ones. hCDKL5_1-treated *Cdkl5*$^{-/y}$ mice were more hyperactive than the GFP-treated ones, which were themselves more hyperactive than *Cdkl5*$^{+/y}$ mice.

Data are presented as mean ± SEM. n = 10 per group for all tests except for n = 9 of the hCDKL5_1-treated *Cdkl5*$^{-/y}$ mice group in the open field test. **P*<0.05, ***P*<0.01, ****P*<0.001, *****P*<0.0001; unpaired t-test (C), ordinary one-way ANOVA (A, B), and two-way ANOVA with Tukey's multiple comparisons test (C, E).

Figure 5. Restored CDKL5 expression in the hindbrain of hCDKL5_1-treated *Cdkl5* KO mice.

A WB analysis of CDKL5 expression in hindbrain. Blots were cropped to show bands under investigation only and full-length blots can be seen in Supplementary Fig 6 A. *Cdkl5*$^{+/y}$ + saline [a]: sample processing control of 2 blots. GAPDH: loading control. 34 µg total protein was loaded for each cell line.

B Quantitative analysis of CDKL5 expression normalised to GAPDH in hindbrain. The samples on the 2 blots were derived from the same experiment and blots were processed in parallel, using the same *Cdkl5*$^{+/y}$ + saline [a] sample loaded on each blot as the sample processing control. Data are presented as mean ± SEM. Saline-treated *Cdkl5*$^{+/y}$ mice: n = 3; hCDKL5_1-treated *Cdkl5*$^{-/y}$ mice: n = 5; GFP-treated *Cdkl5*$^{-/y}$ mice: n = 5; saline-treated *Cdkl5*$^{-/y}$ mice: n = 2. One-way ANOVA with Tukey's multiple comparisons test; **P*<0.05, ***P*<0.01.

Figure 6. Correction of PSD95 misexpression in the anterior domain of cerebellar vermis in hCDKL5_1-treated *Cdkl5* KO mice.

A Regions a – e and 4 transverse domains in cerebellum. Region a: lobules I – III; region b: lobules IV – V; region c: lobules VIa, VIb and VII; region d: lobules VIII – IX; region e: lobule X.

B Representative images show HA^+ (green) Purkinje cells in cerebellar regions a – e. Cell nuclei were counterstained with DAPI (blue). Scale bars: 25 μm.

C Quantitative analysis of relative HA fluorescence intensity of Purkinje cells in cerebellar regions a – e. region a: n = 75 cells from 5 mice; region b: n = 61 cells from 5 mice; region c: n = 84 cells from 5 mice; region d: n = 63 cells from 5 mice; region e: n = 50 cells from 5 mice. Data are presented as min to max. Two-way ANOVA with Tukey's multiple comparisons test; $^{**}P<0.01$, $^{****}P<0.0001$.

D Representative images of CB^+ (green) Purkinje cells and $PSD95^+$ (red) pinceau in the anterior domain of cerebellar vermis in *Cdkl5*$^{-/y}$ mice injected with AAV-PHP.B-*hCDKL5_1* (bottom) relative to those with AAV-PHP.B-eGFP (top). Scale bars: 25 μm.

E Quantitative analysis of $PSD95^+$ pinceau volume in the anterior domain of cerebellar vermis showed the abnormally increased pinceau volume in *Cdkl5*$^{-/y}$ mice was restored by hCDKL5_1 expression. hCDKL5_1-treated *Cdkl5*$^{-/y}$ mice exhibited a significant reduction in $PSD95^+$ pinceau volume in the anterior cerebellar vermis relative to GFP-treated ones. *Cdkl5*$^{-/y}$ + GFP: n = 164 pinceau from 5 mice; *Cdkl5*$^{-/y}$ + hCDKL5_1: n = 209 pinceau from 5 mice. Data are presented as min to max. Ordinary two-way ANOVA; $^{**}P<0.01$.

Box-and-whisker plots in C and E, from top to bottom: Maximum, Upper quartile, Median, Lower quartile and minimum.

Figure 7. Amelioration of deficits in *CDKL5*-mutant iPSC-derived neurons treated with AAV-DJ-*hCDKL5_1/2*.

A-D Comparison of $VGLUT1^+$ puncta density and calcium signalling between #13 *CDKL5*-mutant iPSC-derived neurons and #11 isogenic control.

A-B TUJ1/VGLUT1 dual staining of #11 and #13 iPSC-derived neurons. #11 (A) and #13 (B) neurons were co-labelled with TUJ1 (green) and VGLUT1 (red). Cell nuclei were counterstained with DAPI (blue). Scale bars: 25 µm.

C Quantification of VGLUT1$^+$ puncta density on the secondary dendrites of non-transduced #11 and #13 iPSC-derived neurons. #13 neurons exhibited a slight trend of decreased VGLUT1$^+$ puncta density on the secondary dendrites relative to #11 neurons, although this was not statistically significant. Data are presented as mean ± SEM. #11 neurons: n = 31 secondary dendrites from 5 neurons; #13 neurons: n = 24 secondary dendrites from 5 neurons. Unpaired t-test.

D Transient cytosolic Ca^{2+} changes induced by bath application of 50 mM KCl in fluo-4-loaded #11 and #13 iPSC-derived neurons. Intracellular Ca^{2+} changes are presented as ratios of the fluorescence change and basal fluorescence ($\Delta F/F_0$). #13 neurons exhibited a sharp decrease after the peak relative to the steadily decreasing curve of #11 neurons, indicating the functional defects of *CDKL5*-mutant neurons in maintaining high concentration of cytosolic Ca^{2+} and recovering to basal state. n = 50 neurons per group. Data are presented as mean only for the comparison purpose. Data presented as mean ± SEM can be seen in Supplementary Fig 9.

E-I Improvement of VGLUT1$^+$ puncta density by hCDKL5_1 expression and amelioration of calcium signalling defect by hCDKL5_2 expression in #13 *CDKL5*-mutant iPSC-derived neurons.

E-G Dual staining of #13 iPSC-derived neurons transduced by AAV-DJ vectors. #13 neurons transduced by AAV-DJ-eGFP were labelled with GFP (green) (E); those transduced by AAV-DJ- HA-*hCDKL5_1* were labelled with HA (green) (F); and those transduced by AAV-DJ-Myc-*hCDKL5_2* were labelled with Myc (green) (G). All #13 neurons were co-labelled with VGLUT1 (red). Scale bar: 25 µm.

H Quantification of VGLUT1 puncta density on the secondary dendrites of #13 neurons transduced by AAV-DJ vectors. *hCDKL5_1* expression significantly increased synaptic density of VGLUT1$^+$ puncta along the secondary dendrites, whilst *hCDKL5_2* enhanced the VGLUT1$^+$ puncta density but not in a statistically significant manner relative to GFP. Data are presented as mean ± SEM. GFP: n = 12 secondary dendrites from 5 neurons; *hCDKL5_1*: n = 27 secondary dendrites from 5 neurons; *hCDKL5_2*: n = 13 secondary dendrites from 5 neurons. Unpaired t-test.

I Transient cytosolic Ca^{2+} changes induced by bath application of 50 mM KCl in fluo-4-loaded #13 neurons transduced with AAV-DJ-eGFP (n = 30), AAV-DJ-HA-*hCDKL5_1* (n = 30) or AAV-DJ-Myc-*hCDKL5_2* vectors (n = 26). Intracellular Ca^{2+} changes are presented as ratios of the fluorescence change and basal fluorescence ($\Delta F/F_0$). #13 neurons expressing hCDKL5_2 exhibited a $\Delta F/F_0$ curve similar to #11 neurons, with a steadily decreasing curve after the peak relative to the sharp decrease of GFP control. #13 neurons expressing hCDKL5_1 showed a small increase of $\Delta F/F_0$ for less than 10%, but a similar polarization rate to those expressing hCDKL5_2. Data are presented as mean only for the comparison purpose. Data presented as mean ± SEM can be seen in Supplementary Fig 9.

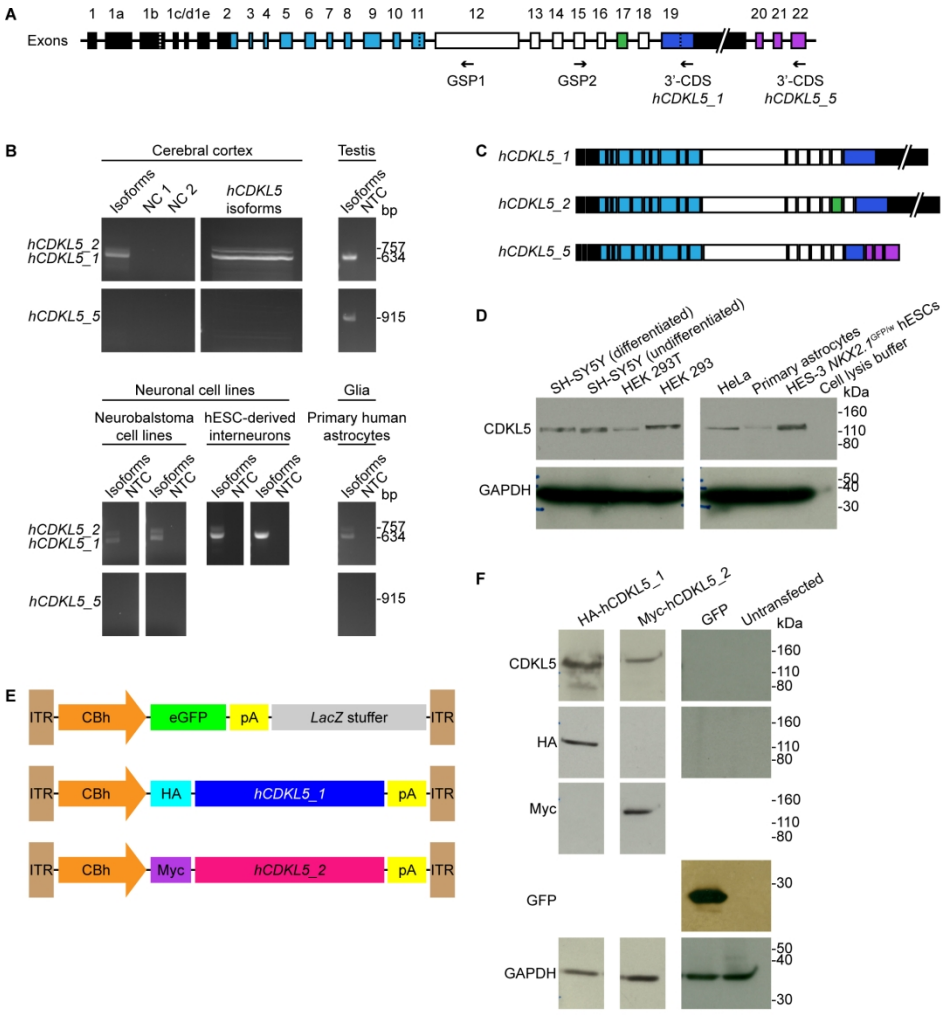

Figure 1

Figure 1. Identification and molecular cloning of *hCDKL5* brain isoforms

180x230mm (300 x 300 DPI)

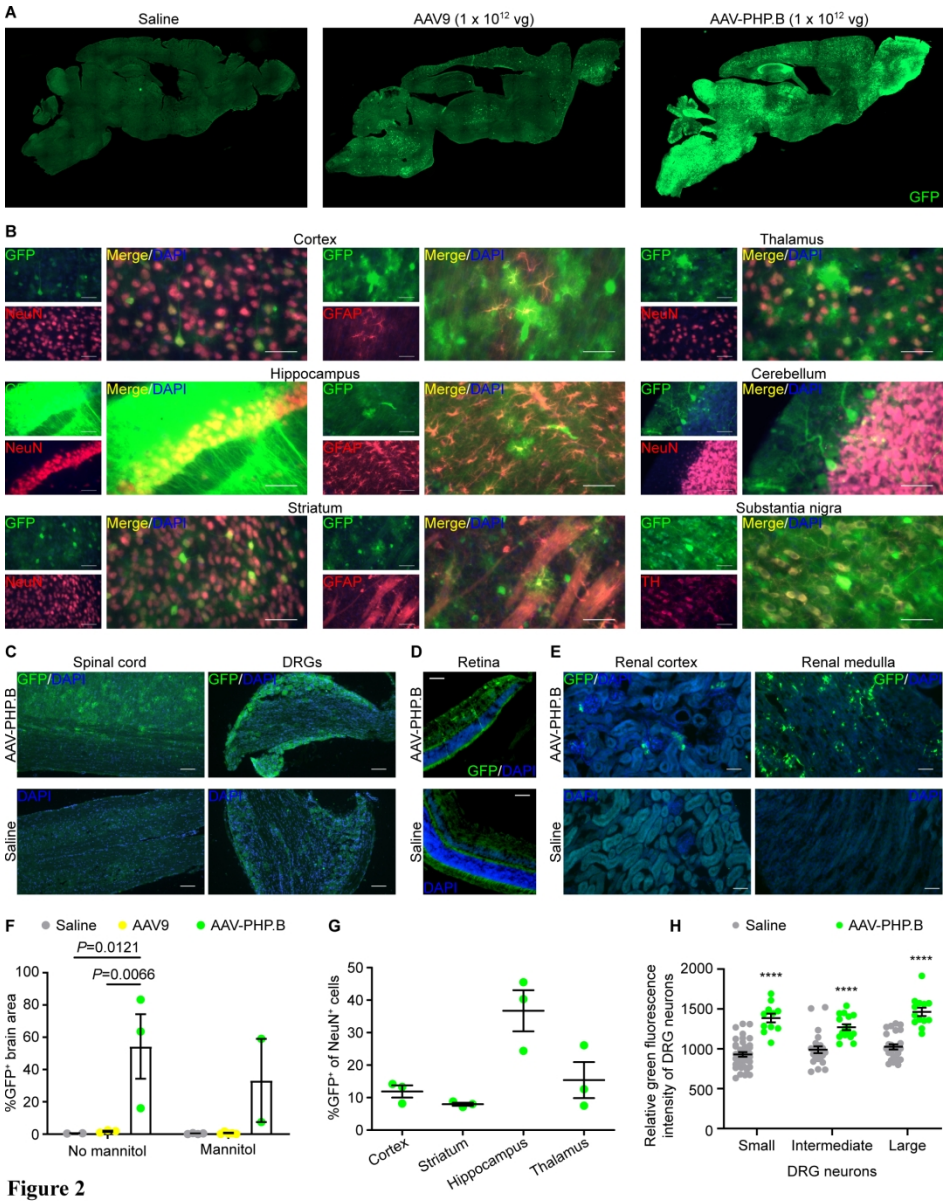

Figure 2

Figure 2. AAV-PHP.B efficiently transduces CNS and peripheral tissues following intrajugular injection into adult WT male mice

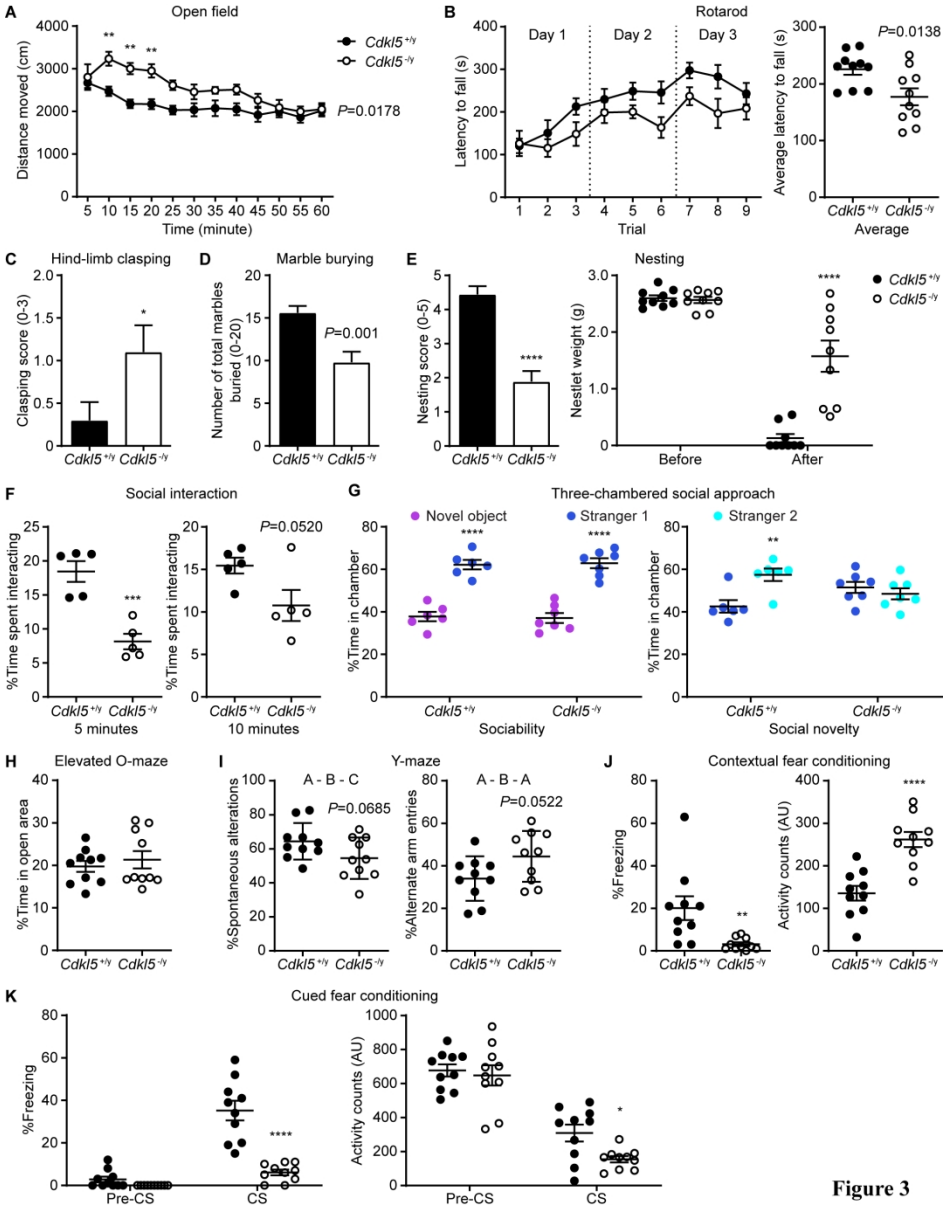

Figure 3. Behavioural characterization of adult *Cdkl5* KO male mice

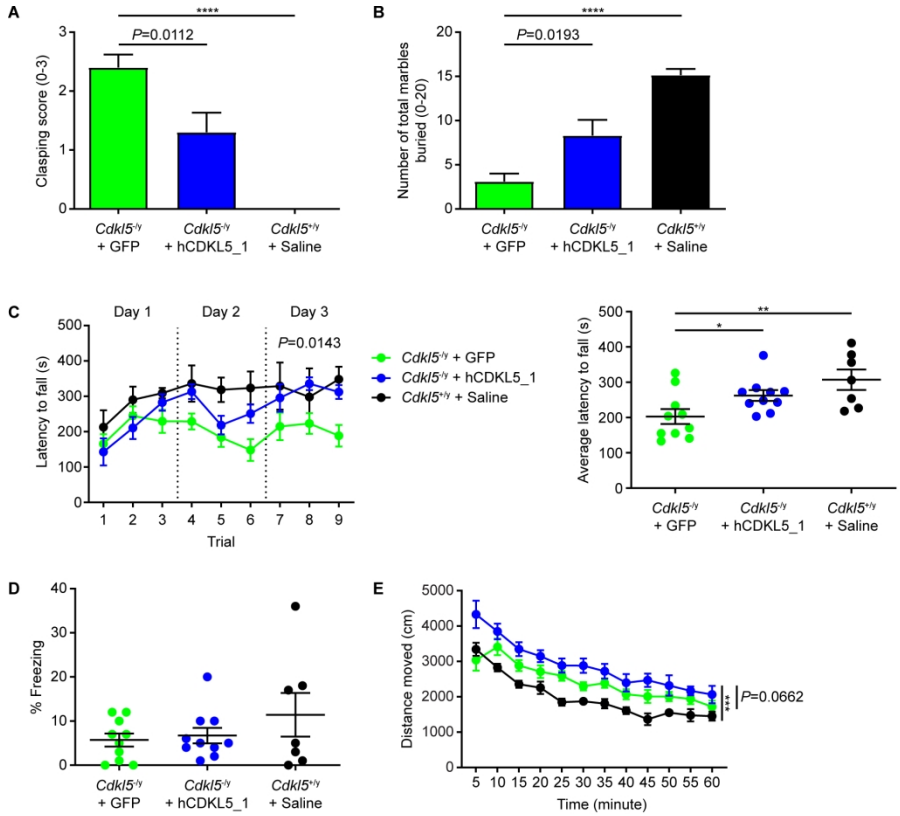

Figure 4

Figure 4. Behavioural improvements in *Cdkl5* KO male mice treated with AAV-PHP.B-*hCDKL5_1</i*

180x230mm (300 x 300 DPI)

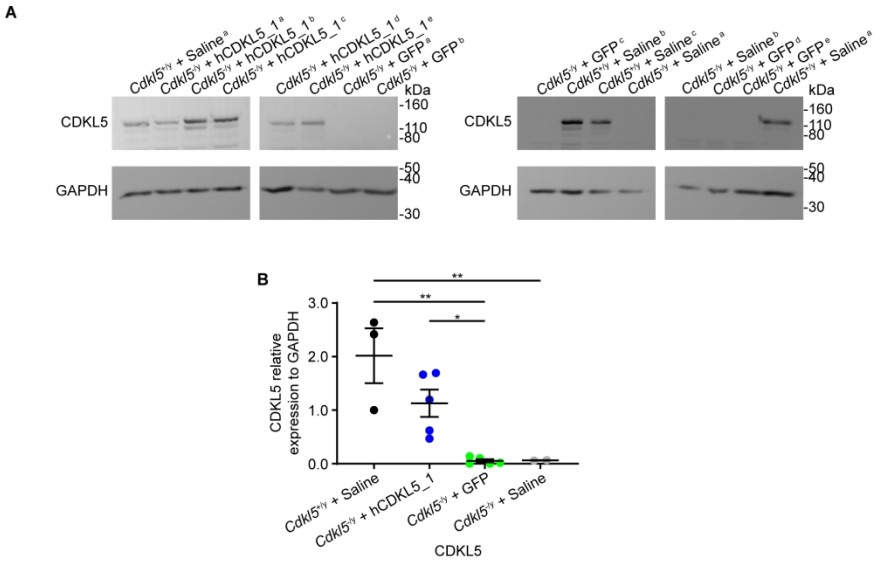

Figure 5

Figure 5. Restored CDKL5 expression in the hindbrain of hCDKL5_1-treated *Cdkl5* KO mice

180x230mm (300 x 300 DPI)

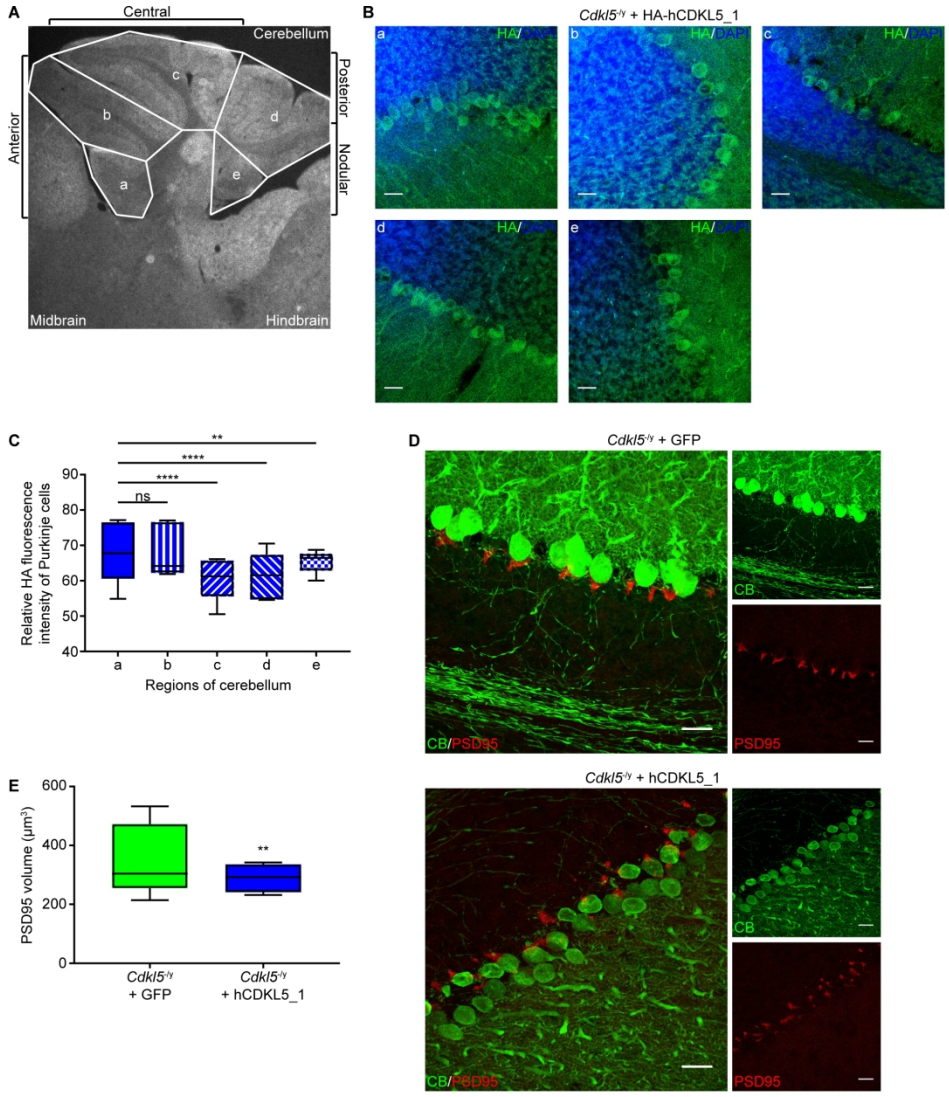

Figure 6

Figure 6. Correction of PSD95 misexpression in the anterior domain of cerebellar vermis in hCDKL5_1-treated *Cdkl5* KO mice.

180x230mm (300 x 300 DPI)

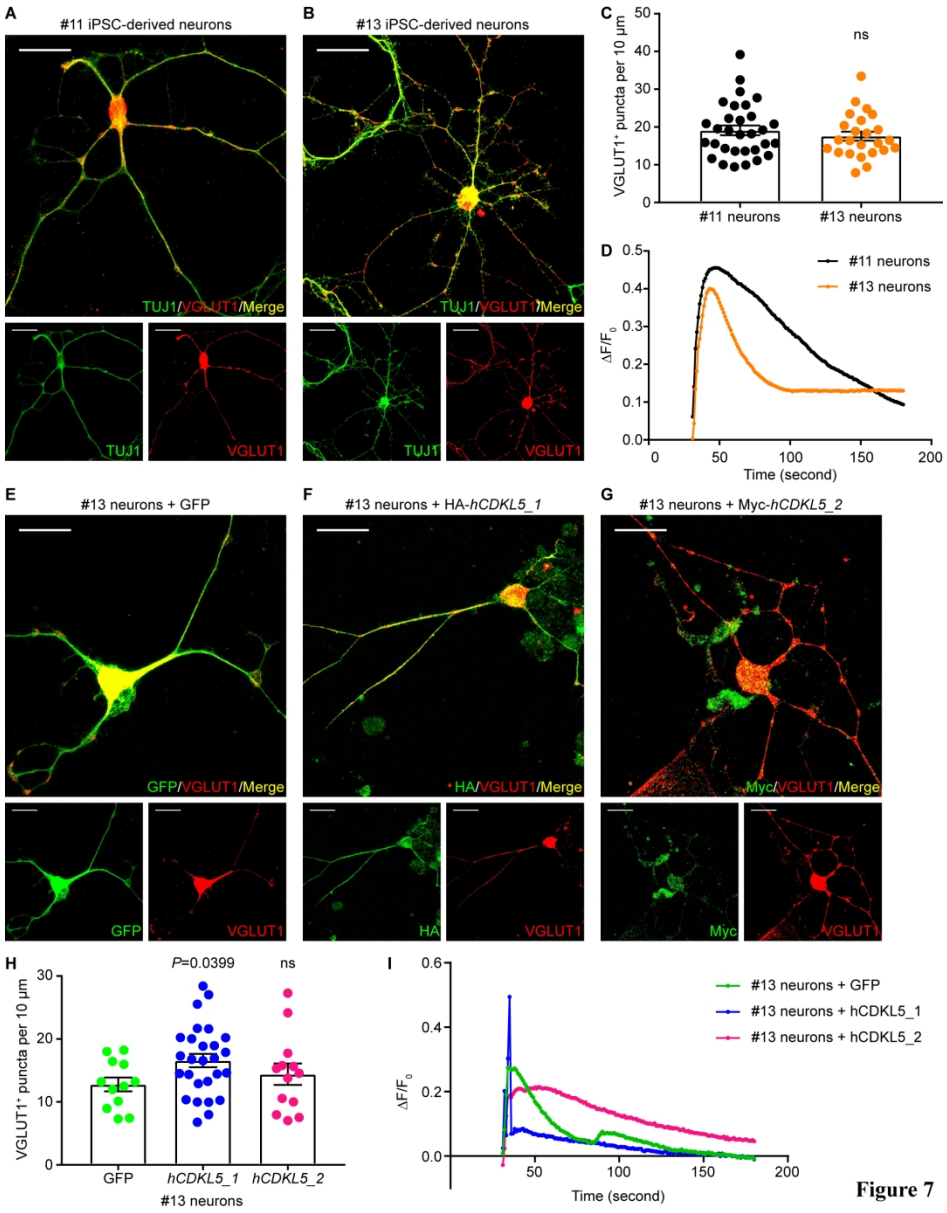

Figure 7. Amelioration of deficits in *CDKL5*-mutant iPSC-derived neurons treated with AAV-DJ-*hCDKL5_1/2*

Supplementary Materials

Supplementary Methods

Cell lines, culture and differentiation

All cell lines were incubated at 37°C in humid, 5% CO_2 HERAcell® 150 and 150i Incubators (Thermo) and handled under sterile conditions in the Biological Safety Cabinets Class II (NuAire or LaboGene). HEK 293 cells were culture in Minimum Essential Medium Eagle (EMEM) (Sigma) supplemented with 10% Fetal Bovine Serum (FBS) (Gibco), 2 mM L-Glutamine (200 mM) (Sigma), 1x Non-Essential Amino Acids (NEAA, 100×) (Gibco) and 1x Penicillin/Streptomycin (100x) (Sigma). HEK 293T cells were cultured in Dulbecco's Modified Eagle's Medium (DMEM) (Sigma) supplemented with 10% FBS, 2 mM L-Glutamine and 1x Penicillin/Streptomycin. HeLa cells were cultured in EMEM supplemented with 10% FBS, 2 mM L-Glutamine, 1x NEAA and 1x Penicillin/Streptomycin. Primary human astrocytes were cultured in ABM™ Astrocyte Basal Medium (Lonza) supplemented with AGM™ SingleQuots™ (Lonza) according to manufacturer's instructions. SH-SY5Y cells were maintained in Ham's F-12 (Sigma): EMEM (1:1) supplemented with 15% FBS, 2 mM L-Glutamine, 1x NEAA and 1x Penicillin/Streptomycin. SNL cells were cultured in DMEM supplemented with 10% FBS, 2 mM L-Glutamine, 1x Penicillin/Streptomycin, 1x 2-Mercaptoethanol (2-ME) (55 mM, 1000x) (Gibco) and 200 µg/ml Geneticin™ Selective Antibiotic (Gibco). To make feeders, confluent SNL cells were incubated with DMEM supplemented with 10% FBS, 2 mM L-Glutamine, 1x Penicillin/Streptomycin, 1x 2-ME and 10 µg/ml Mitomycin C (Sigma) for 2-3 hours at 37°C and then split 1:2 into 0.1% gelatin-coated flasks. HES-3 *NKX2.1*$^{GFP/w}$ hESCs were maintained on SNL-derived feeders in DMEM/F-12 (Gibco) supplemented with 20% KnockOut™ Serum Replacement (Gibco), 1x GlutaMAX™ Supplement (100x) (Gibco), 1x NEAA, 1x Penicillin/Streptomycin, 1x 2-ME and freshly added 10 ng/ml FGF2 (R&D). RET849 #11 and #13 iPSCs were maintained in mTeSR™1 Basal Medium (Stemcell) supplemented with 1x mTeSR™1 Supplement (5x) (Stemcell) and 1x Penicillin/Streptomycin.

SH-SY5Y cells were differentiated in Ham's F-12: EMEM (1:1) supplemented with 15% FBS, 2 mM L-Glutamine, 1x NEAA, 1x Penicillin/Streptomycin and 10 µM all trans-retinoic acid for 7 days.

HES-3 *NKX2.1*$^{GFP/w}$ hESCs were differentiated into *NKX2.1*-GFP^{+} cortical interneurons using the B27 + 5F method as previously described (Nicholas *et al.*, 2013). Briefly, cultured hESCs were dissociated using TrypLE™ Select (Gibco) and feeders were removed by incubating the cell suspension on 0.1% gelatin-coated 100 mm dishes (Corning) at 37°C for 2 hours on day 0. Feeder-free hESCs were plated at the density of 1 x 10^4 cells per well into 96-well round-bottom ultralow-attachment microplates (Corning) in NB-A/B27 medium [Neurobasal™-A Medium (Gibco) supplemented with 2% B-27 (Gibco), 1x NEAA, 1x Penicillin/Streptomycin, 1x GlutaMAX and 1x 2-ME] supplemented with 10 µM Y-27632 (Calbiochem), 10 µM SB 431542 (Tocris Bioscience), 2 µM Purmorphamine (PM) (Calbiochem), 1.5 µg/ml BMPRIA-Fc (R&D) and 250 ng/ml DKK1 (Gibco). After incubating at 37°C for 1 week, one large suspension embryoid body (sEB) was formed in each well. On day 7, sEBs from each 96-well microplate were transferred en bloc to a Matrigel-coated 100 mm dish and maintained in NB-A/B27 medium supplemented with 10 µM SB 431542, 2 µM PM, 1.5 µg/ml BMPRIA-Fc, and 250 ng/ml DKK1 for 1 week to form adherent embryoid bodies (aEBs). From day 14, aEBs were cultured in NB-A/B27 medium supplemented with 2 µM PM. On day 25 of differentiation, aEBs were dissociated using Accutase (Gibco) and then re-plated as dissociated monolayers of 3 x 10^5 cells per cm^2 onto poly-L-ornithine/laminin-coated 100 mm dishes and 24-well plates in NB-A/B27 medium supplemented with 2 µM PM. From day 28, cells were differentiated in NB-A/B27 medium supplemented with 2 µM PM and 10 µM DAPT. On day 35, *NKX2.1*-GFP^{+} cells were sorted from the neural differentiation culture via FACS using undifferentiated hESCs as negative control. Cells were dissociated using Accutase and re-suspended in NB-A/B27 medium supplemented with 10 µM Y-27632. Cells were kept on ice till right before the FACS, when the cells were pelleted and re-suspended in HBSS (Sigma) supplemented with 1% FBS, 20 mM glucose, 1x Penicillin/Streptomycin and 10 µM Y-27632. Then cells were filtered using a 50 µm Cup-Type Filcon (BD) into a 5 ml Round Bottom High Clarity Polypropylene Test Tube (Corning). hESC-derived cells were FACS-sorted using FACSAria™ II Flow Cytometer (BD), and FACS-sorted *NKX2.1*-GFP^{+} cells were collected into 500 µl NB-A/B27 medium supplemented with 10 µM Y-27632 and kept on ice till further analysis.

RET849#11 and #13 iPSCs (#13 *CDKL5*-mutant and #11 isogenic control) were differentiated into NPCs as previously described (Kim *et al.*, 2011). Briefly, cultured iPSCs were pre-treated with 5 µM Y-27632 for 30 minutes and dissociated using Accutase on day 0. iPSCs were seeded at the density of 3 x 10^6 cells per well into AggreWell™800 plate (Stemcell) in NB

medium [DMEM/F-12 with GlutaMAX™ Supplement (Gibco) supplemented with 1% N-2 (Gibco), 4% B-27, 1x Penicillin/Streptomycin and 1x 2-ME] supplemented with 5 µM Y-27632 and 200 ng/ml Noggin (R&D). On day 2, sEBs from each well of AggreWell™800 plate were transferred to a 90 mm Petri dish (Fisher) and cultured in NB medium supplemented with 5 µM Y-27632 and 200 ng/ml Noggin for 2 days. On day 4, sEBs were re-plated onto Matrigel-coated 60 mm dishes in NB medium supplemented with 200 ng/ml Noggin to form aEBs. From day 5, aEBs were maintained in NB medium supplemented with 20 ng/ml FGF2, 200 ng/ml Noggin and 200 ng/ml DKK1 to form rosettes for a few days. As soon as rosettes were clearly evident, they were collected and re-plated into Petri dishes and allowed to grow in suspension in NB medium supplemented with 20 ng/ml FGF2 and 10 ng/ml EGF (R&D) for 4 days to generate NPCs. iPSC-derived NPCs were expanded in NB medium supplemented with 20 ng/ml FGF2 and 10 ng/ml EGF in poly-L-ornithine/laminin-coated 6-well plates (Corning).

For the terminal differentiation of NPCs into neurons on astrocyte layer, astrocytes were seeded at 1 x 10^4 cells per well onto poly-D-lysine/fibronectin-coated 8-well glass chamber slides (Thermo). 1 day after seeding astrocytes, the #13 NPCs transduced with AAV-DJ vectors at the MOI of 3 x 10^3 vg per cell for 3 days, or the non-transduced #11 and #13 NPCs, were dissociated and re-plated on the astrocyte layer at 1-3 × 10^4 cells per well in NB medium supplemented with 20 ng/ml FGF2, 10 ng/ml EGF and 5 µM Y-27632. 1 day after seeding NPCs, terminal differentiation was initiated by replacing medium with TD medium (Neurobasal™ Medium (Gibco) supplemented with 1% N-2, 2% B-27, 15 mM HEPES solution (1 M) (Sigma), 1x NEAA, 1x Penicillin/Streptomycin, 1x GlutaMAX™ and 1x 2-ME) supplemented with 10 ng/ml BDNF (Alomone), 10 ng/ml GDNF (Alomone), 200 µM ascorbic acid (Sigma) and 1 mM dibutyryl cAMP (Sigma). NPCs were differentiated for 32 days into neurons.

Cloning and production of AAV vectors

The 5' tagged and codon-optimized *CDKL5* transgene sequences synthesized and cloned into ssAAV vector genome to generate pTR-CBh-HA-*hCDKL5_1*-BGH polyA and pTR-CBh-Myc-*hCDKL5_2*-BGH polyA. Briefly, the pTR-CBh-eGFP-BGH polyA was first constructed by replacing the CMV-*LacZ* sequence of pTR-CMV-*LacZ*-BGH polyA (NGVB) with CBh-eGFP insert from pTRs-KS-CBh-eGFP (NGVB). Then eGFP sequence was amplified by PCR using GFP primers (Supplementary Table 1) and re-cloned into pTR-CBh-eGFP-BGH polyA, in order to import a 5' NheI and a 3' HindIII restriction site flanking the eGFP transgene. To

construct pTR-CBh-HA-*hCDKL5_1*-BGH polyA plasmid, eGFP transgene of pTR-CBh-eGFP-BGH polyA was replaced with synthesized HA-*hCDKL5_1* sequence via restriction digest using NheI/BamHI followed by DNA ligation. To construct pTR-CBh-Myc-*hCDKL5_2*-BGH polyA plasmid, eGFP transgene of pTR-CBh-eGFP-BGH polyA was replaced with synthesized Myc-*hCDKL5_2* sequence via restriction digest using NheI/HindIII followed by DNA ligation. pTR-CBh-eGFP-BGH polyA-*LacZ* stuffer vector plasmid was constructed as positive control. A *LacZ* stuffer sequence was inserted after BGH polyA to lengthen the eGFP plasmid size to 6864 bp, which was similar to the 6867 bp HA-*hCDKL5_1* and 7012 bp Myc-*hCDKL5_2* plasmids.

AAV9 and AAV-DJ vectors were prepared via 3-plasmid co-transfection of HEK 293T cells using PEI as previously described (Gray *et al.*, 2011a). Briefly, HEK 293T cells in 150 mm dishes (Corning) (1.21 x 10^7 cells per dish) were transfected with 13 µg rAAV vector plasmid, 13 µg capsid plasmid and 26 µg pXX6-80 helper plasmid mixed with 156 µg PEI in 3 ml DMEM supplemented with 2 mM L-Glutamine and 1x Penicillin/Streptomycin per dish. 48-72 hours post-transfection, viral particles were harvested from both cells and media by centrifugation at 2500 x g for 10 minutes at 4 °C. Media supernatant was stored at 4°C and cell pellets were resuspended in 50 mM Tris-HCl, 150 mM NaCl and 2 mM $MgCl_2$, pH 8.0, lysed through 3 sequential freeze-thaw cycles, and incubated with 50 U/ml Benzonase® Nuclease (Sigma) at 37°C for 30 minutes. Cell lysate was centrifuged at 2500 x g for 30 minutes at 4°C and the supernatant was combined with the previous media supernatant stored at 4°C. The clarified supernatant was precipitated with 8% poly(ethylene glycol) (PEG) (Sigma) and 0.5 M NaCl (Ayuso *et al.*, 2010), centrifuged and then resuspended in PBS. rAAVs were purified using iodixanol gradients (15%, 25%, 40% and 54%) (Zolotukhin *et al.*, 1999) prepared from OptiPrep™ Density Gradient Medium (60% iodixanol) (Sigma) by centrifugation at 69000 rpm for 90 minutes at 18°C and then concentrated using Amicon Ultra-15 Centrifugal Filter Unit with Ultracel-100 membrane (Millipore) in PBS with 0.001% Pluronic F-68 (Gibco).

For the preparation of AAV-PHP.B vectors, the above rAAV production protocol was modified (Deverman *et al.*, 2016) as follows. HEK 293T cells (9.12 x 10^6 cells per dish) were transfected with 5.7 µg rAAV vector plasmid, 22.8 µg AAV-PHP.B capsid plasmid and 11.4 µg pXX6-80 helper plasmid mixed with 142.12 µg PEI in 2 ml DPBS per dish. rAAVs were harvested from the media only at 72 hours post-transfection and from both cells and media at 120 hours. Cell pellets were resuspended in 50 mM Tris-HCl, 500 mM NaCl and 2 mM $MgCl_2$, pH 8.5. Cell lysate was the incubated with 100 U/ml Salt Active Nuclease (Sigma) at 37°C for 1 hour.

Supernatant was precipitated with 8% PEG and 0.5 M NaCl before added to the cell lysate. And 60% iodixanol was used as the highest gradient instead of 54%.

Behavioural analysis

Open Field

Locomotor activity was assessed using EthoVision XT tracking software (Noldus). Mice were individually placed in a wooden arena (45 x 45 x 45 cm) with the base covered in sawdust. Each mouse was released into a corner of the box and was allowed to explore for 1 hour. Mice were videoed from above and the tracking system recorded the distance the mice travelled.

Hind-limb Clasping

Mice were suspended by tail for 10 seconds and clasping of hind limbs were scored from 0 to 3. Mice were assigned a score of 0 if the hind limbs were consistently splayed outward away from the abdomen. If one hind limb was retracted toward the abdomen for more than 50% of the time suspended, mice received a score of 1. If both hind limbs were partially retracted toward the abdomen for more than 50% of the time suspended, mice received a score of 2. A score of 3 was given if the hind limbs were entirely retracted and touching the abdomen for more than 50% of the time suspended (Guyenet *et al.*, 2010).

Rotarod

A rotarod apparatus (Ugo Basile) was used to measure fore- and hind-limb motor coordination, balance and strength. Mice received three trials per day with an inter-trial interval of 1 hour for 3 consecutive days. The rod accelerated from 5 to 60 rpm over a period of 10 minutes and the latency to fall was recorded.

Elevated O-Maze

The elevated O-maze was used to assess anxiety-like state using EthoVision XT tracking software for automated tracking of location preference. The maze was elevated 50 cm above the floor, 53 cm in diameter with a corridor width of 8 cm and divided into 4 equal-sized zones. Two opposite quadrants were “open” and the remaining two “closed” quadrants were surrounded by 15 cm high dark, opaque walls. Mice were individually placed on the maze at a randomly chosen boundary between an open and a closed zone, facing the inside of the closed

zone and allowed to explore for 10 minutes. Mice were videoed from above and the tracking system recorded the time spent in the open zones of the maze and the distance travelled.

Marble Burying

The marble burying test was used to assess repetitive and anxiety-like behaviour. Mice were individually placed in a wooden arena (45 x 45 x 45 cm) filled with 5 cm of sawdust and 20 marbles placed on top of the sawdust in a 5 x 4 formation. Mice were allowed to freely explore the cage for 20 minutes, and at the end of the test the number of successfully buried marbles was counted. A marble was defined as "buried" when only 1/3 of the marble was visible.

Social Interaction

Mice, who were not cage mates, were arranged into pairs of the same genotype. They were placed at opposite corners of a wooden arena (45 x 45 x 45 cm) which had the base covered with sawdust and allowed to freely interact with each other for 10 minutes. The time spent interacting was recorded.

Three-chambered social approach

The social approach apparatus is an open-topped box made of acrylic, which is divided into three chambers with two clear acrylic walls. The dividing walls have retractable doors allowing access into each chamber. Test mice were confined to the centre chamber at the beginning of each phase. Before the start of the test and in a counter-balanced order, one end chamber was designated the "social chamber" into which a stimulus mouse was placed, and the other end chamber was the "non-social chamber" that remained empty. In the habituation phase of the test, mice were placed in the centre chamber and allowed to explore all three chambers for 10 minutes. During this acclimation period, baseline measurements of how much time the mouse spent in each of the three chambers and how many transitions the mouse made between chambers were recorded. In the sociability phase of the test, a stimulus mouse (stranger 1) of a similar size was placed in a grid enclosure in the social chamber while an empty grid enclosure was placed into the non-social chamber. The test mouse was then allowed to explore for 10 minutes and the time spent in each of the 3 chambers and the number of transitions was then recorded. Following this phase, another stimulus mouse (stranger 2) was placed in the grid enclosure in the non-social chamber and again the test mouse was allowed to explore for 10 minutes. The time spent in each chamber and the number of transitions was recorded.

Nesting

Mice were individually placed in a cage with no environmental enrichment items such as tissues and tunnels. Approximately 1 hour before the dark cycle a Nestlet (Datesand) was weighed and then placed into each cage. The following morning the nests made by the mice were assessed and any untorn Nestlet pieces were weighed. The nests were given a score from 1-5 (Deacon, 2006). A score of 1 was given if the Nestlet was not noticeably touched (more than 90% intact). If the Nestlet was partially torn (50–90% remaining intact) it was given a score of 2. A score of 3 was given if the Nestlet mostly shredded but there was no obvious nest site. If the nest was identifiable but flat, then a score of 4 was given; and if a 'perfect' nest was seen then it was given a score of 5.

Y-maze Spontaneous Alternation

Mice were placed in a Plexiglas Y-maze apparatus that has 3 identical arms placed at 120° with respect to each other. Each mouse was placed at the end of one arm and allowed to explore the apparatus freely for 5 minutes. Spontaneous alternation performance (SAP) was assessed visually by scoring the pattern of entries into each arm during the 5-minute test. Spontaneous alternations (SAP) were defined as successive entries into each of the three arms as a triplet set (i.e., ABC, CBA, ...). Percentage spontaneous alternation was defined as the ratio of actual (= total alternations) to possible (=total arm entries -2) number of alternations × 100. Alternate arm returns (AAR) (i.e., ABA, CBC, …) were also scored. Total entries were scored as an index general activity in the Y-maze.

Contextual and Cued Fear Conditioning

Background fear conditioning has two components that can be tested; hippocampus- and amygdala-dependent contextual fear conditioning and amygdala-dependent cued fear conditioning (Anagnostaras *et al.*, 2001). Mice were individually placed in a conditioning chamber in a soundproof box (NIR Video Fear Conditioning System, Med Associates). After 150 seconds, a tone (90 dB, 10 kHz) was presented for 30 seconds, the last 2 seconds coinciding with a footshock (0.7 mA). After a further 60 seconds, the mice received another tone and shock, and after 60 seconds were returned to their home cage. To test for contextual memory, the mice were placed back into the conditioning chamber 24 hours after training and freezing behaviour was scored. To assess cue-dependent fear conditioning the mice were placed into a novel chamber 24 hours after the context test. Freezing behaviour was assessed during a 3-

minute baseline period (Pre-CS), followed by a 3-min presentation of the tone (CS). Freezing behaviour was scored as no movement other than respiration and was scored by the NIR software.

Supplementary Tables

Supplementary Table 1. List of RACE and RT-PCR primers

Primers	Sequence (5' to 3')
GSP1	GAGACGGTTCTGCTGAGATCTGCTGTTTGAC
GSP2	GAGATCTACCATCAGAGAGCAGTTCTGGAACC
3'-CDS *hCDKL5_1*	AAGCAGTGGTATCAACGCAGAGTACGGCACCCAGCTGTTCAGAG TAGGAA
3'-CDS *hCDKL5_5*	AAGCAGTGGTATCAACGCAGAGTACGCCGCATTCTCATGGTATGT CAGGAG
GFP Fwd	GCGCACCGGTGCTAGCCGCCACCATGGTGAGCAAGGG
GFP Rev	GCGCGGATCCAAGCTTTTACTTGTACAGCTCGTCCATGCCG

Supplementary Table 2. List of mice injected with AAV vectors

Mouse strain	Genotype	Vectors injected	Dose (vg per animal)	Number of animals
C57BL/6	WT	Saline	-	Pre-injected 25% mannitol: n = 4 No mannitol: n = 2
	WT	AAV9-eGFP	1 x 10^{12}	Pre-injected 25% mannitol: n = 5 No mannitol: n = 3
	WT	AAV-PHP.B-eGFP	1 x 10^{12}	Pre-injected 25% mannitol: n = 2 No mannitol: n = 3
Cdkl5 KO	*Cdkl5*$^{-/y}$	AAV-PHP.B-eGFP	1 x 10^{12}	n = 10
	Cdkl5$^{-/y}$	AAV-PHP.B-HA-*hCDKL5_1*	1 x 10^{12}	n = 10
	Cdkl5$^{+/y}$	Saline	-	n = 7

Supplementary Table 3. List of mice for behavioural testing

Group	Genotype	Vectors injected	Number of animals
Cdkl5 KO	*Cdkl5*$^{+/y}$	Saline	n = 10
	Cdkl5$^{-/y}$	Saline	n = 10
AAV-injected *Cdkl5* KO	*Cdkl5*$^{-/y}$	AAV-PHP.B-eGFP (1 x 10^{12} vg per animal)	n = 10
	Cdkl5$^{-/y}$	AAV-PHP.B-HA-*hCDKL5_1* (1 x 10^{12} vg per animal)	n = 10
	Cdkl5$^{+/y}$	Saline	n = 7

Supplementary Table 4. List of primary antibodies

Primary antibody	Host species	Dilution	Source
Anti-6x His tag	Rabbit polyclonal	WB 1:500	Abcam, ab125262
Anti-CaMKII-α	Rabbit	WB 1:1000	CST, 3357
Anti-CB	Guinea pig polyclonal	IHC 1:500	Synaptic Systems, 214004
Anti-CDKL5	Mouse monoclonal	WB 1:500-1:1000	Santa Cruz, sc-376314
Anti-CDKL5	Rabbit polyclonal	WB 1:500	Sigma, HPA002847
Anti-FOXG1	Rabbit polyclonal	ICC 1:1000	Abcam, ab18259
Anti-GAPDH	Mouse monoclonal	WB 1:1000	Santa Cruz, sc-47724
Anti-GAPDH	Rabbit monoclonal	WB 1:2500	CST, 2118
Anti-GFAP	Rabbit polyclonal	IHC 1:1000	Millipore, AB5804
Anti-GFP	Rabbit polyclonal	WB 1:1000	Abcam, ab290
Anti-GFP	Goat polyclonal	ICC 1:1000	Abcam, ab5450
Anti-GFP	Chicken polyclonal	ICC 1:2000 IHC 1:1000	Abcam, ab13970
Anti-HA tag	Mouse monoclonal	ICC 1:1000	Sigma, H3663
Anti-HA tag	Rabbit polyclonal	WB 1:1000	Abcam, ab9110
Anti-HA tag	Rabbit monoclonal	IHC 1:500 WB 1:1000	CST, 3724
Anti-HA-HRP	Mouse monoclonal	WB 1:5000	MACS, 130-091-972
Anti-His tag	Mouse monoclonal	WB 1:1000	Millipore, 70796
Anti-Myc tag	Mouse monoclonal	ICC 1:1000 WB 1:1000	Millipore, 05-419
Anti-Myc tag	Rabbit polyclonal	ICC 1:500	Abcam, ab9106
Anti-Nestin	Mouse monoclonal	ICC: 1:200	Millipore, MAB5326
Anti-NeuN	Rabbit monoclonal	IHC 1:1000	Abcam, ab177487
Anti-OCT4	Rabbit polyclonal	ICC 1:500	Abcam, ab19857
Anti-PSD95	Rabbit monoclonal	ICC 1:500 IHC 1:500 WB 1:1000	CST, 3450
Anti-SOX1	Goat polyclonal	ICC 1:200	R&D, AF3369
Anti-SSEA4	Mouse monoclonal	ICC 1:500	Abcam, ab16287
Anti-TH	Rabbit polyclonal	IHC 1:500	Millipore, AB152
Anti-TRA-1-60	Mouse monoclonal	ICC 1:500	Abcam, ab16288
Anti-TUJ1	Mouse	ICC 1:1000	BioLegend, 801201
Anti-VGLUT1	Rabbit polyclonal	ICC 1:2000	Synaptic Systems, 135302

Supplementary Table 5. List of secondary antibodies

Secondary antibody	Dilution	Source
Goat anti-Mouse IgG (H+L) Highly Cross-Adsorbed Secondary Antibody, Alexa Fluor 488	ICC 1:400	Invitrogen, A11029
Goat anti-Mouse IgG (H+L) Highly Cross-Adsorbed Secondary Antibody, Alexa Fluor 546	ICC 1:400	Invitrogen, A11030
Goat anti-Mouse IgG (H+L) Highly Cross-Adsorbed Secondary Antibody, Alexa Fluor 594	ICC 1:400	Invitrogen, A11032
Goat anti-Rabbit IgG (H+L) Highly Cross-Adsorbed Secondary Antibody, Alexa Fluor 488	ICC 1:400	Invitrogen, A11034
Goat anti-Rabbit IgG (H+L) Highly Cross-Adsorbed Secondary Antibody, Alexa Fluor 546	ICC 1:400 IHC 1:500	Invitrogen, A11035
Goat anti-Rabbit IgG (H+L) Highly Cross-Adsorbed Secondary Antibody, Alexa Fluor 594	IHC 1:500	Invitrogen, A11037
Goat anti-Chicken IgY (H+L) Secondary Antibody, Alexa Fluor 488	ICC 1:400 IHC 1:500	Invitrogen, A11039
Donkey anti-Goat IgG (H+L) Cross-Adsorbed Secondary Antibody, Alexa Fluor 488	ICC 1:400	Invitrogen, A11055
Goat anti-Guinea Pig IgG (H+L) Highly Cross-Adsorbed Secondary Antibody, Alexa Fluor 633	IHC 1:500	Invitrogen, A21105
Donkey anti-Mouse IgG (H+L) Highly Cross-Adsorbed Secondary Antibody, Alexa Fluor 488	ICC 1:400	Invitrogen, A21202
Peroxidase AffiniPure Goat anti-Mouse IgG (H+L)	WB 1:10000	Jackson ImmunoResearch, 115-035-003
Donkey anti-Rabbit IgG H&L (HRP)	WB 1:2000	Abcam, ab16284

Supplementary Figure legends

Supplementary Figure 1. Identification of *hCDKL5* isoforms in human brain cerebral cortex, testis, neuronal cell lines and glia via RACE and RT-PCR.

Full-length gels of Fig 1 B.

A Positive control RACE PCR of mouse transferrin receptor (*TFR*) using Mouse Heart Total RNA (Takara Bio). This was the internal positive control provided by the manufacturer, in order to confirm the reliability of the RACE results obtained in-house. Lane L1: 1 kb DNA ladder (NEB). Lane 1: 5'-RACE *TFR* product, 2.1 kb as expected according to manufacturer's instructions. Lane 2: 3'-RACE *TFR* product, 3.1 kb as expected. Lane 3: 5'-internal positive control, 380 bp as expected. Lane 4: 3'-internal positive control, 380 bp as expected. Lane 5: non-template negative control. Lane L2: 100 bp DNA ladder (NEB).

B-D Identification of *hCDKL5* isoforms in human brain cerebral cortex via RACE PCR using Human Cerebral Cortex Poly A+ RNA.

B 5'-RACE PCR of *CDKL5*. Lane L: 1 kb DNA ladder. Lane 1: 5'-RACE *CDKL5* product, 1.6 kb, sequence corresponds to the *hCDKL5_1* and/or *hCDKL5_2* isoforms. Lane 2: 5' internal positive control, 202 bp. Lane 3: Forward primer (UPM) only negative control. Lane 4: Reverse primer (GSP1) only negative control.

C-D 3'-RACE PCR of *CDKL5*. *hCDKL5_1* (634 bp product) and to a lesser extent *hCDKL5_2* (757 bp product) isoforms were detected in human brain cerebral cortex, whereas *hCDKL5_5* (915 bp product) isoform was not detected.

C 3'-RACE PCR of *CDKL5*. Lanes L: 2-log DNA ladder (NEB). Lanes 1-3 and 7: 3'-RACE using 3'-CDS *hCDKL5_1* primer to amplify *hCDKL5_1* and/or *hCDKL5_2* isoforms. Lanes 1 and 7: 3'-RACE *CDKL5*, 634 bp product from *hCDKL5_1* and 757 bp from *hCDKL5_2*. Lane 2: Reverse primer (UPM) only negative control. Lane 3: Forward primer (GSP2) only negative control. Lanes 4-6 and 8: 3'-RACE using 3'-CDS *hCDKL5_5* primer to amplify *hCDKL5_5* isoform. Lanes 4 and 8: 3'-RACE *CDKL5*. Lane 5: Reverse primer (UPM) only negative control. Lane 6: Forward primer (GSP2) only negative control.

D Identification of *hCDKL5* isoforms in human testis via RT-PCR using Human Testis Total RNA. This was the positive control RT-PCR to confirm the reliability of RT-PCR results from neuronal and glial cell lines. Lane L: 2-log DNA ladder. Lane 1: RT-PCR using 3'-CDS

hCDKL5_1 primer to amplify *hCDKL5_1* and/or *hCDKL5_2* isoforms, 634 bp product from *hCDKL5_1*. Lane 2: non-template control of Lane 1 reaction. Lane 3: RT-PCR using 3'-CDS *hCDKL5_5* primer to amplify *hCDKL5_5* isoform, 915 bp product from *hCDKL5_5*. Lane 4: non-template control of Lane 3 reaction. Both *hCDKL5_1* (634 bp product) and *hCDKL5_5* (915 bp product) isoforms were detected in human testis, consistent with previously published data (Williamson *et al.*, 2012; Hector *et al.*, 2016).

E-H Identification of *hCDKL5* isoforms in neuronal (E-G) and glial (H) cell lines via RT-PCR using total RNA extracted. *hCDKL5_1* (634 bp product) and to a lesser extent *hCDKL5_2* (757 bp product) isoforms were detected in both neuronal and glial cell lines, whereas *hCDKL5_5* (915 bp product) isoform was not detected.

E RT-PCR of *CDKL5* using total RNA from undifferentiated and differentiated SH-SY5Y cells. Lanes L: 2-log DNA ladder. Lanes 1-4: undifferentiated SH-SY5Y cells. Lanes 5-8: differentiated SH-SY5Y cells. Lanes 1 and 5: RT-PCR using 3'-CDS *hCDKL5_1* primer, 634 bp product from *hCDKL5_1* and 757 bp from *hCDKL5_2*. Lanes 2 and 6: non-template control of Lanes 1 and 5 reactions, respectively. Lanes 3 and 7: RT-PCR using 3'-CDS *hCDKL5_5* primer. Lanes 4 and 8: non-template control of Lanes 3 and 7 reactions, respectively.

F-G Identification of *hCDKL5* isoforms in *NKX2.1*-GFP$^+$ cortical interneurons.

F RT-PCR of *CDKL5* using total RNA from unsorted hESC-derived *NKX2.1*-GFP$^+$ cortical interneurons. hESC-derived culture without FACS-sorting was a mixture of *NKX2.1*-GFP$^+$ interneurons and GFP$^-$ cells. L: 2-log DNA ladder. Lane 1: RT-PCR using 3'-CDS *hCDKL5_1* primer, 634 bp product from *hCDKL5_1* and 757 bp from *hCDKL5_2*. Lane 2: non-template control of Lane 1 reaction.

G RT-PCR of *CDKL5* using total RNA from FACS-sorted hESC-derived *NKX2.1*-GFP$^+$ cortical interneurons. *NKX2.1*-GFP$^+$ interneurons were selected from hESC-derived culture via FACS-sorting. L: 2-log DNA ladder. Lane 1: RT-PCR using 3'-CDS *hCDKL5_1* primer, 634 bp product from *hCDKL5_1*. Lane 2: non-template control of Lane 1 reaction. Only *hCDKL5_1* was detected in FACS-sorted *NKX2.1*-GFP$^+$ cortical interneurons, which might be due to the relatively low abundance of *hCDKL5_2* in the brain (less than 10%) (Hector *et al.*, 2016).

H RT-PCR of *CDKL5* using total RNA from primary human astrocytes. Lane L: 2-log DNA ladder. Lane 1: RT-PCR using 3'-CDS *hCDKL5_1* primer, 634 bp product from *hCDKL5_1*

and 757 bp from *hCDKL5_2*. Lane 2: non-template control of Lane 1 reaction. Lane 3: RT-PCR using 3'-CDS *hCDKL5_5* primer. Lane 4: non-template control of Lane 3 reaction.

Supplementary Figure 2. CDKL5 expression in different human cell lines and *hCDKL5* transgene over-expression in HEK 293T cells transfected with AAV vector plasmids.

A WB of CDKL5 expression in different human cell lines. Full-length blots of Fig 1 D. Lanes S: protein standard (Novex™ Sharp Pre-stained Protein Standard, Invitrogen). Lane 1: Differentiated SH-SY5Y cells. Lane 2: Undifferentiated SH-SY5Y cells. Lane 3: HEK 293T cells. Lane 4: HEK 293 cells. Lane 5: HeLa cells, positive control according to the datasheet of mouse anti-CDKL5 monoclonal antibody. Lane 6: Primary human astrocytes. Lane 7: HES-3 *NKX2.1*$^{GFP/w}$ hESCs. Lane 8: cell lysis buffer, no cell lysate, negative control. GAPDH: loading control. 8.7 μg total protein was loaded for each cell line.

B-C WB of transgene expression in HEK 293T cells transfected with AAV vector plasmids. Full-length blots of Fig 1 F. 10 μg total protein was loaded for each sample. Untransfected 293T cells: negative control. GAPDH: loading control.

B WB of hCDKL5 and tag expression in HEK 293T cells transfected with AAV-*hCDKL5* plasmids. In addition to *hCDKL5* transgene expression, WB of transgene tags was performed to examine the tag expression. Expression of the HA tag of HA-hCDKL5_1 and the Myc tag of Myc-hCDKL5_2 was detected via WB, whereas the His tag of His-hCDKL5_2 was not detected. Thus, expression of both transgenes and tags were verified for AAV-HA-*hCDKL5_1* and AAV-Myc-*hCDKL5_2* plasmids.

C WB of GFP over-expression in HEK 293T cells transfected with AAV-eGFP plasmids. This was used as positive control of WB.

Supplementary Figure 3. Comparison of AAV9 and AAV-PHP.B transduction in various mouse brain regions.

Representative images showing that both AAV9 and AAV-PHP.B vectors transduced NeuN$^+$ (red) neurons in cortex, hippocampus, striatum and thalamus, and Purkinje cells in cerebellum. Cell nuclei were counterstained with DAPI (blue). Scale bars: 50 μm.

Supplementary Figure 4. AAV-PHP.B transduction in *Cdkl5*$^{-/y}$ mouse brain following intrajugular injection.

AAV-PHP.B-HA-*hCDKL5_1* or AAV-PHP.B-eGFP, at 1 × 10^{12} vg per animal, was intrajugularly injected into *Cdkl5*$^{-/y}$ mice at age 28-30 days. Images show transgene expression 3 months after injection.

A Representative sagittal brain sections with GFP immunostaining of *Cdkl5*$^{-/y}$ mice injected with AAV-PHP.B-eGFP (bottom) or saline (top).

B Quantitative analysis of AAV-PHP.B-eGFP biodistribution in *Cdkl5*$^{-/y}$ mouse brain relative to saline-injected controls. Data are presented as mean ± SEM. n = 5 per group. Unpaired t-test; ****P<0.0001.

C AAV-PHP.B-HA-*hCDKL5_1* transduction in *Cdkl5*$^{-/y}$ mouse brain. HA-hCDKL5_1 expression delivered by AAV-PHP.B was mainly in hippocampal CA1 region and cerebellar Purkinje cells, and in cortex to a lesser extent. Due to the lack of a reliable and reproducible antibody that specifically detects CDKL5 in brain sections (Zhou *et al.*, 2017), cells transduced by AAV-PHP.B-HA-*hCDKL5_1* should be labelled with HA tag via IHC/IF, the signal of which is not as prominent as GFP. Scale bars: 25 μm.

Supplementary Figure 5. Alterations in protein expression profile in the forebrain and midbrain of *Cdkl5*$^{-/y}$ mice via hCDKL5_1 expression.

A WB analysis of CDKL5, PSD95, CaMKII-α and GAPDH expression in forebrain and midbrain. Lanes S: protein standard. Lanes 1, 10 and 11: *Cdkl5*$^{+/y}$ + saline. Lanes 2-6: *Cdkl5*$^{-/y}$ + hCDKL5_1. Lanes 7-9 and 14-15: *Cdkl5*$^{-/y}$ + GFP. Lanes 12-13: *Cdkl5*$^{-/y}$ + saline. Lanes 1: *Cdkl5*$^{+/y}$ + saline, sample processing control of 2 blots. GAPDH: loading control. 34 μg total protein was loaded for each cell line.

B-D Quantitative analysis of CDKL5 (B), PSD95 (C) and CaMKII-α (D) expression normalised to GAPDH in forebrain and midbrain. The samples on the 2 blots were derived from the same experiment and blots were processed in parallel, using the same *Cdkl5*$^{+/y}$ + saline sample loaded on each blot as the sample processing control (Lanes 1). Data are presented as mean ± SEM. Saline-treated *Cdkl5*$^{+/y}$ mice: n = 3; hCDKL5_1-treated *Cdkl5*$^{-/y}$ mice: n = 5; GFP-treated *Cdkl5*$^{-/y}$ mice: n = 5; saline-treated *Cdkl5*$^{-/y}$ mice: n = 2. One-way ANOVA with Tukey's multiple comparisons test (B-C) and unpaired t-test (D); *P<0.05, **P<0.01, ***P<0.001.

Supplementary Figure 6. Alterations in protein expression profile in the hindbrain of *Cdkl5*$^{-/y}$ mice via hCDKL5_1 expression.

A WB analysis of CDKL5, PSD95, CaMKII-α and GAPDH expression in hindbrain. Lanes S: protein standard. Lanes 1, 10 and 11: *Cdkl5*$^{+/y}$ + saline. Lanes 2-6: *Cdkl5*$^{-/y}$ + hCDKL5_1. Lanes 7-9 and 14-15: *Cdkl5*$^{-/y}$ + GFP. Lanes 12-13: *Cdkl5*$^{-/y}$ + saline. Lanes 1: *Cdkl5*$^{+/y}$ + saline, sample processing control of 2 blots. GAPDH: loading control. 34 µg total protein was loaded for each cell line.

B~~-C~~ Quantitative analysis of ~~CDKL5 (B) and~~ PSD95 ~~(C)~~ expression normalised to GAPDH in hindbrain. CaMKII-α expression was not detected in the hindbrain for the quantification purpose. The samples on the 2 blots were derived from the same experiment and blots were processed in parallel, using the same *Cdkl5*$^{+/y}$ + saline sample loaded on each blot as the sample processing control (Lanes 1). Data are presented as mean ± SEM. Saline-treated *Cdkl5*$^{+/y}$ mice: n = 3; hCDKL5_1-treated *Cdkl5*$^{-/y}$ mice: n = 5; GFP-treated *Cdkl5*$^{-/y}$ mice: n = 5; saline-treated *Cdkl5*$^{-/y}$ mice: n = 2. One-way ANOVA with Tukey's multiple comparisons test; ~~*P<0.05,~~ **P<0.01, ***P<0.001.

Supplementary Figure 7. Characterization of RET849 #11 isogenic control and #13 *CDKL5*-mutant iPSC lines

A Direct sequencing of *CDKL5* RT-PCR products using total RNA from RET849 iPSCs. #11 isogenic control and #13 mutant sequences are shown with the mutated nucleotide outlined in red. Compared to the #11 iPSCs, there was a deletion of GAAA in the exon 5 of *CDKL5* gene in the #13 iPSCs, resulting in the pGlu55fs*74 frameshift mutation.

B WB analysis of CDKL5 expression in RET849 #11 and #13 iPSC lines verified no CDKL5 protein expression in #13 iPSCs relative to #11 cells. '+': positive control, HeLa cells. '-': negative control, cell lysis buffer, no cell lysate. GAPDH: loading control. 10 µg total protein was loaded for each cell line.

C-D ICC/IF of hESC markers in RET849 #11 and #13 iPSCs validated the embryonic stem cell-like pluripotency of both lines. #11 (C) and #13 (B) iPSC lines were labelled with SSEA4 (red), and co-labelled with TRA-1-60 (red) and OCT4 (green). Cell nuclei were counterstained with DAPI (blue). Scale bars: 50 µm.

E-F Array-CGH analysis on both #11 (E) and #13 (F) iPSC lines confirmed the presence of a normal 46 XX karyotype without chromosomal rearrangements. An overview of array results for all chromosomes is shown on the left; the ideogram of chromosome X is reported on the right.

Supplementary Figure 8. Characterization of RET849 iPSC-derived NPCs and terminal differentiation of non-transduced and AAV-DJ-transduced NPCs into neurons.

A-B ICC/IF of NPC markers in RET849 #11 and #13 iPSC-derived NPCs confirmed their characteristics of telencephalic neural stem cells. #11 (A) and #13 (B) iPSC-derived NPCs were co-labelled with neural stem cell markers Nestin (red) and SOX1 (green), and co-labelled with Nestin (red) and telencephalon marker FOXG1 (green). Cell nuclei were counterstained with DAPI (blue). Scale bars: 50 µm.

C *In vitro* AAV-DJ-eGFP transduction in #11 and #13 iPSC-derived NPCs. Non-transduced #11 and #13 NPCs were used as negative controls, with %GFP^+ cells less than 0.1%, respectively.

D Diagram outlining terminal differentiation protocol for non-transduced #11 and #13 NPCs co-cultured with astrocytes into neurons for 32 days. Schematics representing NPCs, astrocytes and neurons were adopted from Russo *et al.* (2018).

E Diagram outlining terminal differentiation protocol for #13 NPCs transduced by AAV-DJ vectors co-cultured with astrocytes into neurons for 32 days. Schematics representing NPCs, astrocytes and neurons were adopted from Russo *et al.* (2018).

Supplementary Figure 9. Calcium imaging using fluo-4 in RET849 iPSC-derived neurons.

A Epifluorescence image of fluo-4 in #11 neurons and astrocytes.

B Transient cytosolic Ca^{2+} changes induced by bath application of 50 mM KCl in fluo-4-loaded #11 neurons (n = 50).

C Epifluorescence image of fluo-4 in #13 neurons and astrocytes.

D Transient cytosolic Ca^{2+} changes induced by bath application of 50 mM KCl in fluo-4-loaded #13 neurons (n = 50).

E Epifluorescence image of fluo-4 in #13 neurons transduced with AAV-DJ-eGFP vectors and astrocytes.

F Transient cytosolic Ca^{2+} changes induced by bath application of 50 mM KCl in fluo-4-loaded #13 neurons transduced with AAV-DJ-eGFP vectors (n = 30).

G Epifluorescence image of fluo-4 in #13 neurons transduced with AAV-DJ-HA-*hCDKL5_1* vectors and astrocytes.

H Transient cytosolic Ca^{2+} changes induced by bath application of 50 mM KCl in fluo-4-loaded #13 neurons transduced with AAV-DJ-HA-*hCDKL5_1* vectors (n = 30).

I Epifluorescence image of fluo-4 in #13 neurons transduced with AAV-DJ-Myc-*hCDKL5_2* vectors and astrocytes.

J Transient cytosolic Ca^{2+} changes induced by bath application of 50 mM KCl in fluo-4-loaded #13 neurons transduced with AAV-DJ-Myc-*hCDKL5_2* vectors (n = 26).

When given KCl stimulus, only neurons would show an increase in fluo-4 fluorescence indicating Ca^{2+} transient influxes, but not astrocytes. Intracellular Ca^{2+} changes are presented as ratios of the fluorescence change and basal fluorescence ($\Delta F/F_0$). Data are presented as mean ± SEM. Scale bars: 25 μm.

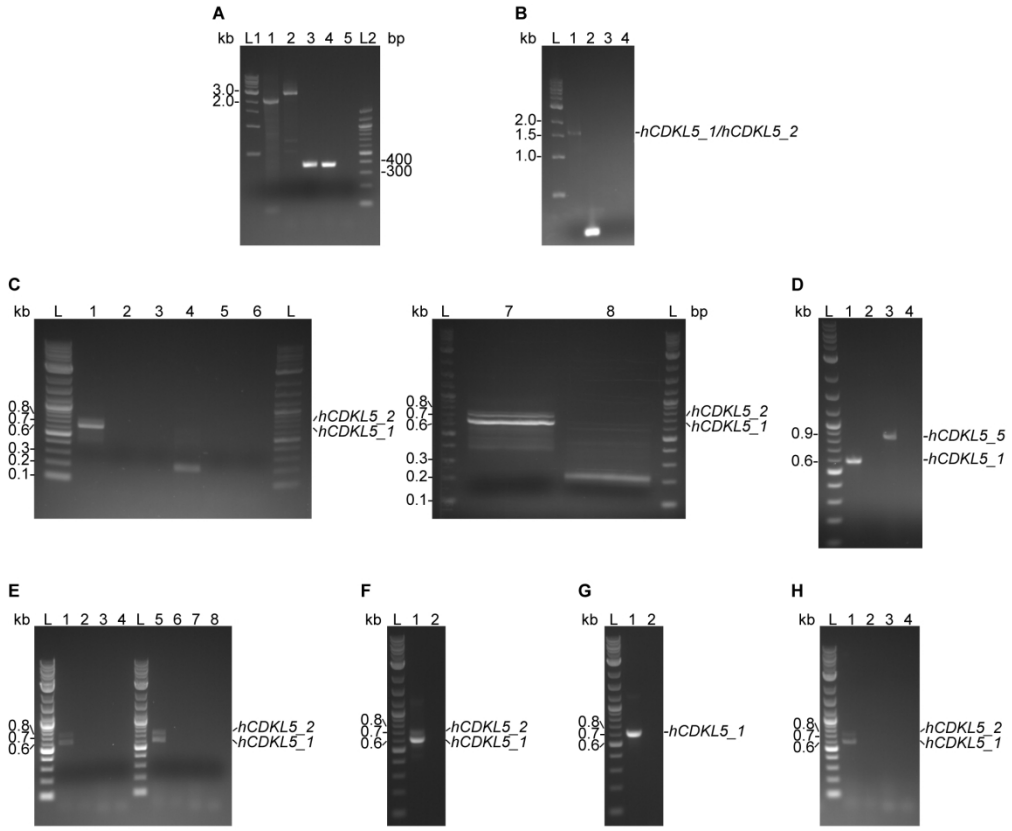

Supplementary Figure 1

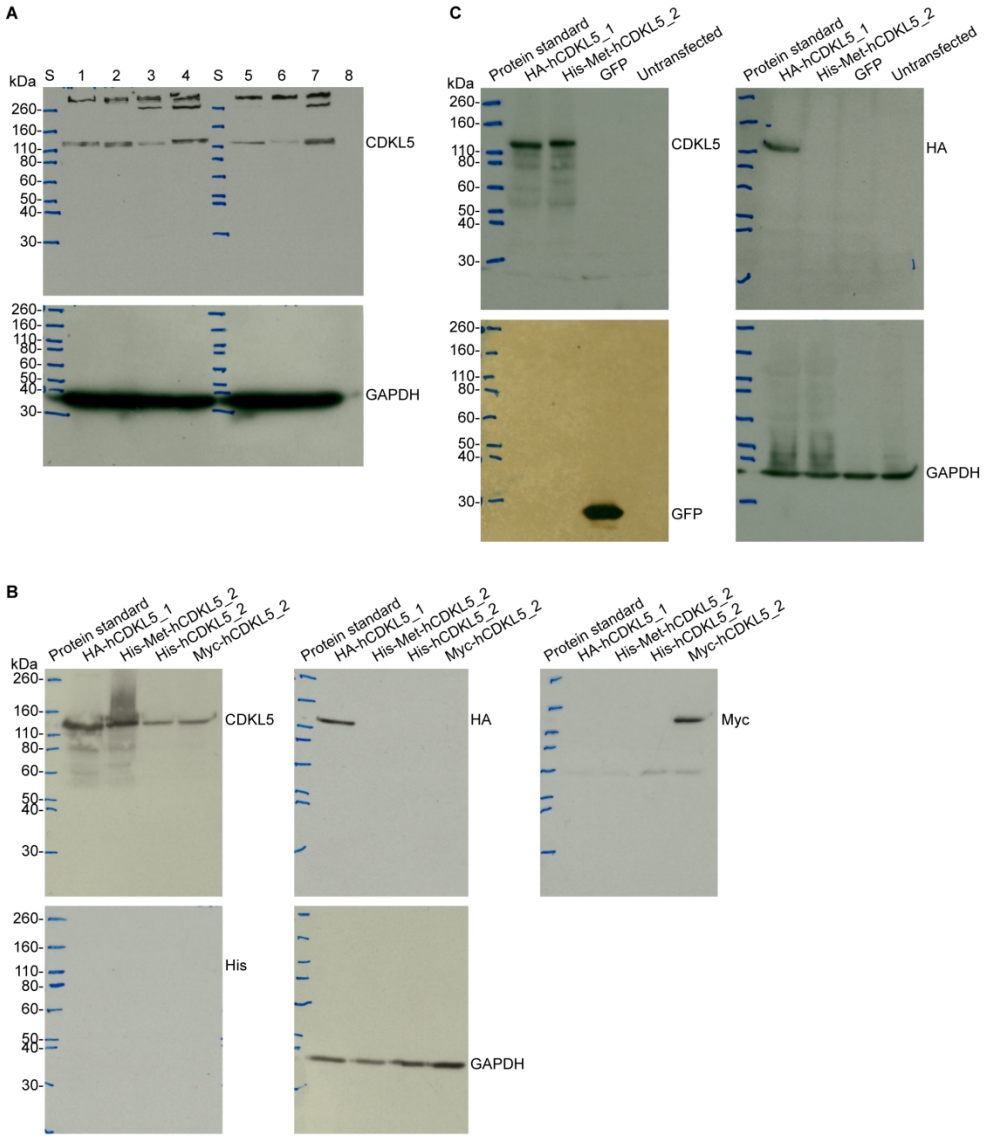

Supplementary Figure 2

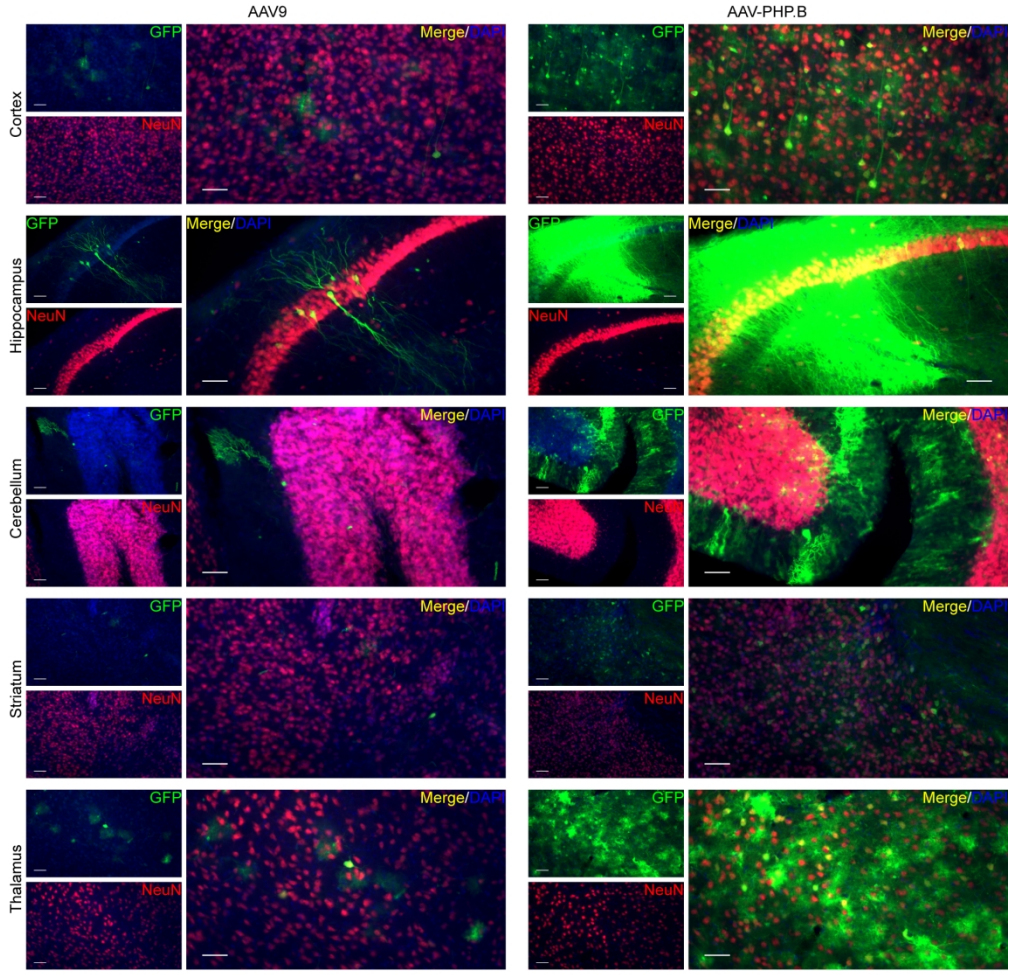

Supplementary Figure 3

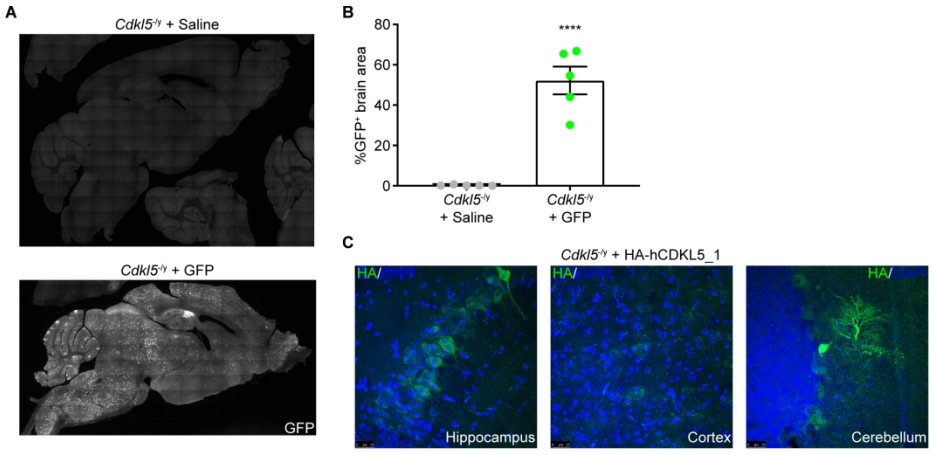

Supplementary Figure 4

180x230mm (300 x 300 DPI)

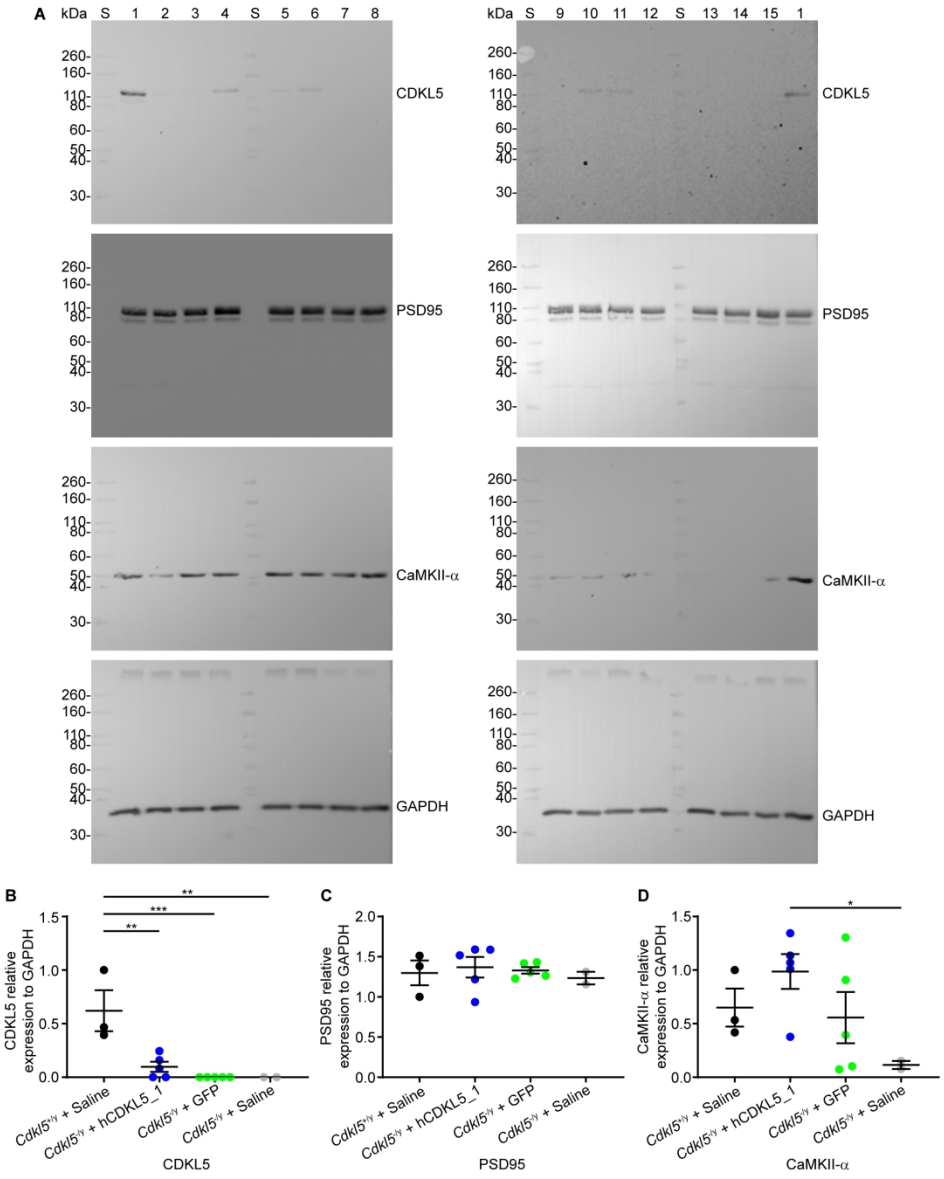

Supplementary Figure 5

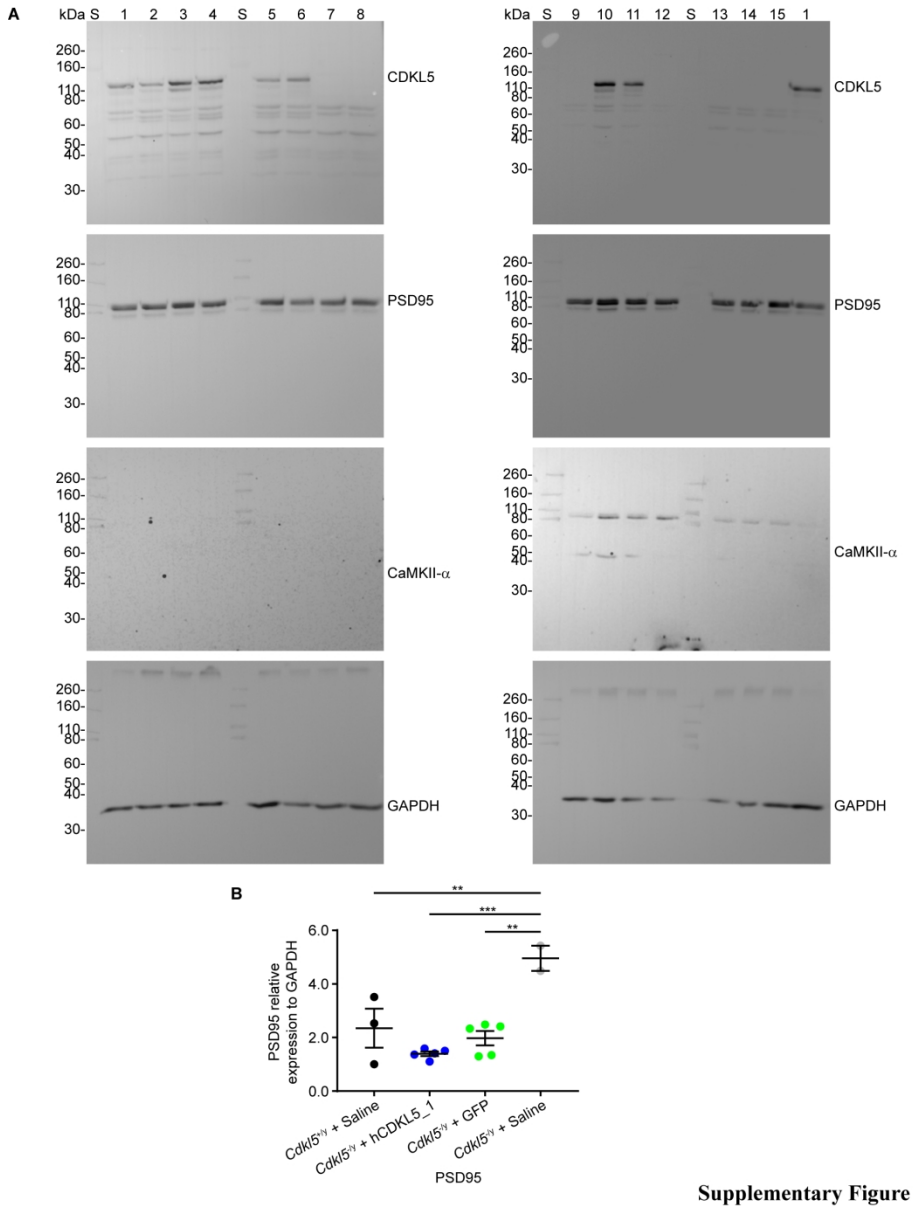

Supplementary Figure 6

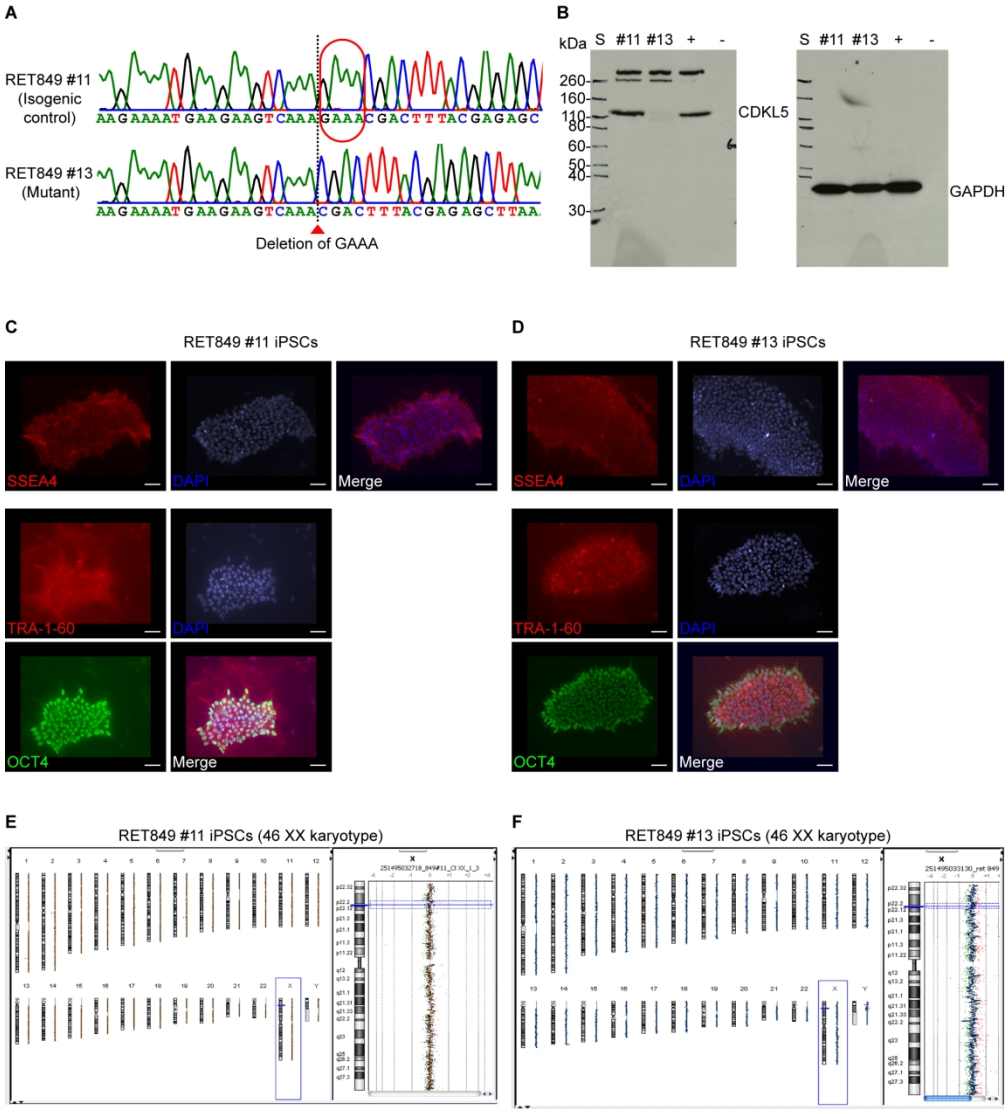

Supplementary Figure 7

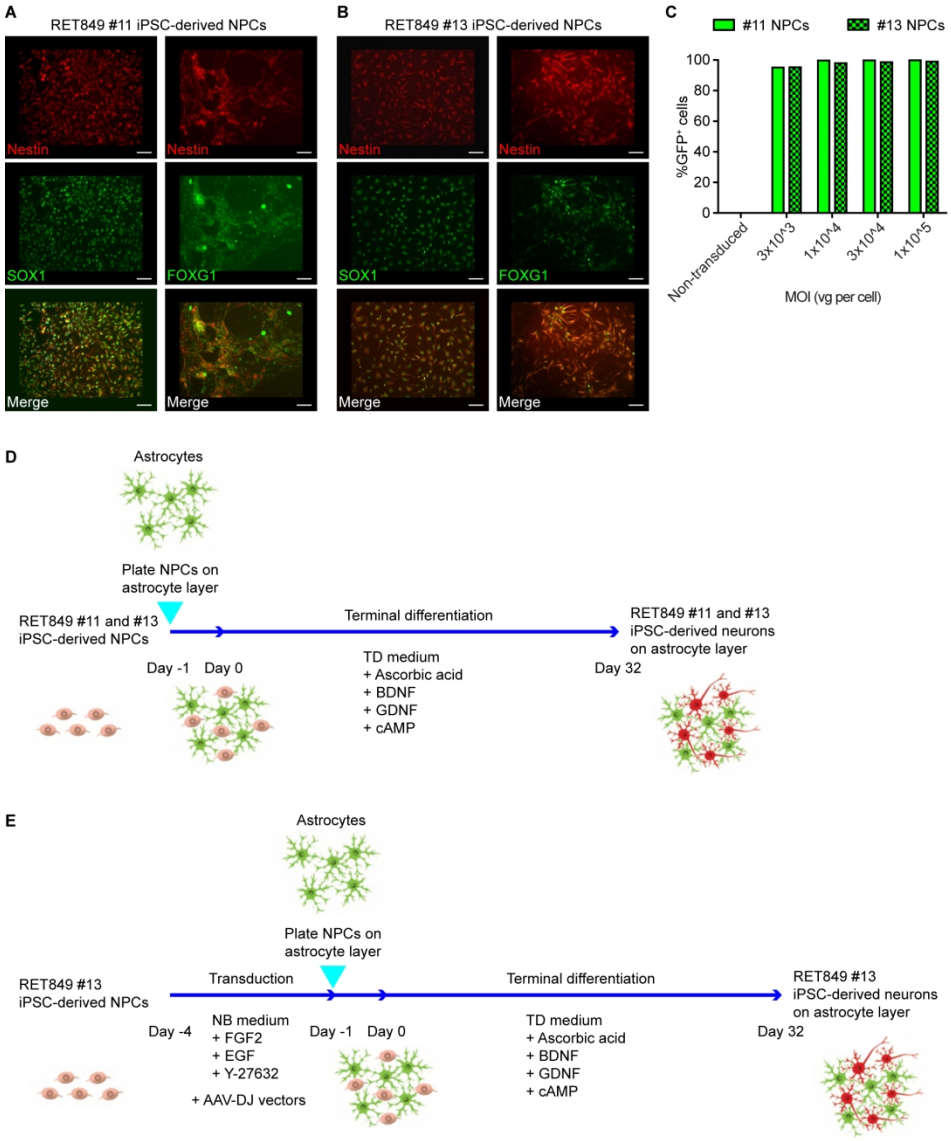

Supplementary Figure 8

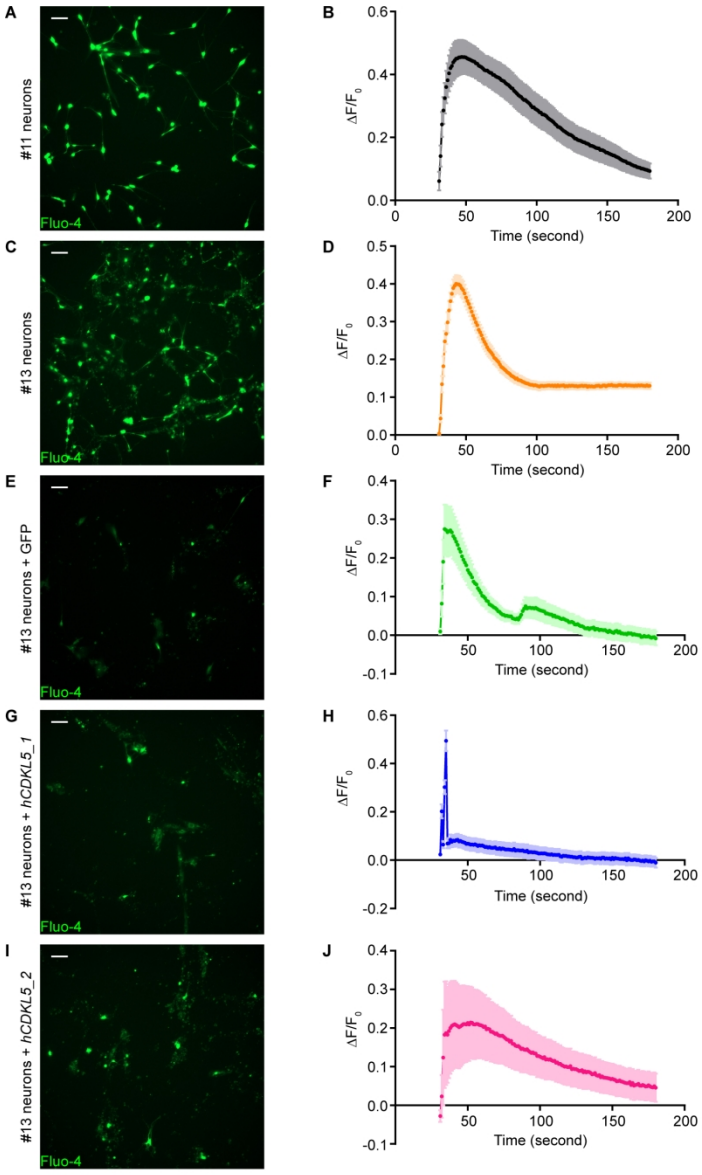

Supplementary Figure 9

180x230mm (300 x 300 DPI)

ARRIVE

The ARRIVE Guidelines Checklist

Animal Research: Reporting In Vivo Experiments

Carol Kilkenny[1], William J Browne[2], Innes C Cuthill[3], Michael Emerson[4] and Douglas G Altman[5]

[1]The National Centre for the Replacement, Refinement and Reduction of Animals in Research, London, UK, [2]School of Veterinary Science, University of Bristol, Bristol, UK, [3]School of Biological Sciences, University of Bristol, Bristol, UK, [4]National Heart and Lung Institute, Imperial College London, UK, [5]Centre for Statistics in Medicine, University of Oxford, Oxford, UK.

	ITEM	RECOMMENDATION	Section/ Paragraph
Title	1	Provide as accurate and concise a description of the content of the article as possible.	Title
Abstract	2	Provide an accurate summary of the background, research objectives, including details of the species or strain of animal used, key methods, principal findings and conclusions of the study.	Abstract
INTRODUCTION			
Background	3	a. Include sufficient scientific background (including relevant references to previous work) to understand the motivation and context for the study, and explain the experimental approach and rationale. b. Explain how and why the animal species and model being used can address the scientific objectives and, where appropriate, the study's relevance to human biology.	Paragraphs 1-8 Paragraphs 5-7
Objectives	4	Clearly describe the primary and any secondary objectives of the study, or specific hypotheses being tested.	Paragraph 8
METHODS			
Ethical statement	5	Indicate the nature of the ethical review permissions, relevant licences (e.g. Animal [Scientific Procedures] Act 1986), and national or institutional guidelines for the care and use of animals, that cover the research.	Paragraph 10
Study design	6	For each experiment, give brief details of the study design including: a. The number of experimental and control groups. b. Any steps taken to minimise the effects of subjective bias when allocating animals to treatment (e.g. randomisation procedure) and when assessing results (e.g. if done, describe who was blinded and when). c. The experimental unit (e.g. a single animal, group or cage of animals). A time-line diagram or flow chart can be useful to illustrate how complex study designs were carried out.	Paragraphs 11-13, 17 Supplementary Tables 2-3
Experimental procedures	7	For each experiment and each experimental group, including controls, provide precise details of all procedures carried out. For example: a. How (e.g. drug formulation and dose, site and route of administration, anaesthesia and analgesia used [including monitoring], surgical procedure, method of euthanasia). Provide details of any specialist equipment used, including supplier(s). b. When (e.g. time of day). c. Where (e.g. home cage, laboratory, water maze). d. Why (e.g. rationale for choice of specific anaesthetic, route of administration, drug dose used).	Paragraphs 11-14 Supplementary methods Paragraphs 9-18
Experimental animals	8	a. Provide details of the animals used, including species, strain, sex, developmental stage (e.g. mean or median age plus age range) and weight (e.g. mean or median weight plus weight range). b. Provide further relevant information such as the source of animals, international strain nomenclature, genetic modification status (e.g. knock-out or transgenic), genotype, health/immune status, drug or test naïve, previous procedures, etc.	Paragraphs 10-11

The ARRIVE guidelines. Originally published in *PLoS Biology*, June 2010[1]

Housing and husbandry	9	Provide details of: a. Housing (type of facility e.g. specific pathogen free [SPF]; type of cage or housing; bedding material; number of cage companions; tank shape and material etc. for fish). b. Husbandry conditions (e.g. breeding programme, light/dark cycle, temperature, quality of water etc for fish, type of food, access to food and water, environmental enrichment). c. Welfare-related assessments and interventions that were carried out prior to, during, or after the experiment.	Not included
Sample size	10	a. Specify the total number of animals used in each experiment, and the number of animals in each experimental group. b. Explain how the number of animals was arrived at. Provide details of any sample size calculation used. c. Indicate the number of independent replications of each experiment, if relevant.	Paragraph 11 Supplementary Tables 2-3
Allocating animals to experimental groups	11	a. Give full details of how animals were allocated to experimental groups, including randomisation or matching if done. b. Describe the order in which the animals in the different experimental groups were treated and assessed.	Paragraph 11
Experimental outcomes	12	Clearly define the primary and secondary experimental outcomes assessed (e.g. cell death, molecular markers, behavioural changes).	Paragraphs 13, 17-16, 19 Supplementary methods Paragraphs 9-18
Statistical methods	13	a. Provide details of the statistical methods used for each analysis. b. Specify the unit of analysis for each dataset (e.g. single animal, group of animals, single neuron). c. Describe any methods used to assess whether the data met the assumptions of the statistical approach.	Paragraph 23 Figures 2-5 Supplementary Figures 4-6
RESULTS			
Baseline data	14	For each experimental group, report relevant characteristics and health status of animals (e.g. weight, microbiological status, and drug or test naïve) prior to treatment or testing. (This information can often be tabulated).	Paragraph 8 Figure 3
Numbers analysed	15	a. Report the number of animals in each group included in each analysis. Report absolute numbers (e.g. 10/20, not 50%[2]). b. If any animals or data were not included in the analysis, explain why.	Paragraphs 4, 9-10 Supplementary Tables 2-3 Figures 2-5 Supplementary Figures 4-6
Outcomes and estimation	16	Report the results for each analysis carried out, with a measure of precision (e.g. standard error or confidence interval).	Paragraphs 4-6, 9-15 Figures 2-5 Supplementary Figures 4-6
Adverse events	17	a. Give details of all important adverse events in each experimental group. b. Describe any modifications to the experimental protocols made to reduce adverse events.	Not included
DISCUSSION			
Interpretation/ scientific implications	18	a. Interpret the results, taking into account the study objectives and hypotheses, current theory and other relevant studies in the literature. b. Comment on the study limitations including any potential sources of bias, any limitations of the animal model, and the imprecision associated with the results[2]. c. Describe any implications of your experimental methods or findings for the replacement, refinement or reduction (the 3Rs) of the use of animals in research.	Paragraphs 2-6

Generalisability/ translation	19	Comment on whether, and how, the findings of this study are likely to translate to other species or systems, including any relevance to human biology.	Paragraphs 2-3, 6 Introduction Paragraph 7
Funding	20	List all funding sources (including grant number) and the role of the funder(s) in the study.	Funding

References:
1. Kilkenny C, Browne WJ, Cuthill IC, Emerson M, Altman DG (2010) Improving Bioscience Research Reporting: The ARRIVE Guidelines for Reporting Animal Research. *PLoS Biol* 8(6): e1000412. doi:10.1371/journal.pbio.1000412
2. Schulz KF, Altman DG, Moher D, the CONSORT Group (2010) CONSORT 2010 Statement: updated guidelines for reporting parallel group randomised trials. *BMJ* 340:c332.

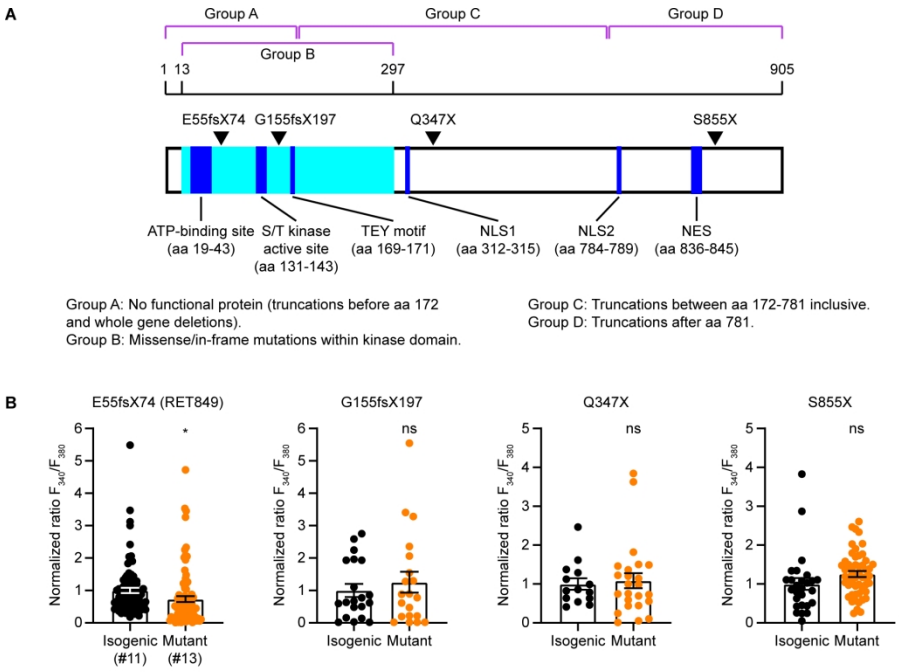

Figure R. Figure for the responses to referee comments only.

180x230mm (300 x 300 DPI)